HIGH-PERFORMANCE DIELECTRIC ELASTOMER ACTUATORS

DISSERTATION

ZUR ERLANGUNG DES GRADES
DES DOKTORS DER INGENIEURSWISSENSCHAFTEN
DER NATURWISSENSCHAFTLICH-TECHNISCHEN FAKULTÄT
DER UNIVERSITÄT DES SAARLANDES

VON

STEFFEN HAU

Saarbrücken

2018

Tag des Kolloquiums:	*16.07.2018*
Dekanin/Dekan:	*Univ.-Prof. Dr. rer. nat. Guido Kickelbick*
Berichterstatter/innen:	*Prof. Dr.-Ing. Stefan Seelecke*
	Prof. Dr.-Ing. Matthias Nienhaus (i.V. Prof. Dr. rer. nat. Helmut Seidel)
	Prof. Herbert Shea
Vorsitz:	*Prof. Dr.-Ing. Stefan Diebels*
Akad. Mitarbeiter/in:	*Dr. rer. nat. Tilman Sauerwald*

“The electric light did not come from the continuous improvement of candles.”

- Oren Harari -

Dedicated to my beloved wife, Christina.

Acknowledgements

First and foremost, I thank my wife Christina for standing beside me throughout the last seven years. Her constant moral support and love helped me through all the difficulties within my academic career and daily life. Her understanding for me working late, on the weekend, and during our wedding planning was a gift and motivation. My family receives my deepest gratitude for their dedication and support during my undergraduate studies that provided the foundation for this work.

I also acknowledge my co-workers at the Intelligent Material Systems Lab at Saarland University who made the research for this dissertation possible. In particular, Thomas and Benedikt for their support on electronic issues, Daniel and my student research assistants for their valuable research support, Micah for his introduction into the world of DEAs and Gianluca for reading through most of my publications and giving appreciated suggestions for improvement.

In addition, I want to express my sincere thanks to Alexander York for his all-embracing help and guidance even after leaving the lab, Marc Williams for his physical and mental support, and both for becoming appreciated friends.

A special thank also goes to Laura York and Paul Motzki for revising the drafts of this dissertation.

I also acknowledge the companies *Wacker Chemie AG* for supplying materials and *Parker Hannifin Corporation* for their material and financial support.

Finally, I thank Professor Stefan Seelecke for giving me the opportunity to do research at his lab and making this dissertation possible. His trust, given freedom, and advice have been invaluable during my time as a Ph.D. and beyond.

Abstract

Dielectric elastomer actuators (DEAs) feature high energy efficiency, lightweight, design flexibility and the use of low cost materials and processes. This holds particularly true for membrane actuators, which, in addition to the dielectric elastomer comprise a separate biasing system. The particular design of the biasing system may dramatically improve the DEA performance, but at the same time, it adds complexity to such a design process. Therefore, in this work, a systematic design approach to adapt DEA systems to specific applications is developed. It allows calculation of all relevant design parameters and incorporates experimentally validated scaling laws to account for actuator geometry effects. Finally, the capability of the design process is illustrated at two examples. In the first one, the force output of circular membrane DEAs, which is typically in the hundreds of millinewton range, is increased by more than two orders of magnitude. For the first time, record-high forces of 100 Newton are generated, while an innovative overall system design maintains compactness. The second system is designed for high reversible actuation strains in the range of >50%. The use of silicone as elastomer additionally results in high-speed actuation. DEA systems with such outstanding performance prove that they are capable of competing with existing technologies such as solenoids, while adding additional functionality and, in the future, smartness through “self-sensing” properties.

Zusammenfassung

Dielektrische Elastomeraktoren (DEA) weisen eine hohe Energieeffizienz, geringes Gewicht und Designflexibilität, bei gleichzeitig geringen Herstellungskosten, auf. Dies trifft speziell auf Membran DEA zu, die zusätzlich über einen Vorspannmechanismus verfügen. Diese Kombination zu einem DEA System ermöglicht eine deutliche Leistungssteigerung, birgt jedoch eine deutlich erhöhte Komplexität. Daher wird in dieser Arbeit ein systematischer Auslegungsprozess entwickelt, um solche Aktorsysteme anwendungsspezifisch anzupassen. Dieser erlaubt, unter anderem mit empirisch ermittelten Skalierungsgesetzen zur Aktorgeometrie, alle notwendigen Aktorparameter zu bestimmen. Abschließend wird die Leistungsfähigkeit des Auslegeprozesses an zwei Beispielen illustriert. Im ersten wird die Kraft eines Membran DEA, die typischerweise im Bereich von einigen hundert mN liegt, um zwei Größenordnungen erhöht. Erstmals erreicht ein solcher Aktor Kräfte von 100 N, während eine innovative Konstruktion dennoch für Kompaktheit sorgt. Mit dem zweiten Aktor können wiederholbare und schnelle (bis zu 0,3 m s^{-1}) Aktuierungsdehnungen von >50% erzeugt werden. DEA Systeme, die eine solche Leistungsfähigkeit aufweisen, zeigen, dass sich die Technologie mit herkömmlichen Aktorprinzipien (z.B. elektromagnetische) messen kann. Darüber hinaus bieten DEA zusätzliche Funktionalität und können in Zukunft durch ihre Möglichkeit des „Self-sensing“ auch zur Entwicklung intelligenter Systeme für die Industrie 4.0 beitragen.

Table of contents

ACKNOWLEDGEMENTS ..... **VII**

ABSTRACT ..... **VIII**

ZUSAMMENFASSUNG ..... **IX**

TABLE OF CONTENTS ..... **XI**

CHAPTER 1 INTRODUCTION **1**

1.1 MOTIVATION 1

1.2 RESEARCH OBJECTIVE AND THESIS STRUCTURE 3

CHAPTER 2 FUNDAMENTALS OF DIELECTRIC ELASTOMERS **5**

2.1 ELECTROMECHANICAL TRANSDUCTION PRINCIPLE 5

2.2 ACTUATOR CONFIGURATIONS 8

2.2.1 STACK ACTUATORS 8

2.2.2 MEMBRANE ACTUATORS 10

2.2.3 TUBE AND ROLL ACTUATORS 15

2.3 MATERIALS 17

2.3.1 ELASTOMERS 18

2.3.2 ELECTRODES 19

2.4 MANUFACTURING OF MEMBRANE DIELECTRIC ELASTOMER ACTUATORS 22

2.5 CHARACTERIZATION OF DIELECTRIC ELASTOMER ACTUATORS 25

CHAPTER 3 DIELECTRIC ELASTOMER ACTUATOR DESIGN **29**

3.1 ACTUATOR MODELING AND THE INFLUENCE OF BIASING ELEMENTS 30

3.2 NEGATIVE-RATE BIAS SPRING DESIGN 36

3.2.1 SIMULATION MODEL 38

3.2.2 PARAMETER STUDY 39

3.2.3 DESIGN METHOD 41

3.3 GEOMETRY DEPENDENT PERFORMANCE PREDICTION AND SCALING LAWS....45
3.3.1 PERFORMANCE PREDICTION AND EVALUATION 47
3.3.2 EXPERIMENTAL RESULTS AND SCALING LAWS 54
3.4 APPLICATION-DRIVEN ACTUATOR SYSTEM DESIGN 57
3.5 CONCLUSION 63

CHAPTER 4 HIGH-FORCE ACTUATOR SYSTEMS.....65
4.1 STATE-OF-THE-ART HIGH-FORCE ACTUATION 65
4.2 DESIGN AND CHARACTERIZATION OF A HIGH-FORCE ACTUATOR SYSTEM 66
4.2.1 ACTUATOR SYSTEM CONCEPT AND MANUFACTURING 67
4.2.2 CHARACTERIZATION OF COMPONENTS AND ACTUATOR SYSTEM PERFORMANCE..... 77
4.3 DISCUSSION OF RESULTS.....83

CHAPTER 5 HIGH STROKE ACTUATOR SYSTEMS 85
5.1 STATE-OF-THE-ART HIGH STROKE ACTUATION 85
5.2 DESIGN AND CHARACTERIZATION OF A HIGH STROKE ACTUATOR SYSTEM.....87
5.2.1 ACTUATOR DESIGN AND MANUFACTURING..... 88
5.2.2 CHARACTERIZATION OF COMPONENTS..... 90
5.2.3 ACTUATOR SYSTEM CONCEPT 92
5.2.4 ACTUATOR SYSTEM PERFORMANCE..... 93
5.3 DISCUSSION OF RESULTS.....97

CHAPTER 6 CONCLUSION AND OUTLOOK 101

REFERENCES 103

LIST OF FIGURES 117

LIST OF TABLES 124

LIST OF ABBREVIATIONS.....125

NOMENCLATURE.....127

CURRICULUM VITAE 130

PUBLICATIONS.....132

Chapter 1 Introduction

Many modern applications, such as biomedical devices, robotics or automation, can benefit from small, lightweight, low cost, mechanically compliant, and energy efficient actuators. The members of a group of materials with intrinsic transduction properties, which are known as “smart” or “intelligent” materials, exhibit at least some of these advantages compared to conventional actuator technologies such as pneumatic or electromagnetic (EM) ones. Common smart materials are electroactive ceramics (EACs), shape-memory-alloys (SMAs), and electroactive polymers (EAPs). While EACs have already entered the market in numerous applications, e.g., micro motors [1] and injectors [2], and SMAs start to establish themselves in first niche areas, e.g., seat inflation valves [3], EAPs are a relatively new and emerging technology [4]. EAP technology started to gain research interest in the early 1990s with the work of Pelrine and others at *Stanford Research Institute International* [5,6], even though Röntgen already described a reversible electrically-induced elongation of a natural rubber band in 1880 [7], which was likely the first dielectric EAP. This thesis deals with such dielectric EAPs.

1.1 Motivation

Dielectric EAPs, most commonly referred to as dielectric elastomers (DE), consist of a dielectric elastomer membrane, which is sandwiched between compliant electrodes, resulting in what could be called a flexible capacitor. In this configuration, they can function as sensors, generators, and actuators. Due to their ability to transform mechanical energy into electrical energy and vice versa, they are also named DE transducers (DETs). DETs represent a promising technology for building small, lightweight, and energy efficient systems [4,8]. DE actuators (DEAs) in particular outperform existing technologies, such as voice coils, in terms of energy density, actuation pressure, and strain. Their large actuation strain (up to 380%) [9] is unique even in the class of smart materials (see Table 1.1).

Table 1.1: Comparison of smart materials properties and conventional EM actuators (voice coil). Data refers to [10] *unless otherwise stated.*

Property	DEA	SMA [c]	EAC [d]	EM [e]
Density (g cm^{-3}) [11]	1-2.5	5-6	6-8	8
Modulus	0.1-3 MPa [4]	20-80 GPa [4]	~ 60 GPa [12]	---
Actuation Strain (%)	120[a] / 380[b]	< 5	0.2	50
Actuation Pressure (MPa)	3[a]/ 7.2[b]	< 400	110	0.1
Reaction Speed	µs to ms [13]	ms to min [11]	µs [11]	µs [11]
Driving Voltage [11]	10-150 V/µm	1-10 V	50-80 V	typ. 0-120V
Specific Energy Density (J g^{-1})	0.75[a] / 3.4[b]	> 15	0.013	0.003
Energy Density (J cm^{-3})	0.75[a] / 3.4[b]	> 100	0.1	0.025

[a] Silicone-based DEA

[b] Acrylic-based DEA

[c] Nickel-titanium alloy (NiTi)

[d] Lead zirconate titanate (PZT), at a maximum electric field of 4 V µm^{-1}

[e] EM: Values based on array of 10 mm thick voice coils, 50% conductor, 50% permanent magnet, 1 T magnetic field, 2 ohm-cm resistivity, and 40,000 W m^{-2} power dissipation.

In addition to their outstanding actuation properties, DETs show potential to make use of the "self-sensing" effect for building smart systems. The effect is based on their capacitor-like structure. Every change in geometry results in a measurable capacitance change, which directly relates to the state of deformation without requiring external sensors [14].

Due to these unique properties, several DET applications have been proposed and documented in recent literature, e.g., valves [15,16], pumps [17,18], optical switches [19,20], braille displays [21], loudspeakers [22], translation [23] and positioning stages [24], tunable lenses [25], and grippers [26,27]. In addition, applications such as pressure [28] or weight sensing [29], as well as energy harvesting [30–32], have been documented. The inherent softness of the elastomer is also of particular interest for the emerging field of soft robotics, in which many applications, such as the ones shown in [33], have been proposed.

1.2 Research objective and thesis structure

The applications presented above are just a few examples with potentially many more that have yet to be studied. However, each of these applications presents different requirements, and in order to increase the acceptance of the technology among engineers and designers, it is an important task to establish systematic design rules and scaling laws. This will support the future development of novel solutions in a broad field of applications and will aid to access the large potential of dielectric elastomers.

In addition to the development of a systematic design methodology, it is also important to understand how advanced design concepts may help expand the limits of DE applications. In this thesis, a DE membrane actuator system will be introduced that provides force outputs three orders of magnitude larger than previously introduced membrane solutions. Furthermore, a new concept is introduced that allows linear actuation strokes of up to 50% of the original actuator length. Both of these examples emphasize the importance of proper design concepts based on a thorough understanding of the material's behavior.

One of the specific aims of this work is the development of scaling laws, which can be used to adapt DEAs to various applications. The focus of the development is on the actuator geometry and the mechanics of biasing subsystems, useful for the operation of membrane DEAs. The goal is a prediction method for the DEAs' performance, which does not make use of complex and time-consuming finite element (FE) simulations (see, e.g., [34,35]), but it establishes clear rules that can be directly employed by the design engineer.

The gained knowledge on scaling is subsequently used to developed design methods, which expand the limits (in terms of stroke and force output) of state-of-the-art DEAs. This specifically involves:

a) a systematic approach for the intelligent combination of a biasing mechanism with particular DEA designs to enable high-forces and/or high strokes,
b) novel biasing and manufacturing concepts for stacks of membrane DEAs,
c) and the integration of both (DEAs and biasing) within a simple and compact design.

Each of the presented high-performance DEA systems employs state-of-the-art industrial manufacturing techniques and commercially available materials.

To achieve the aims stated above, this thesis is organized as follows:

Chapter 2 gives an introduction into the operating principles of DEAs, different actuator configurations, the materials used, and the manufacturing process. In addition, basic mechanical and electrical characterization techniques are described.

Chapter 3 deals with the DEA design process, which is based on a method using force equilibria between DEA, biasing mechanism, and external loads. The influence of different biasing mechanisms and DEA geometries on the performance of DEA systems is described and scaling laws are obtained by the empirical characterization of DEAs with different geometries. Based on these results, a straight-forward modeling method for the force-displacement characteristic of circular membrane DEAs is developed. Finally, the gained knowledge is used to develop a design process for application-specific DEA systems with a focus on intelligent combinations of DEAs with biasing mechanisms.

Chapter 4 describes the use of the methods and the design process mentioned in the previous chapter for the design of a high-force actuator. Novel biasing, stacking, and integration concepts, which are needed for pushing the output force of membrane DEAs from a few hundreds of millinewtons to the 100 N level, are described. Finally, characterization results and performance of the high-force DEA systems are documented.

Chapter 5 discusses strip-in-plane DEAs to achieve high-stroke. This type of actuator, in combination with an appropriate biasing mechanism, is well-suited for fast high-stroke applications (actuation strain >60%). The performance of a technology demonstrator is documented.

Chapter 6 summarizes the results and concludes this thesis by giving an outlook on future research topics.

Chapter 2 Fundamentals of dielectric elastomers

EAP actuators can be classified by actuation principle as ionic or electronic polymers. For ionic EAPs, commonly referred to as ionic polymer-metal composites (IPMC), the generated motion is based on the migration of mobile ions. An electric field imposed across their thickness causes mobile ions to move into or out of the polymer matrix towards the respective electrode, resulting in swelling, shrinking, or large bending displacement [36]. Electronic EAPs are divided into two subcategories: ferroelectric and dielectric. The shape change of ferroelectric EAPs is related to attraction or repulsion of polymer chains within the material induced by an electric field, while dielectric EAPs, mostly referred to as dielectric elastomers, which are studied in this thesis, are driven by Coulomb forces [37].

This chapter starts with a description of the fundamental design and actuation principles of DEAs, followed by an introduction into different actuator configurations reported in the recent literature. Subsequently, different DE materials and their effects on performance are described along with a screen-printing process used for manufacturing. Finally, basic characterization setups for DEAs, which are frequently used within this thesis, are explained.

2.1 Electromechanical transduction principle

Figure 2.1 (a) shows the basic structure of DEs. They typically consist of an elastomer layer, which is sandwiched between electrode layers. These electrode layers must be able to stretch and contract with the elastomer. Therefore, they need to be highly compliant. Given this basic structure, the DEs are electrically recognized as capacitors with the capacitance C, which can be written as

$$C = \varepsilon_0 \varepsilon_r \frac{A}{t}, \tag{2.1}$$

where ε_0 is the vacuum permittivity, ε_r the relative permittivity of the elastomer, A the overlapping area of the opposing electrodes, and t the thickness of the elastomer (in the direction of z). The area defined by A is also referred to as 'active area'. equation (2.1) is only true for an ideal DE with zero resistance in the electrode, an infinite resistance through the elastomer, and elastomer properties of a perfect dielectric, which means a constant ε_r [4]. The capacitor-like structure explains the first operational mode of DEs. Any change of its geometry, caused by an external force, changes its capacitance and can be related to its deformation. This effect is utilized for the sensor mode and can be used in applications such as strain [38] or pressure [28] sensing.

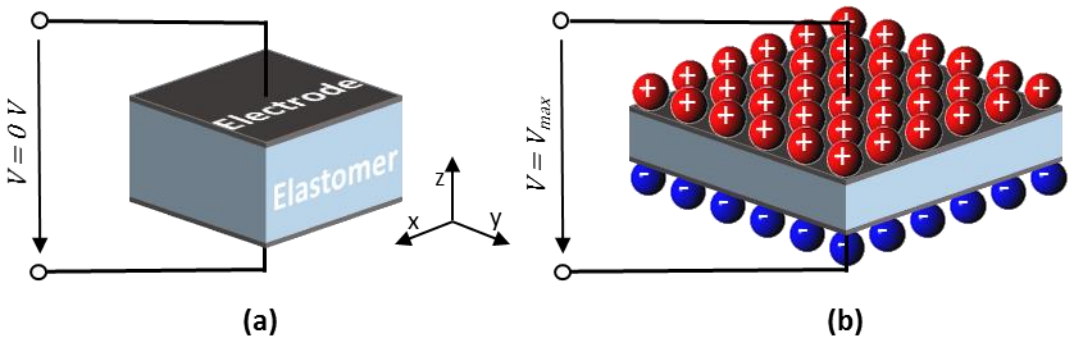

Figure 2.1: (a) Basic configuration of a DE in its initial and (b) in its charged state.

DEs can operate in two additional modes. They offer a transducer technology for converting electrical into mechanical energy and vice versa. They use a reversible electromechanical transduction mechanism, which allows them to operate in generator or actuator mode, depending on the direction of energy conversion [4]. However, the generator mode (see [30–32,39]) is not further discussed, as it is not the subject of this thesis.

In actuator mode, electrical energy is used to generate mechanical work. To do so, a high voltage (HV), referred to as U_{max} in Figure 2.1 (b), is applied to the DE to charge the capacitor. The opposing *unlike* charges on the electrodes attract each other and cause a thickness compression of the elastomer. Additionally, the incompressible nature of elastomers and the repelling forces of *like* charges (on the same electrode) cause an expansion of the elastomer surface area [40]. Both, reduction of thickness and surface area expansion can be used for actuation. Typical actuation voltages are between 1 and 10 kV

for an elastomer thickness of 10 to 100 µm [41]. Thinner elastomer layers can reduce the driving voltage as shown by Poulin *et al.* in [42]. They manufactured DEAs with 3 µm thick membranes, which exhibit an actuation strain of 7.5% at 245 V applied. However, these thin membranes are very difficult to handle and the influence of the mechanical properties of the electrodes increases dramatically.

The force output of a DEA is directly related to the Maxwell pressure p, which can be written as:

$$p = \varepsilon_0 \varepsilon_r E^2 = \varepsilon_0 \varepsilon_r \left(\frac{V}{t}\right)^2, \tag{2.2}$$

where E is the applied electric field across the elastomer and V is the applied voltage. equation (2.2) can be derived by an approach, which equalizes mechanical and electrical energy introduced by Pelrine *et al.* in [8]. To do this, additional assumptions need to be made. The first one is a further simplification to the ones mentioned above, for the capacitance of a DE: the elastomer is considered perfectly elastic with no dissipative mechanical losses; and the second one is the assumption that the volume of an elastomer stays constant under deformation [43]. The ability of a DE to reduce thickness and increase the area at the same time, when exposed to an electric field, leads to another interesting fact. Compared to air-gap, electrostatic actuators with two parallel rigid electrode plates, the resultant Maxwell pressure is twice as big for DEs, which can be explained by the additional degree-of-freedom (DOF). This additional DOF, namely the increase of area, couples (additionally to the reduced plate distance) into the energy conversion from electrical to mechanical energy [4].

The resultant strain of a DEA depends on a number of factors such as boundary conditions, elastic modulus, and loading conditions. In the unloaded and unconstrained case, which is the simplest, the thickness strain can be calculated by balancing the Maxwell pressure of (2.2) and the elastic force of the elastomer film. After which, thickness strain s_z is typically written as:

$$s_z = -\frac{p}{Y} = \frac{\varepsilon_0 \varepsilon_r E^2}{Y}, \tag{2.3}$$

with Y as the elastic modulus, despite the fact that elastomers show a non-linear stress-strain characteristic [8]. It should be kept in mind that equation (2.3) is not valid for loaded or biased DEAs discussed later in this work.

2.2 Actuator configurations

Flexibility in design is one of the major advantages of DEAs. They can be manufactured in many different sizes and shapes to suit the requirements of the intended application. Therefore, a variety of different actuators have been proposed within the last 30 years. In general, they are divided into two groups, following their actuation direction with respect to the applied electric field: Stack actuators use the thickness compression parallel to the electric field, whereas membrane actuators utilize the area expansion transversal to the electric field. In the following sections of this chapter, these two actuator types, along with roll (or rather tube) actuators, which are a particular 3-dimensional configuration of membrane actuators, are explained in detail.

2.2.1 Stack actuators

Stack actuators are a very popular actuator configuration. They have been studied by various research groups [44–47] and are even one of the few commercially available DE products [48]. They consist of multiple layers of DE stacked on top of each other (see Figure 2.2 (a) and (b)). An applied voltage causes the whole stack to contract by Δs (see Figure 2.2 (c)) and thereby produce a linear motion. The maximum achievable stroke is the sum of the contraction of each individual layer and thus scales with the number of layers. Typical contraction strains are in the range of 5 to 20% [47,49] depending on the design and the material used as dielectric. The force of such actuators scales with the active area of the DE layers.

Recent literature proposes three different automated manufacturing methods for stack DEAs. The first one from *TU Darmstadt*, Germany, is based on a completely wet process [44], which means the material is applied in liquid form. It starts with a spin-coating process, followed by a heat-induced cross-linking process to manufacture a dielectric layer

made of silicone. The electrodes are applied by spraying a graphite powder/solvent mixture through a shadow mask. These processes are repeated until the desired final layer number is reached. The other two processes are using a pre-fabricated elastomer film. The process of *Empa*, Switzerland, uses *VHB* ('*Very High Bond*') tape produced by the company *3M* as a dielectric. The tape is coated with an electrode material and afterwards cut into discs. These discs can be stacked to reach the desired final number of layers (see Figure 2.3 (c) and (d) [47]. The process of *University of Applied Sciences Ostwestfalen-Lippe* (*HS-OWL*), Germany, is similar to the one of *Empa*. It uses a pre-fabricated silicone or polyurethane film, which is spray-coated with structured electrodes. Instead of stacking individual layers, a folding process is used to manufacture small stack modules, which are then cut out. These modules are combined afterwards to form larger stacks. The connection of the individual layers is made by an elastomer strip coated with electrode material, which is wrapped around the stack (see Figure 2.3 (a), left) [45]. The advantage of the process of *Empa* and *HS-OWL* is the ability to manufacture sub-modules, which can be tested before combining them into a stack with several hundred layers, thus resulting in higher yields.

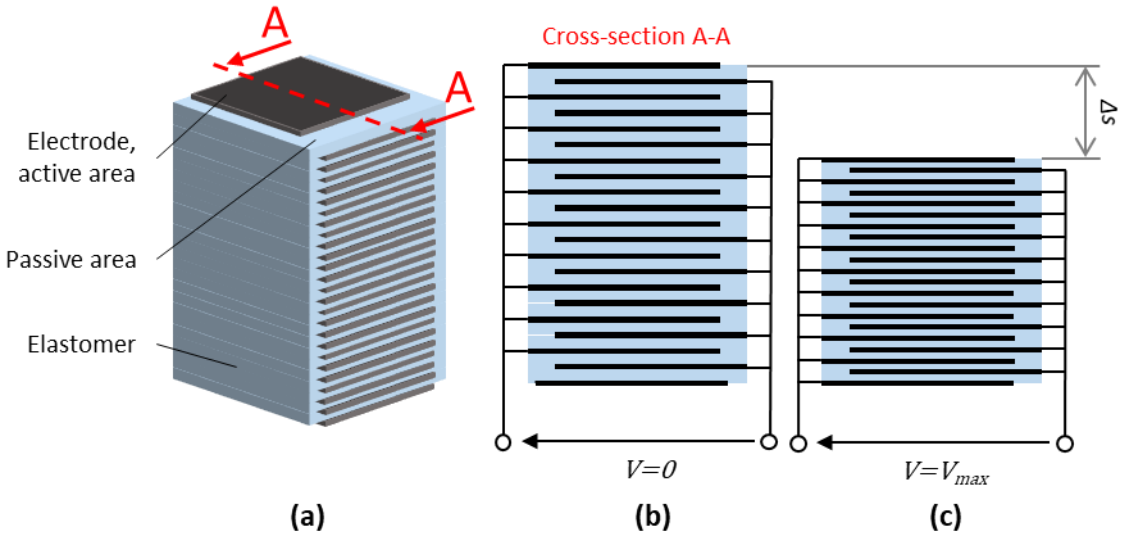

Figure 2.2: (a) Sketch of a stack actuator, (b) cross-section through the stack with electrical connections, and (c) cross-section through an activated stack.

The advantage of stack DEAs are their simple design, low integration effort, compactness, and ability to provide relatively high forces. However, their actuation strain is very limited and the passive area (see Figure 2.2 (a)), which is needed for insulation,

hinders the actuation. Nevertheless, this kind of actuator has shown its functionality in applications such as peristaltic pumps [44] or valves (see Figure 2.3 (d)) [16].

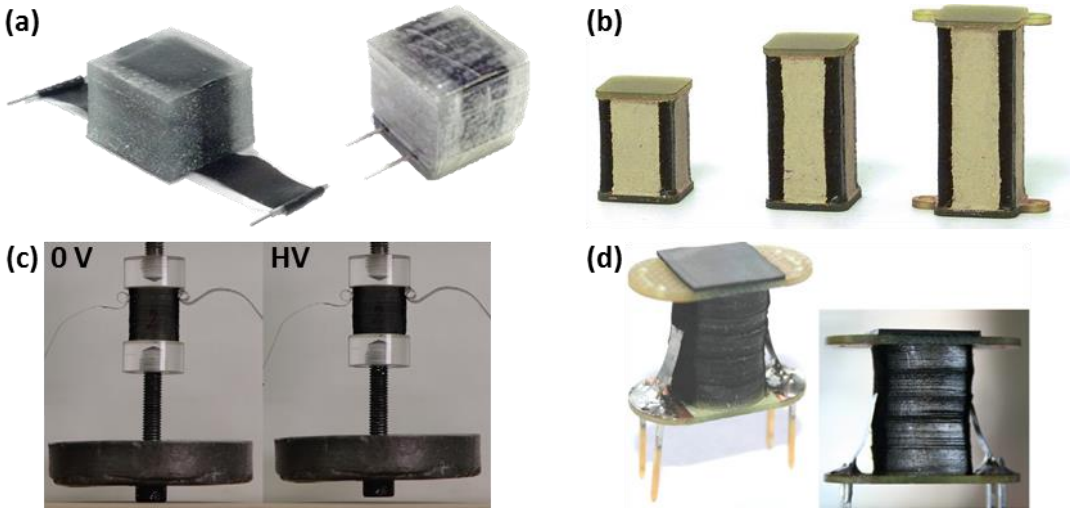

Figure 2.3: Examples of stack actuators. (a) Stack actuator from University of Applied Sciences Ostwestfalen-Lippe, Germany, manufactured by folding and stacking [50]. *(b) Commercial stack actuator made by CT-Systems, Switzerland* [51] *with process of Empa. (c) Stack actuator made by Empa, Switzerland, lifting a weight* [47]. *(d) Stack actuator for valve applications with sealing pad on top made by Empa, Switzerland [16].*

2.2.2 Membrane actuators

Membrane actuators are the second very popular actuator configuration. In contrast to stack actuators, they make use of the area expansion for actuation. In their simplest configuration, they consist of a single DE layer. However, in order to generate a reasonable amount of strain, membrane actuators need to be biased by an external force. This force is typically generated by pre-stretching the membrane or using passive biasing elements like hanging masses, springs, or non-linear springs. For a detailed discussion of different biasing systems and their influence on the actuator performance, see Section 3.1. The force of a membrane actuator scales with the active area and the number of layers, while the stroke scales with the length of the active area in the direction of movement [52]. Depending on the direction of actuation, membrane DEAs are divided into two groups: out-of-plane and in-plane actuators.

A special configuration, which is somewhere in-between the two groups, and acting in bending mode, are the minimum energy structure actuators [23]. They are typically based on a bi-layer, consisting of a support structure and a DE layer, which is attached after being pre-stretched. The pre-stretch causes the bi-layer to bend. The area expansion of the DE, triggered by an applied voltage results, in a relaxation of the DE and therefore in a reduced bending of the bi-layer. A minimum energy structure actuator, designed as a gripping device, is shown in Figure 2.4.

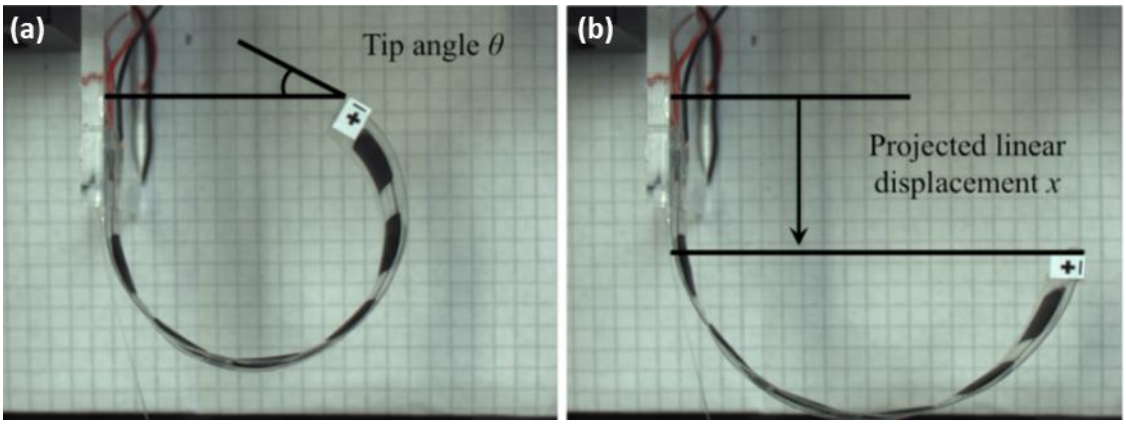

Figure 2.4: Minimum energy structure consisting of PET foil and a DE layer (a) at 0 V and (b) activated with 3.8 kV manufactured by École Polytechnique Fédérale de Lausanne [27].

In-plane actuators

Circular-in-plane (CIP) DEAs, also called expanding circle DEAs, are a common representative of the in-plane actuators. They are based on equi-biaxially pre-stretched DE membranes with a circular active area. To maintain the pre-stretch of the membrane, it is typically attached to a circular stiff frame (see Figure 2.5 (a)). If a voltage is applied, the circular electrode area expands radially (see Figure 2.5 (b)). This configuration is mainly used for evaluation of new elastomers, electrodes, and their combinations. When doing so, the conditions (frame size, electrode size, etc.) mentioned in [53] should be considered in any test setup to achieve a high level of comparability of the results. Rosset et al. [54] also proposed CIP-DEAs for electrode degradation tests (see Figure 2.6 (a)).

A very similar configuration, which uses a ring electrode instead of a circular one, has also practical use in optical applications like tunable lenses [25,55] or laser speckle

reduction [55]. These are some of the few commercial DE products. An additional interesting field of application are tunable windows (see Figure 2.6 (c)).

Another interesting and one of the simplest actuator configurations is the strip-in-plane (SIP) DEA. They often consist of a rectangular DE membrane attached to rigid frames at two opposing sides (see Figure 2.5 (c)). An external biasing force causes the membrane to expand uniaxially when the DE is charged (see Figure 2.5 (d)). The performance of such actuators strongly depends on the pre-stretch being perpendicular to the moving direction and the biasing force characteristic. Kollosche *et al.* [56] studied these influences and achieved a non-reversible voltage induced strain of 360% followed by an electrical break down.

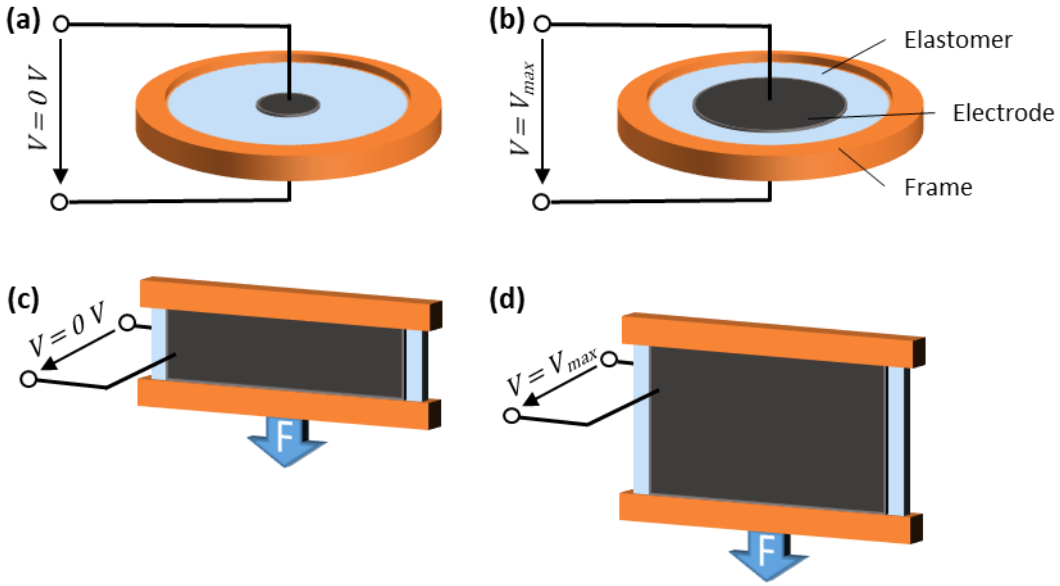

Figure 2.5: CIP-DEA biased by elastomer pre-stretch at (a) 0 V and (b) a high voltage applied. Strip in-plane (SIP) DEA biased by an external force at (c) 0 V and (d) a high voltage applied.

The SIP-DEA configuration is used by scientists to study material properties as well as electrically induced stress and strain distributions [57,58]. For any such characterization, the conditions mentioned in the 'Standard for dielectric elastomer transducers' [53] should be considered for experimental set-ups. *Artificial Muscle Inc.*, USA, developed a haptic feedback device based on SIP-DEAs. The external force for this device is generated by the film pre-stretch (see Figure 2.6 (d)). The SIP-DEA configuration is also studied in detail in Chapter 5 of this thesis.

A special in-plane configuration is the diamond-shaped actuator extensively studied by Vogan [59] and Plante [60] shown in Figure 2.6 (b). The name comes from the diamond-shaped compliant frame, which is attached to the elastomer film to maintain the pre-stretch applied before the attachment of it. Additionally, the frame is coupled to two elastic beams, which bias the whole structure. When a voltage is applied, this actuator generates a linear movement, while the stress and stretch stays evenly distributed across the entire active area. This is the particular advantage of the design (in terms of reliability) in addition to the high stroke being achieved [61]. It is worth mentioning, that Berselli and Vassura studied several additional designs of in-plane DEAs for soft robotic applications in [62].

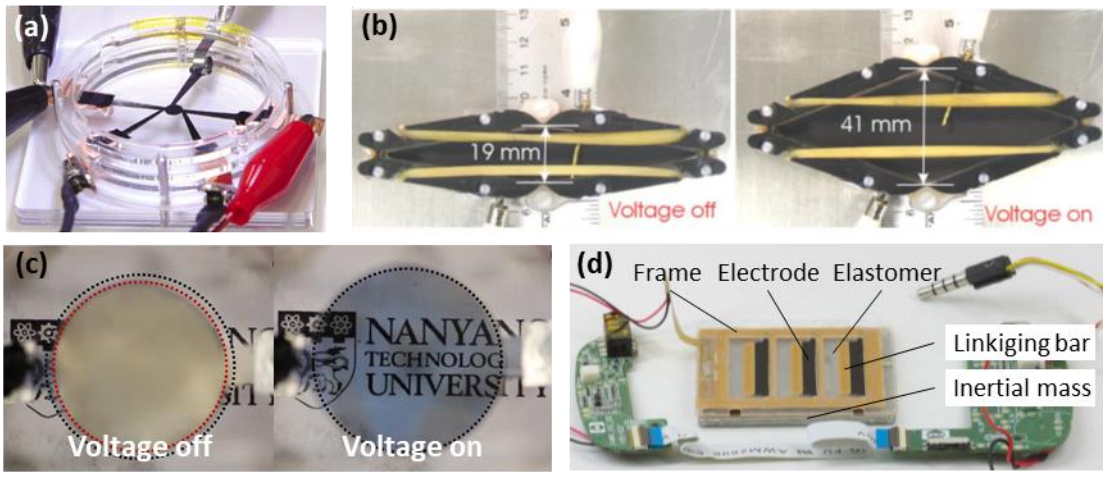

Figure 2.6: Examples for in-plane actuators. (a) CIP-DEA for material evaluation developed by École polytechnique fédérale de Lausanne, Switzerland [54]. *(b) Diamond-shaped linear actuator at its initial state and activated, manufactured by Massachusetts Institute of Technology, USA* [61]. *(c) CIP-DEA changing the light transmission developed by Nanyang Technological University, Singapore* [19]. *(d) Haptic feedback actuator and driving electronic designed for an iPod Touch by Artificial Muscle Inc., USA* [51].

Out-of-plane actuators

This actuator type generates motion out of the elastomer plane. The most prominent representative design for this actuator category are circular out-of-plane (COP) DEAs, which are also referred to as cone actuators. Their structure is similar to the CIP-DEAs. However, the active area has an annular shape and they feature an additional circular rigid center frame/ disc (see Figure 2.7 (a)). The DE membrane is typically pre-stretched equi-biaxially

and sandwiched between rigid frames to maintain the pre-stretch. Additionally, the rigid frames act as mechanical terminations. For actuation, a biasing force F_B, acting normal to the center disc and deflecting it out of plane, is needed in addition to an applied voltage. A biased COP-DEA is shown in Figure 2.7 (b). An applied voltage, in addition to a biasing force, causes the center disc to move further out of plane gaining the stroke Δs, because of the active area expansion (see Figure 2.7 (c)).

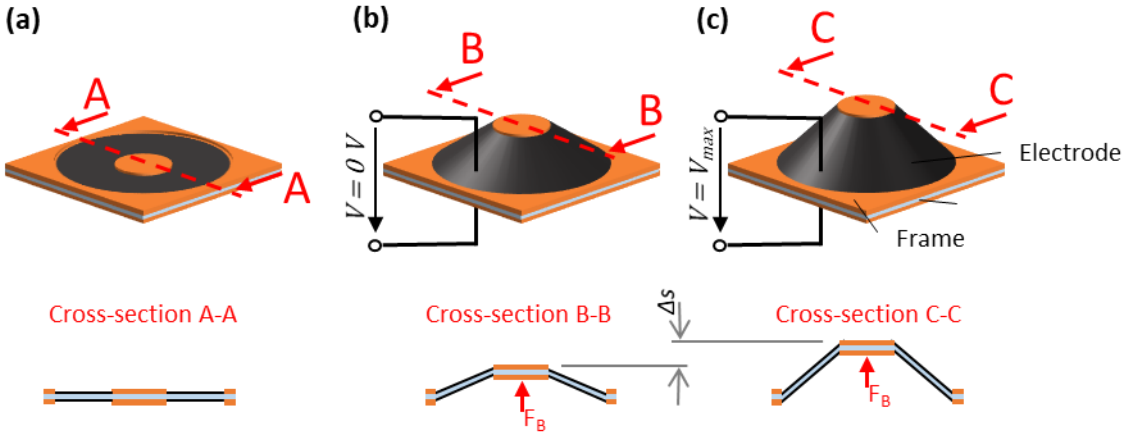

Figure 2.7: Sketch and cross-section of a COP-DEA (a) at rest, (b) biased out-of-plane with an external force F_B, and (c) biased out-of-plane with an external force F_B and additionally V_{max} applied.

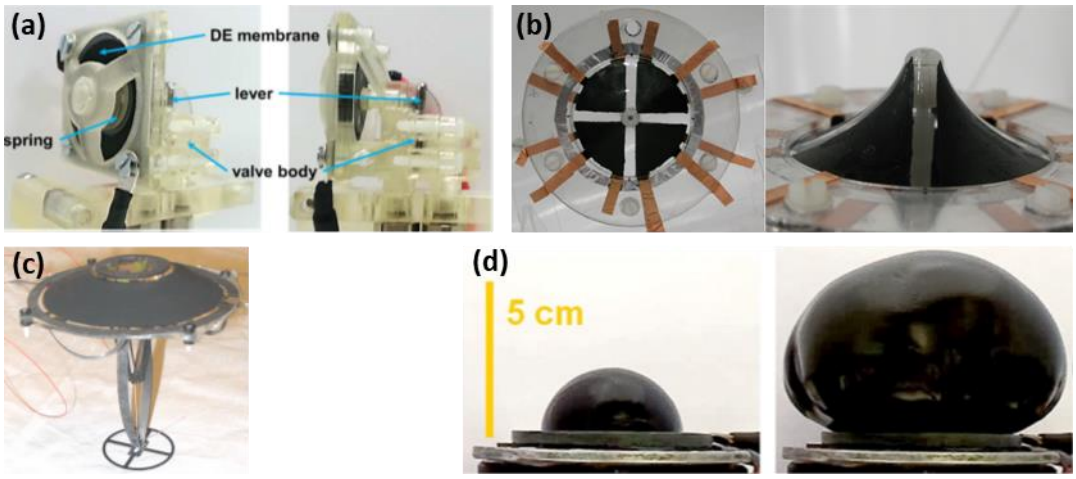

Figure 2.8: Examples for out-of-plane actuators. (a) COP-DEA for driving a valve manufactured by Saarland University, Germany [15]. *(b) Multi DOF positioning system driven by two COP-DEAs (left: top view, right: side view) and manufactured by Bristol Robotics Laboratory, UK* [63]. *(c) COP-DEA driven jumping robot for extraterrestrial exploration manufactured by Massachusetts Institute of Technology, USA* [61]. *(d) Balloon-like DEA (left: at rest, right: activate) demonstrated by Zhejiang University, China* [64].

COP-DEAs have been studied for many applications, e.g., positioners [24,65], jumping robots (see Figure 2.8 (c)) [61,66], valves (see Figure 2.8 (a)) [15], and with segmented electrodes for a multi-DOF positioning-system (see Figure 2.8 (b)) [63]. There are also more exotic out of plane actuators. Li *et al.* for example, proposed a balloon-like membrane DEA, which is biased by a chamber with pressurized air. In this configuration, a record-high voltage induced area expansion of 1692% is achieved (see Figure 2.8 (d)).

2.2.3 Tube and roll actuators

Tube (also referred as ring) and roll actuators have been very popular during the first decade of the 21st century. They have been the first choice to drive robotic arms for the *EAP arm wrestling challenge* hosted at the annual *EAPAD* conference [67]. The first challenge was in 2005. Tube and roll actuators are actually a particular configuration of membrane DEAs and as such use the area expansion for actuation too. They consist of an elastomer tube, which is covered with an electrode at the inside and outside (see Figure 2.9 (a) and (c)). The only difference between roll actuators in comparison to tube actuators is that they consist of a rolled-up multi-layer system of electrode and elastomer layers, as can be seen in the cross-section shown in Figure 2.9 (d). They can be rolled up around themselves or a passive core. The ends of the tube (and roll) actuator are not covered with electrodes, which acts as a mechanical termination and prevents arching when a voltage is applied. The Maxwell stress acts in the radial direction for this type of actuator and causes the tube or roll to expand in the direction of their axis by Δs (see Figure 2.9 (a) and (b)). The initial length of the actuator can be used to scale the stroke output, while the force output scales with the circumference and the number of DE layers used. Typically, strains of less than 13% are achieved [68,69]. Figure 2.10 (c) shows a photo of a roll actuator.

The performance of these actuators can also be increased by passive biasing elements. In this case, the passive core is replaced, for instance, by a compression spring. The spring keeps the elastomer under tension and increases the performance to strains in the range of 20 to 35% [67,70]. Such actuators are shown in Figure 2.10 (a) and (b). Under laboratory conditions, a special type of ring actuator (see Figure 2.10 (e)) even exhibits an actuation strain of 142% [71]. The high actuation strain is a result of the chosen material, a well-

selected and defined bi-axial pre-strain of the elastomer, and the use of buckled carbon fiber strips as biasing elements.

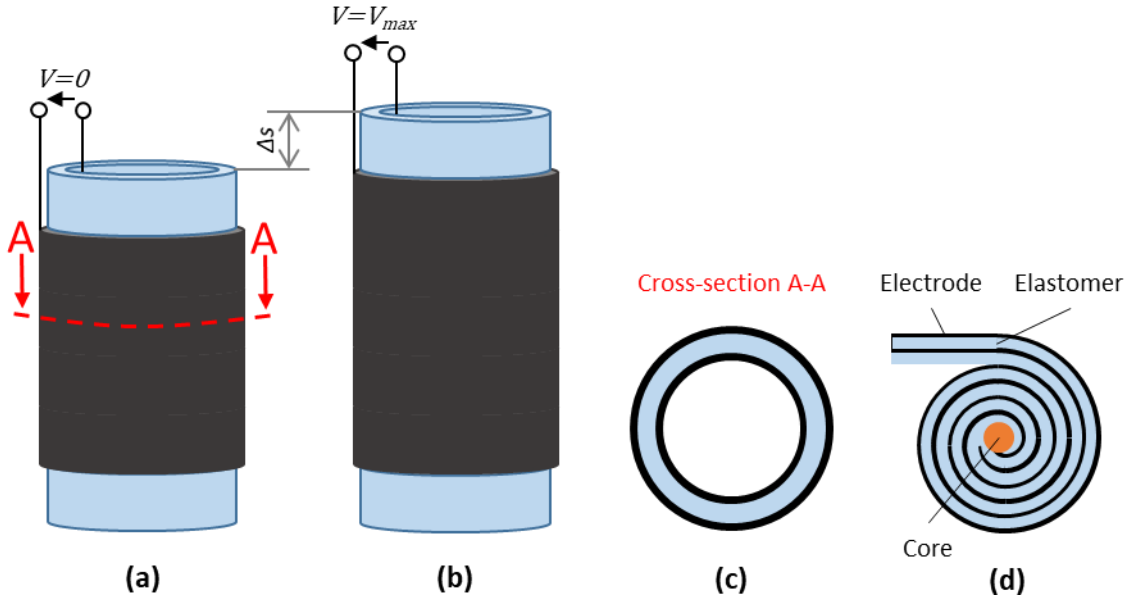

Figure 2.9: (a) Tube actuator in its initial state, (b) activated state, and (c) a cross-section of it. (d) Cross-section of a roll actuator.

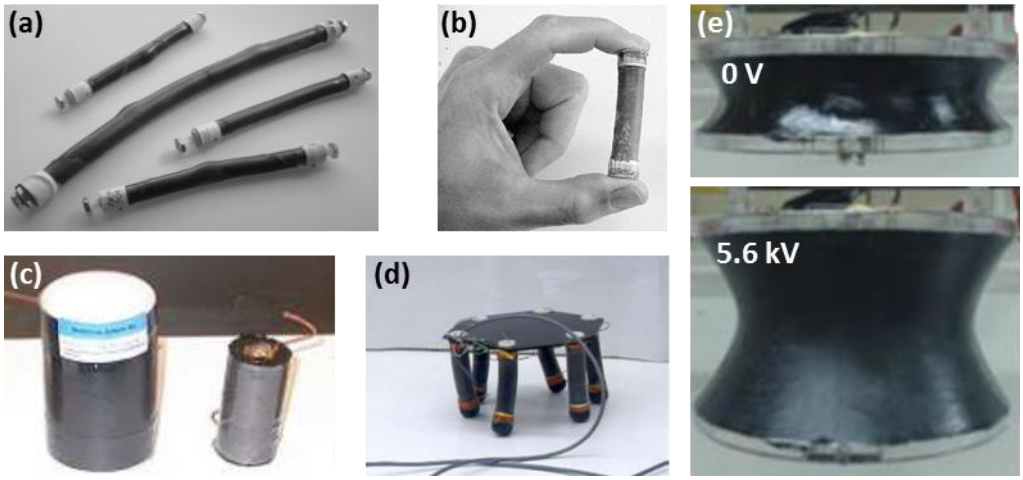

Figure 2.10: Roll actuators with spring core in different sizes made by (a) Empa, Switzerland [67] *and (b) Stanford Research Institute International, USA [20]. (c) Rolled actuator with passive core made by Defence R&D Canada–Atlantic* [69]. *(d) 2-DOF roll actuators with spring core used for a six-legged robot manufactured by Stanford Research Institute International, USA* [72]. *(e) Ring actuator at 0 V (top) and 5.6 kV (bottom) exhibiting 142% actuation strain demonstrated by the National University of Singapore* [71].

Roll actuators can also be designed to generate bending motion. In this case, the electrodes are segmented and do not cover the whole circumference of the actuator. Actuators with two semicircular electrodes, which allow a bending actuation (angles of up to 90°), are demonstrated within a walking robot shown in Figure 2.10 (d) [72].

2.3 Materials

The material selection is very important for a successful actuator design. Focus must not only be placed upon the material properties themselves but also on their influence on the actuator performance. In addition, the market requirements, need to be considered. Figure 2.11 shows the importance of the overall material performance (using the example of the elastomer), which needs to be considered when designing an actuator for a commercial application. Besides the elastomer, the electrode is the second most important material for DEAs. Both need to match each other and are discussed in detail in the following sections.

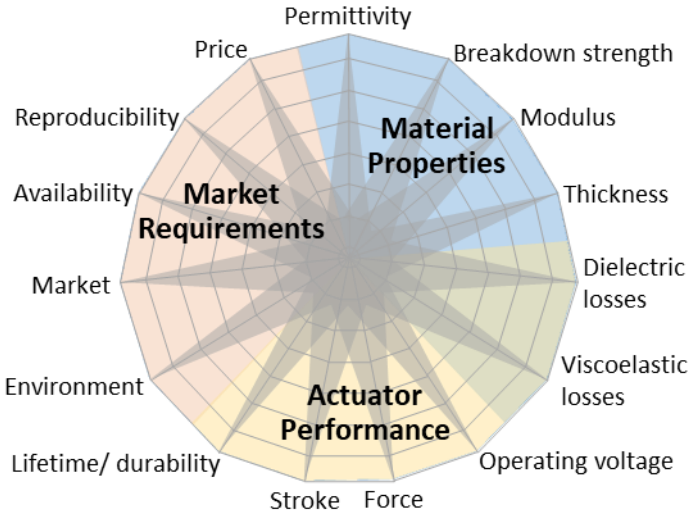

Figure 2.11: Radar chart demonstrating the equivalent importance of parameters of the elastomer for a successful actuator system design [cf. 70]. The parameters are grouped in market requirements (red) and material properties (blue), which overlap actuator performance (yellow).

2.3.1 Elastomers

The elastomer is very important for the performance of DEAs. Therefore, several different materials have been studied. The main physical requirements for a good actuator performance are being soft (< 20 MPa), exhibiting a high relative permittivity (> 2), as well as a high breakdown strength (> 100 V μm^{-1}) - the latter of which is mostly dependent on the other two properties [74]. For commercialization, the parameters mentioned in Figure 2.11 need to be considered as well. According to equation (2.3) a very low Young's modulus seems to be favorable for high actuation strain. However, this is only true under certain boundary conditions (free elastomer boundaries and no load). Under the conditions of a DEA system utilizing a biasing mechanism, the actuation strain is mainly dictated by the biasing mechanism and the Young's modulus becomes secondary. In this case, a low Young's modulus even becomes counterproductive resulting in a lower force difference as shown in Section 3.4.

The most promising material candidates, also studied in recent literature, are silicone, polyurethane, and acrylic elastomers. A comparison of the materials and data for *Wacker's Elastosil®* film, which is used within this thesis, are shown in Table 2.1. This table can only give a rough overview, due to the material properties being strongly dependent on the test conditions. In addition, natural rubber is studied in the literature, however more likely in the context of generators [30].

The material mainly used in research labs is an adhesive tape from *3M* called *VHB*, which is the most popular representative of acrylic elastomers. The reason for its popularity is the commercial availability as a film and the simple processing, rather than outstanding material properties. It can easily be attached to support frames after being stretched and, for example, carbon black powder sticks to it as electrodes due to the adhesive nature of the tape [75]. In terms of material properties, its main advantages are being highly stretchable, breakdown field, and thus very high actuation strains of up to 380% [9,76]. However, acrylic elastomers exhibit a strong viscoelastic behavior, which causes creep and low actuation speed. In addition, it exhibits frequency dependent and high mechanical losses during cyclic actuation [76]. A study of the dynamic response speed reveals that the performance of a *VHB* based actuator drops down to 20% only at 10 Hz compared to quasi-static actuation [25]. Another drawback is time dependent drift between device strain and

capacitance, which limits the accuracy of self-sensing approaches [77]. Polyurethane also suffers from high viscoelastic behavior, displaying similar drawbacks. However, due to its high Young's modulus and high relative permittivity, it demonstrates the highest actuation pressure [8].

Table 2.1: Comparison of different elastomer materials. Values reported may depend on test conditions such as the strong relation between breakdown field and applied strain or Young's modulus, respectively.

Elastomer	Young's modulus [MPa]	Breakdown field [V µm^{-1}]	Relative permittivity	Response speed
Acrylic (3M VHB 4910)	0.2…3 [37]	~55…412* [78]	4.8 [37]	ms to s
Polyurethane	17 [37]	~160 [40]	7 [37]	ms to s
Silicone	0.1…1 [37]	~80-130 [75]	2.8…3.7 [37]	µs to ms [13]
Silicone (Elastosil® Film)	1 [75]	80…100 [79]	2.8 [79]	µs to ms [13]

**** Depending on strain***

Unless very high actuation strains (> 80%) are needed, silicone is the material of choice for commercial DEA applications. Compared to acrylic elastomers it exhibits high stability over a wide temperature range, significantly lower viscous losses [75,76], and thus allows high-speed actuation up to the kHz-range [25]. The low creep, fast response, and a direct strain-to-capacitance relationship allows very low errors (<1% static [77] and <5% dynamic [14]) in closed-loop position control utilizing self-sensing. In addition, a high quality silicone film (*Wacker Elastosil®* film [79]) with precisely controlled thickness is commercially available, which enables the manufacturing of DEAs with repeatable performance and high reliability. In terms of fatigue, both, silicones and acrylics have proved several million cycles of actuation [25,80,81].

2.3.2 Electrodes

Flexible electronics with flexible printed circuit boards based on a polymer covered with conductive paths are already state-of-the-art technology. However, flexible in this case

means bendable rather than stretchable. The requirements for DEs are much harsher. Flexible, or rather compliant, in terms of a DE means that the electrode is able to stretch at least 100% without losing the conductivity (typical resistance in the kΩ-range). The necessary conductivity depends on the intended reaction speed of an actuator or the intended sampling rate of a sensor. Conductivity, or rather resistivity, is linked to the actuation speed via the RC-circuit time constant, which is the product of the serial resistance and the capacitance [53]. After five times the time constant the DE is considered to be completely charged (> 99%) and thus builds up the full Maxwell pressure in the actuator case. For example, a DEA with a capacitance of 1 nF and serial electrode resistance of 200 kΩ, can still be driven at 1 kHz. However, the mechanical time constant, which is typically larger than the electrical one, also needs to be considered.

While the electrical properties of the electrode could vary within a wide range (up to MΩ) the limits for the mechanical ones are much tighter. Beside the fact that the electrode must be able to undergo strains larger than 100%, it needs to be as soft as possible, not impede the deformation of the elastomer. Therefore, the best electrode is no electrode as, shown by Keplinger *et al.* [82], when repeating Röntgen's experiment with charges directly sprayed onto the elastomer from high-voltage electrode tips. However, this concept is not suitable for dynamic actuation or sensor applications because it does not allow the DE to be charged or discharged efficiently [83]. A trade-off between conductivity and low mechanical stiffness (on the elastomer film) must be made.

Two approaches have been studied in the recent literature to address this problem: Either the softness is achieved structurally (patterned electrodes) or by using soft electrode materials. Patterned electrodes typically provide very high conductivity, due to the use of thin, metal films (thickness in the nm-range). However, the patterns only provide softness in a single direction, e.g., spirals for out-of-plane [84] or meandering pattern [85] and corrugated surfaces [86] for in-plane direction. Soft, or at least isotropic compliant, electrodes are made of conductive particles (mostly carbon black powder), which are deposited on the elastomer surface. When working with *VHB* the carbon powder can simply be dusted onto its sticky surface, which is quick but not very reliable. Another quick way is to bind the conductive particles in an oil or grease. This allows easy patterning just by using a paint brush, but still does not allow for making reliable electrodes. The big

advantage of both methods is that the stiffness impact on the elastomer can be neglected. The most common version for reliable, soft electrodes is binding the conductive particles into an elastomer matrix, which can be cured after application and thus is bonded together with the elastomer. This allows long-term, stable electrodes with a high resistance against mechanical abrasion, especially if the elastomer matrix of the electrode and the dielectric are from the same material. However, these advantages are incurred by a stiffness impact on the elastomer, which in this case is no longer negligible. A comprehensive overview on electrodes, further detail on the aforementioned, and additional novel concepts are summarized by Rosset and Shea in [83].

The actuators manufactured within this work use an electrode, which is based on carbon black bound into a silicone matrix. For a reliable actuator manufactured in mass production the electrode needs to fulfill several additional requirements, besides the above mentioned mechanical and electrical properties. The requirements are listed in Figure 2.12 for an electrode applied via screen-printing, which is used for actuator manufacturing within this thesis and described in detail in Section 2.4.

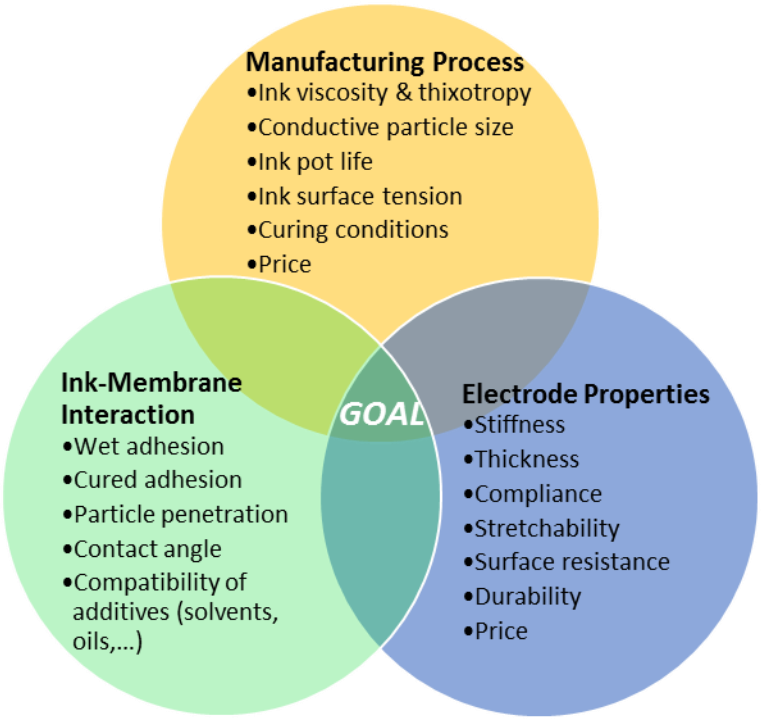

Figure 2.12: Parameter space for an electrode ink used in a screen-printing process.

2.4 Manufacturing of membrane dielectric elastomer actuators

Since elastomer films (for example *3M's VHB* or *Wacker's Elastosil*) are commercially available, the motivation for casting one's own film is significantly reduced and thus not discussed. However, there are still a large variety of methods to apply the electrode. Beam evaporation, cathodic sputtering, or electroplating are just a few methods, which are used for metal electrodes [83]. When using carbon based electrodes typically methods like pad printing [87], spin [44] or spray [45] coating through a shadow mask and screen- [58] or inkjet-printing [88], are used. There are even more advanced methods for high resolution electrode patterning. They utilize blade casting of an electrode film combined with laser appellation structuring, and afterwards plasma bonding of the electrode film onto the elastomer [89]. The author chose screen-printing for the manufacturing of the DEAs, knowing it is typically used for mass production. However, screen-printing is still a comparatively easy process, which can be used for prototyping as well, and allows for high repeatability.

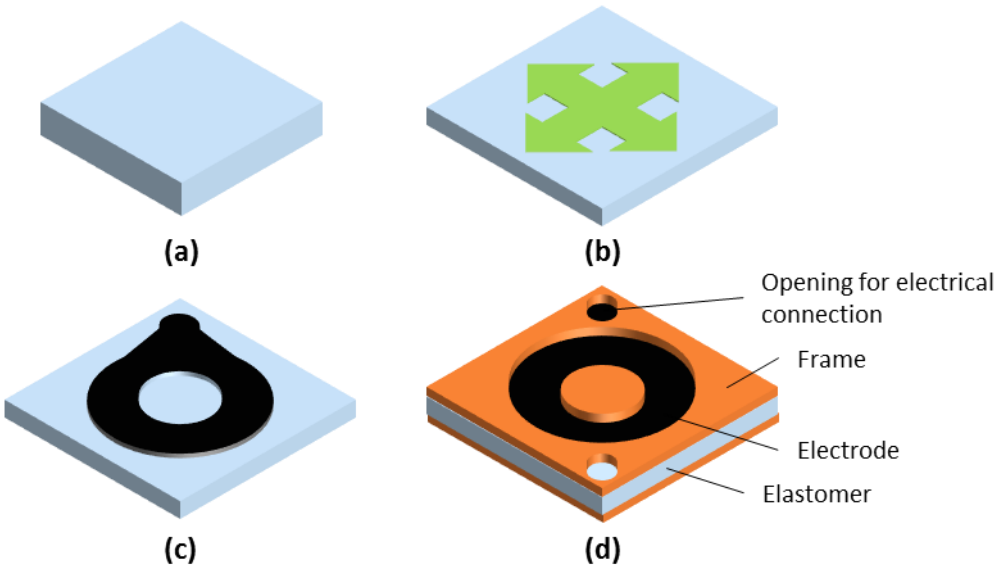

Figure 2.13: Schematic of the process flow for manufacturing a COP-DEA showing the progress after each manufacturing step. (a) Initial sheet of silicone film, (b) silicone film after pre-stretch, and (c) screen-printing of electrode-rings and (d) frame material on both side of the film.

In the following paragraph, the manufacturing process of the DEAs, which are studied in this thesis, is described. The DEAs are based on *Wacker's Elastosil 2030* film with a thickness of 50 µm (Figure 2.13 (a)) and carbon black electrodes. The manufacturing process starts with the removal of the film backing layer and its mounting on a self-made stretching device. Pre-stretching of the elastomer film (see Figure 2.13 (b)) is important in order to improve the DEA's performance [78], to increase the breakdown voltage [90], and to prevent the film from sagging within the metal frame - which supports the handling during manufacturing. In particular, a biaxially homogenous pre-stretch of 20% is applied to the membrane, if not stated differently. After this, the film is clamped in-between two metal frames to maintain the pre-stretch and to allow for easy handling. After pre-stretching, electrodes are applied on both sides of the film using a screen-printing process (see Figure 2.13 (c)). A subsequent heat curing process results in the evaporation of solvents within the electrode ink and crosslinking of the electrode with the silicone film. Afterwards, screen-printing is used again to apply a heat curable epoxide on both sides, acting as a mechanical frame (see Figure 2.13 (d)). Normally, this process is not done for a single DEA only. Screen-printing allows batch processing of multiple DEAs simultaneously. The two screens used for the electrode and the frame, to manufacture 12 SIP-DEAs in one process, are shown in Figure 2.14.

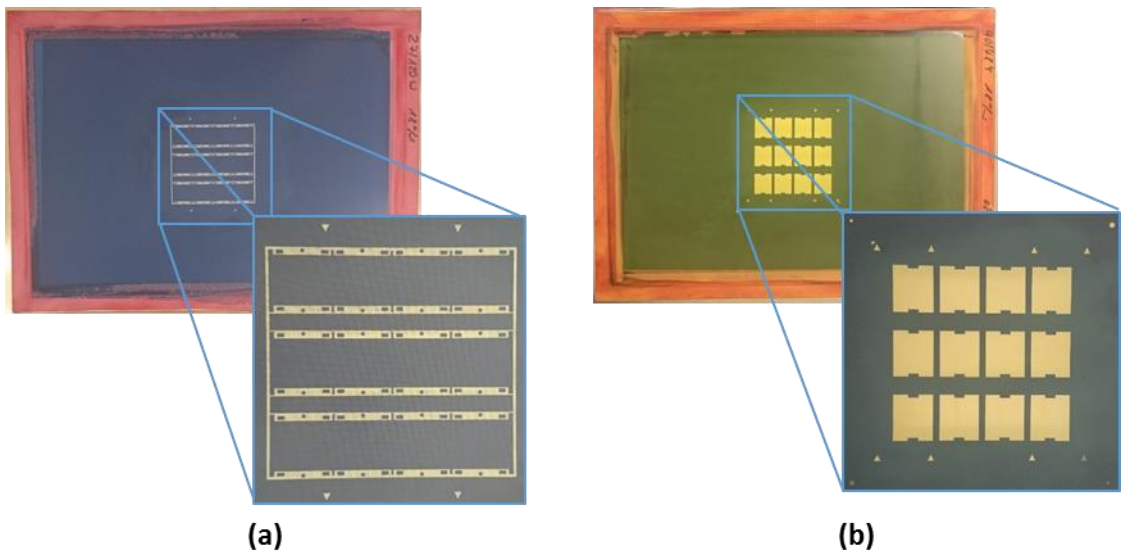

Figure 2.14: Screens for printing (a) the frame and (b) the electrode of SIP-DEAs.

The most critical process is the screen-printing of the electrodes. Apart from the electrode properties, which are mentioned in Figure 2.12, the printing parameters are also important. They can be separated by processes control parameters such as print speed, blade material and pressure, and number of print runs, as well as screen parameters such as mesh type, number of threads per inch, and emulsion film thickness to name just a few. All of the above directly influence the thickness of the electrode and thus its mechanical impact on the elastomer. In order to have a good control on these parameters, the semi-automatic screen-printer *ESC-AT 60P* (see Figure 2.15) is used. The electrode ink itself is a mixture of *Wacker's RTV-2* polydimethylsiloxane (PDMS), *Orion's Printex XE2* carbon black, and *Wacker's AK 100 K* silicone oil. These components are mixed in the ratio of 50%wt, 20%wt, and 30%wt, respectively. In an effort to make the mixture screen printable *VD 60* solvent and *VM1* additive (both are from *Coats Screen Inks)* are added next. The additive and the solvent are used to control the viscosity of the ink, which has an impact on the electrode thickness, too. An *EXAKT* 3-roll mill and a planetary mixer manufactured by *Thinky* are used to homogenize the ink. More details on the screen-printing process and an investigation on the printing parameters can be found in [58].

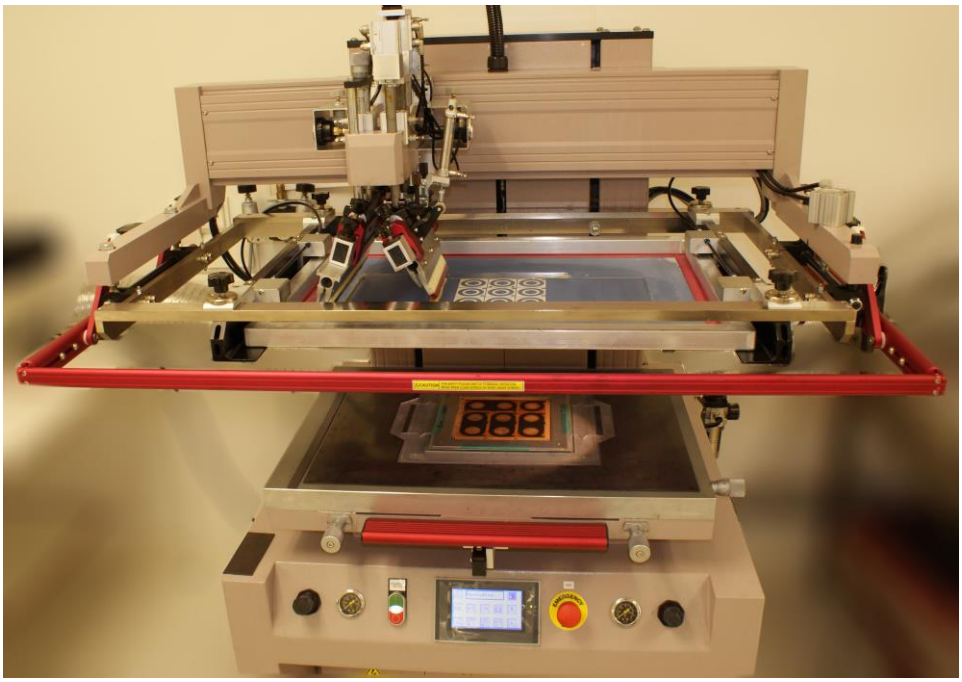

Figure 2.15: Semi-automatic screen-printer ESC-AT 60P with a screen for COP-DEAs and completely printed COP-DEAs underneath.

2.5 Characterization of dielectric elastomer actuators

For the design of DEA systems, it is necessary to have accurate information about the characteristic of the DEAs and the mechanical parts used. Especially, the force-displacement characteristic need to be known. In terms of the DEA, this characteristic needs to be measured at different applied voltages. The constant voltage (CV) test is used to gain this information. During this test, the DEA is cyclically deflected from zero to a maximum strain value with a constant voltage applied, while the deflection force is measured. The test is typically performed at 0 V and the maximum allowed voltage V_{max}. In order to perform a detailed study of the DEA, intermediate voltages are chosen as well. The area between the zero and the maximum voltage curve defines the work area of a DEA. When characterizing a COP-DEA, the outer frame is clamped, while the center disc is deflected (see Figure 2.16). For the SIP-DEAs, one end is fixed, while the other one is pulled away - stretching it. The CV test is used to characterize the potential work area of a complete DEA system too. Therefore, the DEA system is fastened and the output side of the DEA system is deflected at different voltages. Additionally, this test can be performed to characterize mechanical parts such as springs, etc. The results of a CV test for a COP-DEA are shown in Figure 2.17.

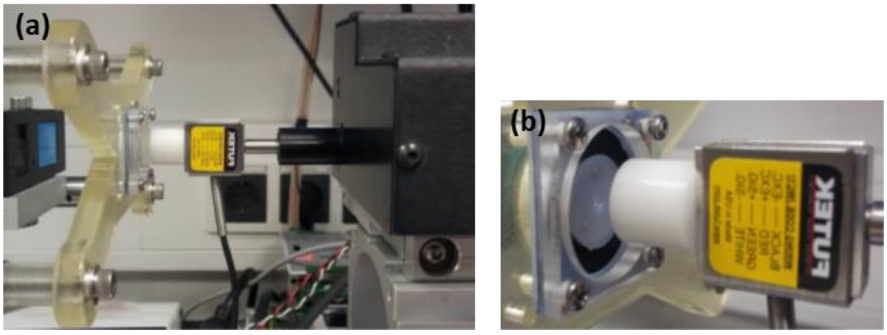

Figure 2.16: Close-up photos of the low force setup shown in Figure 2.18. (a) Showing the laser sensor, the DEA mounting, and the motor. (b) Photo of the pushrod with a load cell attached before deflecting a COP-DEA. The HV amplifier is connected to the screws, which are screwed through the electrode for electrical connection.

Another interesting performance parameter of DEAs is the blocking force, which is measured by the constant position (CP) test. Within this test, the stretch of the DEA stays

constant and the voltage is cycled, while the force is measured. The force difference between zero and the maximum voltage applied equals the blocking force (see Figure 3.18 for an example).

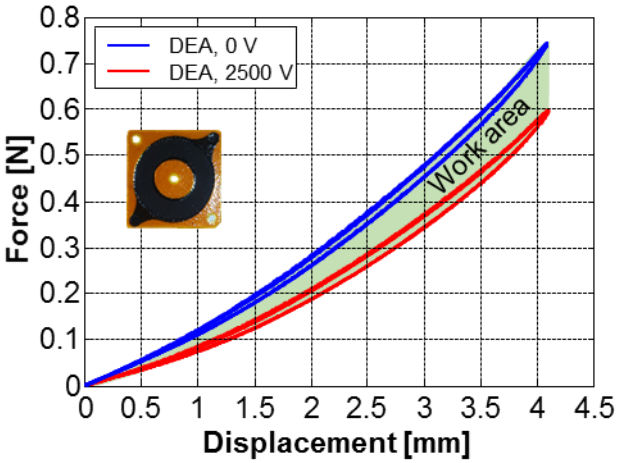

Figure 2.17: Results of a CV measurement of a medium-sized D25 COP-DEA (see inset and Table 3.2). Light green area indicates the work area of this specific DEA.

To perform the characterization tests mentioned above, two similar setups are used within this thesis. The first one is used for the basic characterization of single elements or small, multi-layer modules, and therefore low forces, while the other one allows also the characterization of larger stacks and the high-force actuator of Chapter 4. They both consist of a linear motor, a load cell, a laser displacement sensor, and a voltage amplifier (see Figure 2.18 (a)). All components are connected to a *Windows* computer running *LabVIEW* via a data acquisition board (DAQ) from *National Instruments* (*NI*). This allows the control of the components as well as data acquisition. The load cells are connected via an additional *NI* full bridge signal-conditioning module (named amplifier in Figure 2.18).

The **low-force setup** (see Figure 2.18) allows precise measurements in the range of ±10 N, which is limited by the linear electromagnetic motor (Model *ANT-25LA*) from *Aerotech*. An *Aerotech Ensemble CP* controller allows operating the motor. It accepts analog inputs for speed and stroke definition and provides an analog output for position feedback. A *Futek* load cell (Model *LSB-200 5 lb*), a *Keyence* laser displacement sensor (Model *LK-G37*), and a *Trek® Model 610E* voltage amplifier complete the setup. All

components are mechanically mounted to a *Thorlabs* optical breadboard for precise alignment.

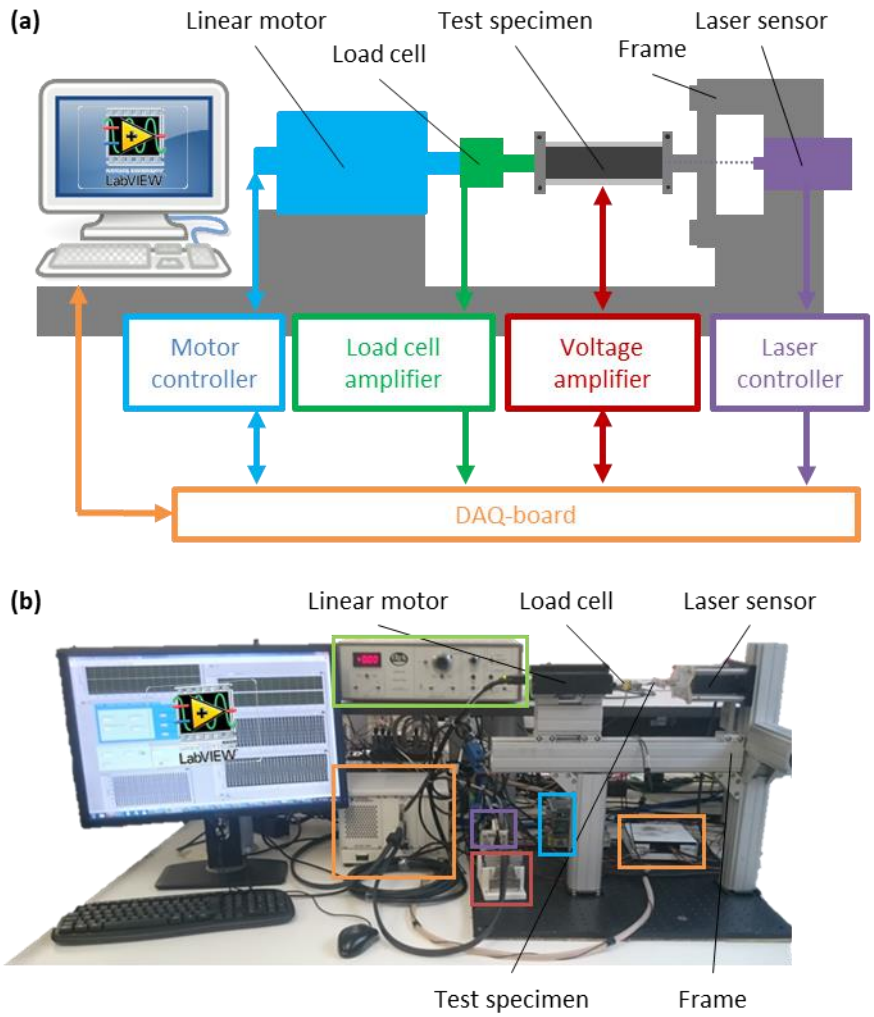

Figure 2.18: (a) Schematic sketch and (b) photograph of the low force test setup used for characterization.

The **high-force setup** looks different (see Figure 2.19), but offers similar functionality. The main difference is that the components used are designed for higher forces. The load cell is a *Futek LCM 300* (50 lb), and the motor from of the *TA.XT-Series* from *Stable Micro Systems*. In this setup, the load cell is limiting the force range to ±223 N. Additionally, a different voltage amplifier from *Ultravolt (4HVA24)* and the laser sensor *LK-G87* from *Keyence* are used. However, this setup has one major drawback. At such high forces, the stiffness of the setup (in comparison to the measured components) is not negligible anymore. This error is compensated for in different ways for the two measurement modes

shown in Figure 2.19 (b). In method (1), for characterizing test specimens, such as DEAs or springs, the error is compensated by design. The laser is mounted on top of the motor arm and aims at a fixed surface. Therefore, it moves with the motor arm and only measures the actual movement, unaffected by any distortion of the motor arm. This configuration is also used to measure the overall stiffness of the setup, which is k_{SU} = 153 N mm^{-1}. The method (2) is used to characterize the whole actuator system. In this case, the laser is aimed onto a reference surface (dashed box in Figure 2.19 (b)), which moves with the actuator stroke. However, the generated force distorts the motor arm as well. Assuming linearity, this distortion can be calculated by dividing the measured force by the stiffness of the setup then subtracted from the laser measurement. In addition, the stiffness of the setup also influences the stiffness of the load, which acts onto the actuator. The actual load stiffness k_L can be calculated as follows:

$$\frac{1}{k_L} = \frac{1}{k_{LS}} + \frac{1}{k_{SU}}, \tag{2.4}$$

with, k_{LS} stiffness of the load spring.

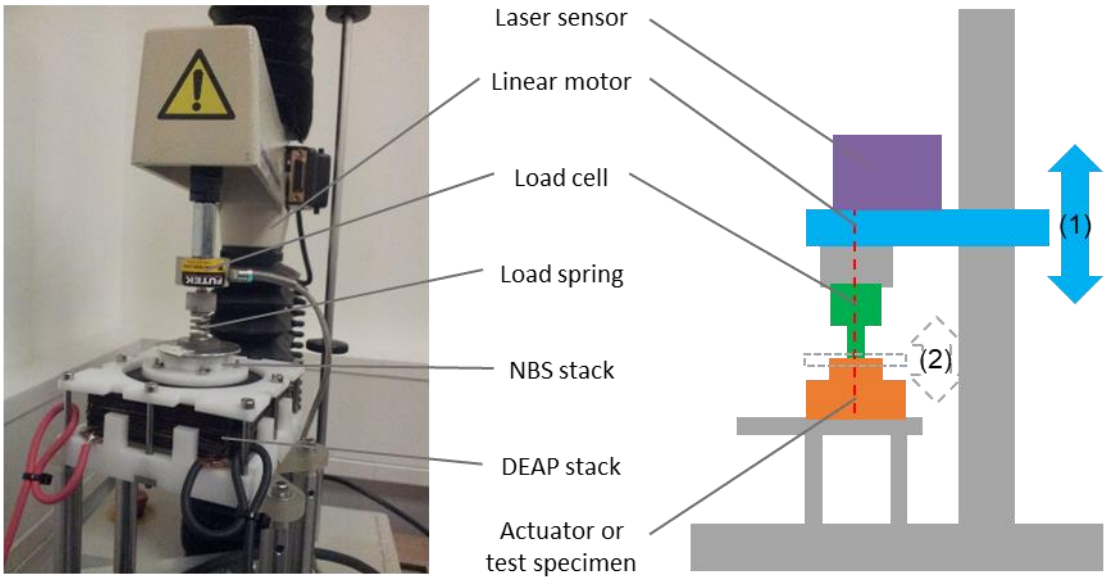

Figure 2.19: (a) Photo of the high-force characterization setup measuring an actuator from Chapter 4 including load spring (Laser missing on photograph). (b) Schematic of the setup showing two operational modes: (1) Motor is moving to deflect a test specimen and (2) actuator is activated to measure generated force and stroke.

Chapter 3 Dielectric elastomer actuator design

For the development of high-performance DEA systems, it is important to understand the mechanical and electrical properties of every element involved, such as DEA, biasing, or external load, and how they interact with each other. It is essential to combine membrane DEAs with an appropriate biasing mechanism to optimize their performance. Therefore, the most important biasing mechanisms (mass, liner spring, magnet, and non-linear elements with negative stiffness range) and their influences are described in Section 3.1. Additionally, a systematic approach to model the interaction using force-equilibrium-plots for quasi-static conditions is described.

The most effective biasing is a combination of a negative-rate bias spring (NBS) and a linear spring. However, the NBS needs to have a certain force-displacement characteristic for a specific DEA. Therefore, an efficient way to design an NBS based on buckled beams is presented. The method allows the calculation of all NBS parameters (needed for manufacturing) to achieve a desired force-displacement profile. In addition, important parameters for space requirements and maximum allowed material stress can be freely chosen. This method is described in Section 3.2.

For the DE itself, a very important design parameter is the material. As one can directly see from equation (2.2), the Maxwell pressure is directly related to the material-dependent relative permittivity ε_r. As the influence of this parameter is already described in detail in [4,8], and this work focuses on the use of commercially available materials, this parameter has been chosen not to be studied. The second important parameter is the DEA geometry, which is studied in detail in Section 3.3 for COP-DEAs with various different cases. Scaling laws for force and stroke output are extracted from the investigation, and a simplified prediction method for the force-displacement characteristic of such DEAs is developed.

Finally, in Section 3.4 a systematic design process for DEA systems is introduced. It is shown how design parameters (biasing and geometry) can be used to adapt a DEA system to specific load cases. The introduced method is then used in Chapter 4 and Chapter 5 to design high-performance DEA systems.

3.1 Actuator modeling and the influence of biasing elements

Hodgins *et al.* [91] showed that the performance of membrane DEAs strongly depends on their biasing mechanism. Especially the use of bi-stable mechanisms may boost their performance by, e.g., increasing the stroke by an order of magnitude compared to a linear spring [92]. Therefore, the interaction of a biasing mechanism and the DEA needs to be studied and understood before designing DEA systems with optimized performance. This section describes a systematic modeling approach for DEA interaction with passive mechanical loads using the example of a DEA coupled with a linear spring and a buckled beam based NBS (see Section 3.2). This combination is very common for DEAs with high actuation stroke. The result is a graphical solution, which allows predicting the stroke output and the resulting force difference of such DEA systems.

The model is based on an approach using the fundamentals of applied mechanics. It applies the laws of statics to model the system behavior of a DEA coupled with any other mechanical element, such as a spring. The fundamentals of statics assume that the sum of forces and moments equal zero. This implies that there is no (or only slow) movement in the system, therefore, limiting the approach to quasi-static conditions for any electrical loading condition of the DEA. It needs to be pointed out that time dependent effects like viscoelasticity or charging are neglected, which is sufficient in most cases. Basic approaches of this methodology have already been used by several scientists studying membrane DEAs, for example in [34,40,93,94]. However, in this thesis a systematic and generalized approach is presented, which is universal and allows application to other smart materials as well. In addition, it focuses on matching the actuator element with a biasing force. This leads to a powerful and systematic tool to design DEA systems for intended applications, as shown in Section 3.4, when combining it with the NBS modeling in Section 3.2 and the DEA performance prediction in 3.3.

In the following section, this systematic approach is used to show the influence of different common biasing elements on the force and stroke output of COP-DEAs. The concept always follows four steps, which are typically used when solving a quasi-static problem:

(1) Define or measure material/ element model for involved parts

(2) Define global coordinate system and set up kinematic relations

(3) Draw free body diagrams (FBD) and form equations of force equilibrium

(4) Solve problem: Predict stroke output and resulting force difference

(1) Material/ element model

This kind of model needs to describe the relationship between force and displacement. It can be expressed as an equation for simple elements, such as linear springs, or be represented by an empirical measurement for more complex elements, such as DEAs. Due to the complexity of smart materials, measurements are preferred, and the modeling problem is solved graphically. For DEAs, the CV measurements described in the previous characterization Section 2.5 are used. Figure 3.1 (b) shows a qualitative result of such a measurement for a COP-DEA. The index 'D' is used to relate the quantities displacement x and force F to the DEA. The force-displacement curve of such DEAs is point symmetric around the origin, has a parabola-like shape in the first quadrant, and less force is needed to displace the DEA with a HV applied, due to the Maxwell pressure, which reduces the mechanical stress of the pre-stretch within the membrane. The hysteresis of the DEAs, which can be seen in Figure 2.17, is neglected.

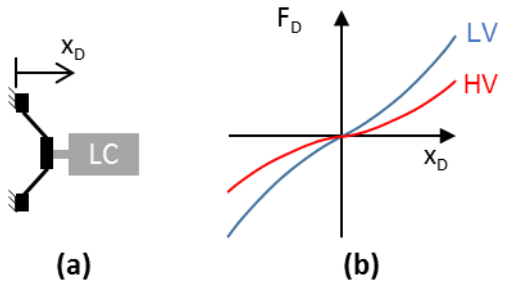

Figure 3.1: (a) Sketch of the DEA measurement with load cell (LC) and coordinate system and (b) qualitative results for a CV measurement and applied a low voltage (LV) and a high voltage (HV).

The sketch of the measurement setup shown in Figure 3.1 (a) is important, because it defines the coordinate system of the measurement and the direction of the measured force. Per definition, tensile forces measured by the load cell are assumed positive and compression forces are negative. These conventions need also be considered during data recording, and help avoiding confusion when drawing the free body diagram. Figure 3.2 shows the same diagrams for the most common biasing elements with their indexes, namely a weight $'W'$, a linear spring $'S'$, NBS $'N'$, and a magnet $'M'$. The forces for the weight and spring can easily be described by linear equations instead of measurements, which is not easily possible for the other two.

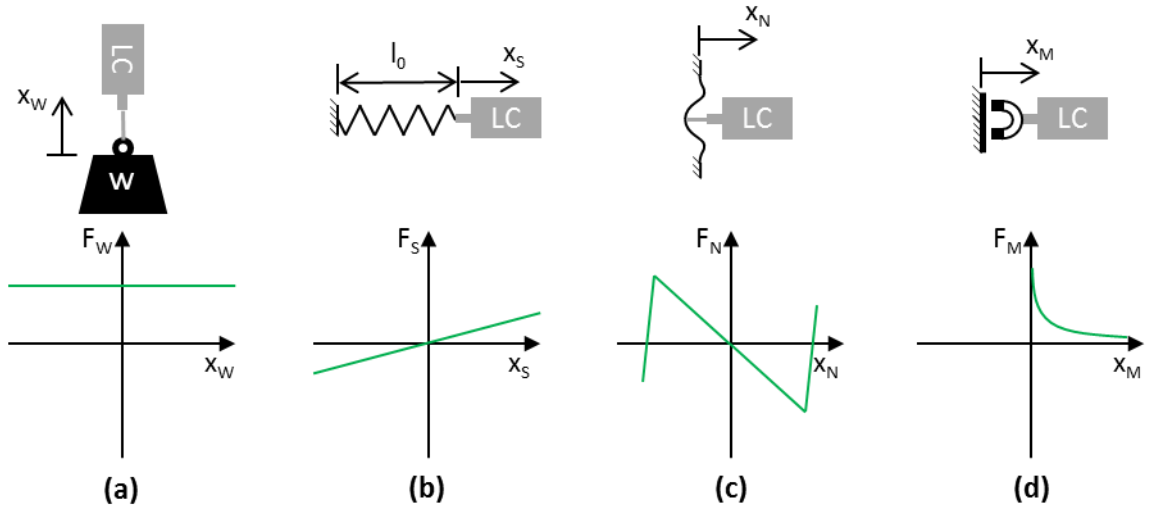

Figure 3.2: Sketch of the measurement setup (LC and biasing element) and the corresponding force-displacement characteristic of various biasing elements: (a) weight (mass), (b) linear spring with initial length l_0, (c) buckling beam based negative-rate bias spring, and (d) magnet.

(2) Global coordinate system and kinematic

From this step on, we start to consider the combination of the DEA with the biasing elements shown schematically in Figure 3.3. This figure also contains the local element coordinate systems, which must be in accordance with the ones of the material models in terms of direction and position. The offsets O between the coordinate systems and spacers S, which connect the elements rigidly, are shown, too. The indices of O and S indicate which elements/ coordinate systems are connected. The aim of step two is to unify the local coordinate systems to a single global one.

We start with the definition of the global coordinate system x (see Figure 3.3). It can be freely chosen and is defined right from the DEA in this example with an offset of $O_{D,X}$, relative to the DEA coordinate system. In the case of a real actuator, the origin of the global coordinate system could be, for example, a reference surface of the actuator casing or a zero position of a push rod. The next step is to set up equations for the relation between the individual and the global coordinate system based on the direction, the offsets O and the spacers S shown in Figure 3.3:

$$x_D = x + O_{D,X} \tag{3.1}$$

$$x_N = x + O_{D,X} + O_{N,D} - S_{N,D} = x - C_N \tag{3.2}$$

$$x_S = x + O_{D,X} + O_{N,D} + O_{S,N} - S_{N,D} - S_{S,N} - l_0 = x - C_S \tag{3.3}$$

The absolute terms C_N and C_S just merge all constants for the NBS and the spring, respectively.

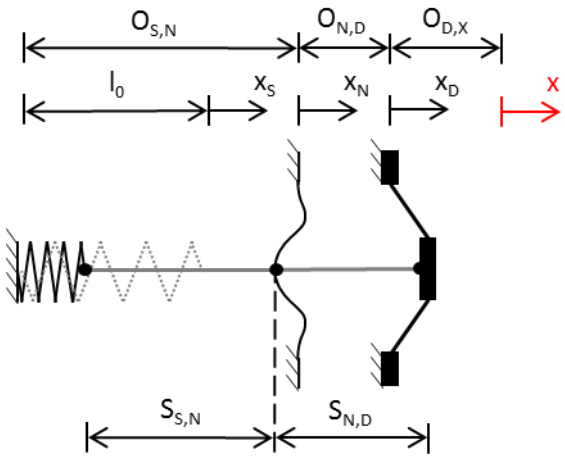

Figure 3.3: Schematic sketch of the system with global coordinate system x and individual coordinate systems of the elements, offsets O of the coordinate systems to each other, lengths S of the rigid spacers, and the initial spring length l_0.

(3) Free body diagram and force equilibrium

After unifying the coordinate system, the next step is to sum up the forces of the individual elements. Therefore, we have look at the FBD shown in Figure 3.4. Forces are vector quantities, and thus the direction needs to be considered in addition to the value. The force arrows in the FBD must point in the positive force direction for each individual element defined in the material model. This might be a bit confusing, when looking at the DEA force F_D, as it is pointing in the direction of deflection and not in the direction it is actually acting. However, the direction of the force is defined in the material model and its

measurement and follows the convention made in Section (1) 'Material/ element model' of this chapter.

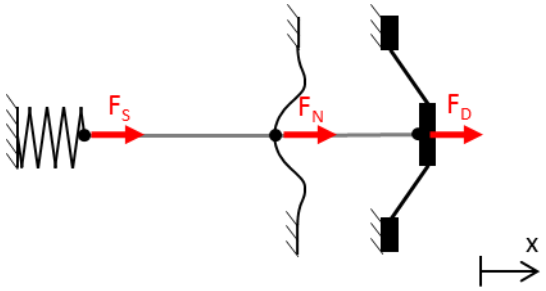

Figure 3.4: FBD showing the individual forces acting onto the connecting rod.

As we consider static conditions the sum of forces needs to be zero. To set up the force equilibrium in the direction of x all forces need to be summed up, while the direction of the arrow indicates their signs. Forces in the direction of x are defined to be positive, which leads to:

$$\sum F_x = 0 = F_S + F_N + F_D \tag{3.4}$$

(4) Solution

For a graphical solution, all forces need to be drawn into one diagram. The equations (3.1) to (3.3) allow to describe all forces as a function of the global coordinate system x. To describe the movement of the system, when the voltage of the DEA changes, equation (3.5) can be used to describe the equilibrium between the DEA and biasing elements (NBS and spring):

$$F_D = -F_S - F_N \tag{3.5}$$

Figure 3.5 (a) shows again the material model of the NBS and the spring, however, in the global coordinate system. The sum of forces of the right side of equation (3.5) are plotted in the global coordinates system in Figure 3.5 (b). Due to the minus signs, the forces of the material model are mirrored on the x-axis. Both forces are also shifted relative to the origin by their C values of equation (3.2) and (3.3). For the spring, this shift can be interpreted as a pre-compression. The sum of both biasing forces and the DEA forces are plotted in Figure 3.5 (c). Typically, the DEA is deflected in one direction only, and therefore just the first quadrant of the material model of Figure 3.1 (b) is considered. The two intersection points ($x_{LV}|F_{LV}$) and ($x_{HV}|F_{HV}$) of the biasing elements and the DEA at LV and HV represent the two

quasi-static equilibria. When switching the voltage, the system jumps from one equilibrium to the other. Therefore, they can also be used to determine the stroke $\Delta s = x_{HV} - x_{LV}$ and the resulting force difference $\Delta F = F_{HV} - F_{LV}$. Figure 3.3 also shows an important design criterion for the biasing mechanism. Its force path needs to fit into the work area located between the two DEA curves.

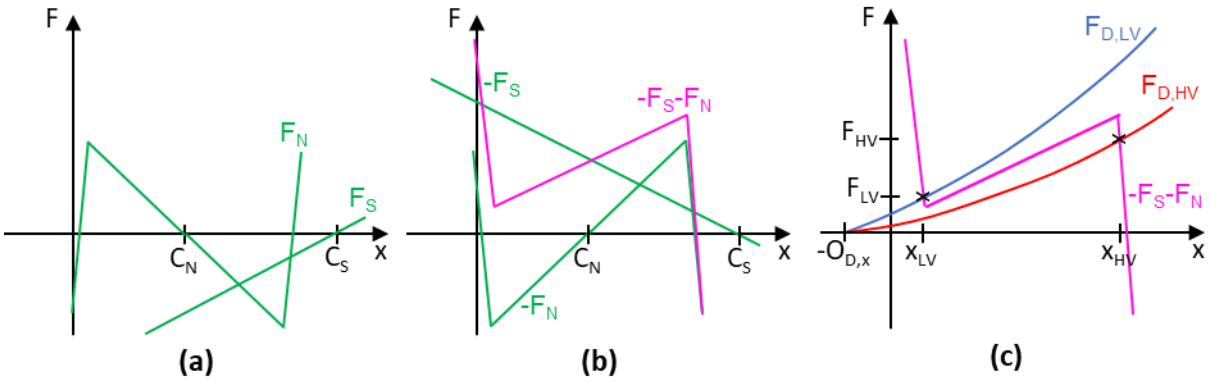

Figure 3.5: (a) Material model of spring and NBS in the global coordinate system and (b) inverted forces as well as the sum of them. (c) Force equilibrium plot of the summed up biasing mechanism force and the DEA at different voltages.

The example points out the importance of the combination of a NBS and a spring. To get an optimal use of the NBS it needs to be shifted on the x-axis and the force-axis as well. The shift on the x-axis can easily be done by selecting the right spacing between DEA and NBS. For the shift on the force-axis an additional force needs to be added, which is the pre-compression force of the linear spring. In addition, the spring can be used to fine-tune the slope of the negative stiffness branch of the NBS. Compared with other biasing mechanisms, the combination of a spring and the NBS gives the best performance (see Figure 3.6).

Each of the different biasing mechanisms shown in Figure 3.6 has its pro and cons. The **mass** is simple, offers a medium stroke, but adds mass to the system and thus eliminates one of the advantages of DEAs, namely being lightweight. The **spring** is simple as well, can be used for high frequency applications, but delivers the lowest stroke. The **NBS** by itself delivers high strokes, can be used for quick operation, but an additional hard stop is necessary as shown in [95]. In addition, the system becomes more complex, and an additional bias force is needed to gain the full performance. The **magnet** is relatively easy to implement and offers high strokes, too. However, it adds some mass to the system, and

an additional hard stop is needed (see Figure 3.6 (d)) to prevent the system from collapsing onto the metal surface. The stroke can even be further increased by adding a spring to the magnet-DEA system [96].

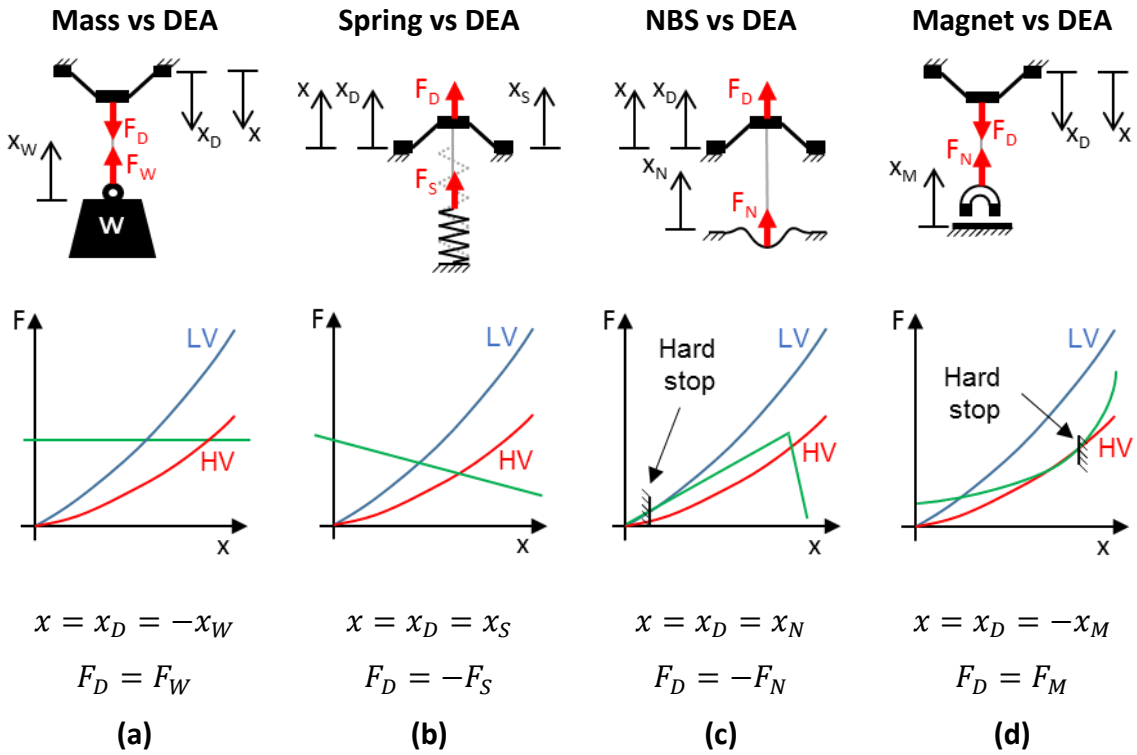

Figure 3.6: Comparison of different biasing mechanisms acting against a COP-DEA. The kinematic equation just considers the direction reflected by the algebraic sign and offsets/ spacers are neglected.

3.2 Negative-rate bias spring design

Apart from a magnet, a NBS is the most promising biasing mechanism to optimize the performance of membrane DEAs. Therefore, this section describes a very efficient design process of a NBS mechanism based on a pre-compressed buckled beam. The design process allows calculating the geometry and pre-compression of a buckled beam with a desired force-displacement characteristic. In addition, the maximum available installation space and the yield strength of the material used is considered. This section is based on the master thesis of Bruch [97] and conference paper [98].

The buckled beam with its dimensions (initial length l_0, width w, thickness t, and compressed length l) is shown in Figure 3.7 (a). Several approaches trying to analytically

describe the nonlinear reaction force F (see Figure 3.7 (c)) of a centrally loaded beam undergoing symmetrical bending modes (see Figure 3.7 (b)) have been reported in the recent literature, for instance in [99–101]. These models are based on classic Euler-Bernoulli beam theory, which is typically used for small deformation only and thus neglecting the kinematic nonlinearities. This results in increased deviations between the model and the experiment for large deformations, which are the case when using the buckled beams as a NBS. For more accurate modeling, FE simulations can be utilized, as has been done, for instance, by Follador *et al.* in [102] to design a bi-stable DEA system. However, FE simulations are very time-consuming.

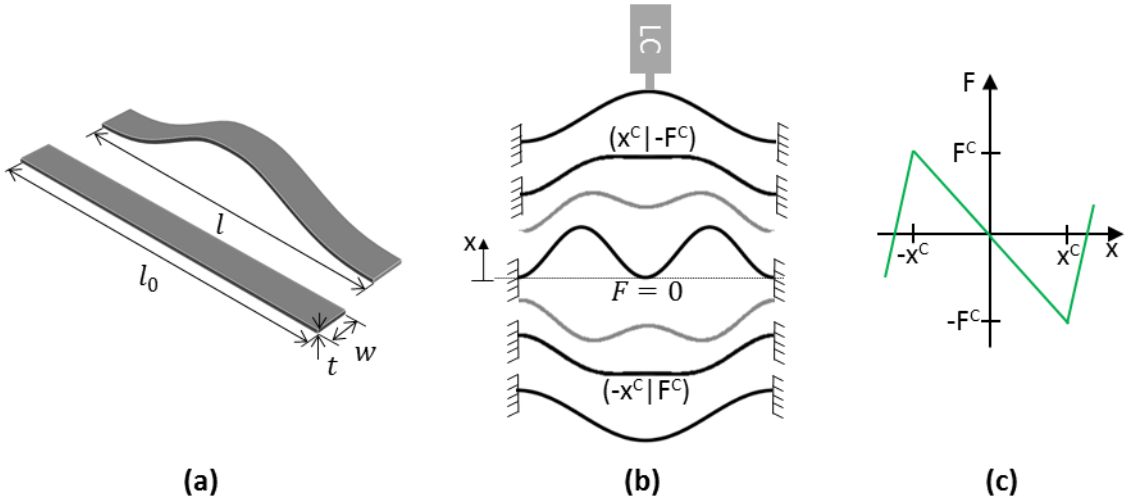

Figure 3.7: (a) CAD model of a beam in a flat and a pre-compressed configuration showing the nomenclature. (b) Symmetrical bending mode at different deflections for a centrally loaded buckled beam in-between the two stable equilibria. (c) Schematic of force-displacement plot with critical forces and displacements marked with F^c and x^c, respectively.

Therefore, an efficient design method based on a FE simulated parameter study, which is only performed once, is developed. With this parameter study, the influences of each geometry parameter and the pre-compression rate *c* (see equation (3.6)) on the force-displacement characteristic as well as the maximum mechanical stress of a pre-compressed buckled beam are studied.

$$c = \frac{l}{l_0} \tag{3.6}$$

Polynomial fits of the found relationships together with a systematic and stepwise approach allows for the calculation of the beam geometry for a given force-displacement characteristic described by $\Delta F = 2F^c$ and $\Delta x = 2x^c$ analytically.

3.2.1 Simulation model

Apart from the geometry parameters and the material used, the actual bending mode influences the force-displacement characteristic, too. In this work, only the symmetric 'M'- or 'W'-shaped bending mode is considered, which is enforced by the central loading condition in combination with a linear guiding causing a horizontal tangent at the center of the beam during all bending states (see Figure 3.7 (b)) [99,100].

The FE model for the buckled beam parameter study is implemented in *COMSOL Multipysics® 5.3* by means of the solid mechanics module. A Saint-Venant-Kirchhoff model is used, which combines a linear-elastic Hookean material behavior with a non-linear Green-Lagrange deformation. This model cannot account for plastic deformations, which would also cause a hysteresis in the force-displacement characteristic. This hysteresis is undesired and therefore, the maximum occurring material stress needs to be considered too. This stress is expressed by the second Piola-Kirchhoff stress in the simulation. A detailed description of the FE model as well as the used boundary conditions are documented in [97].

The FE model is validated with several experiments measuring the force-displacement characteristic of buckled beam NBSs. An exemplary comparison of a beam with different compression rates is shown in Figure 3.8. In addition, calculated curves based on the analytical model of Vangbo [100] are shown. The simulated and the measured data agree very well especially in the important region of the negative stiffness, while the analytical model predicts a higher negative stiffness. The deviation (rounding) of the measurement data in the region close to the critical force value is a result of the imperfections in the measurement setup, for instance, imperfect alignment. However, the major error source is the clamp material (3D printed material *VEROCLEAR RGD810*) and the clamping of the beam itself, which deviates from the boundary condition of an infinitely stiff fixation in the simulation. This is discussed in detail in [97] and proved by adding the clamps to the simulation. However, the simulation gets more complex and time-consuming by adding the clamping and thus it is not used in the parameter study.

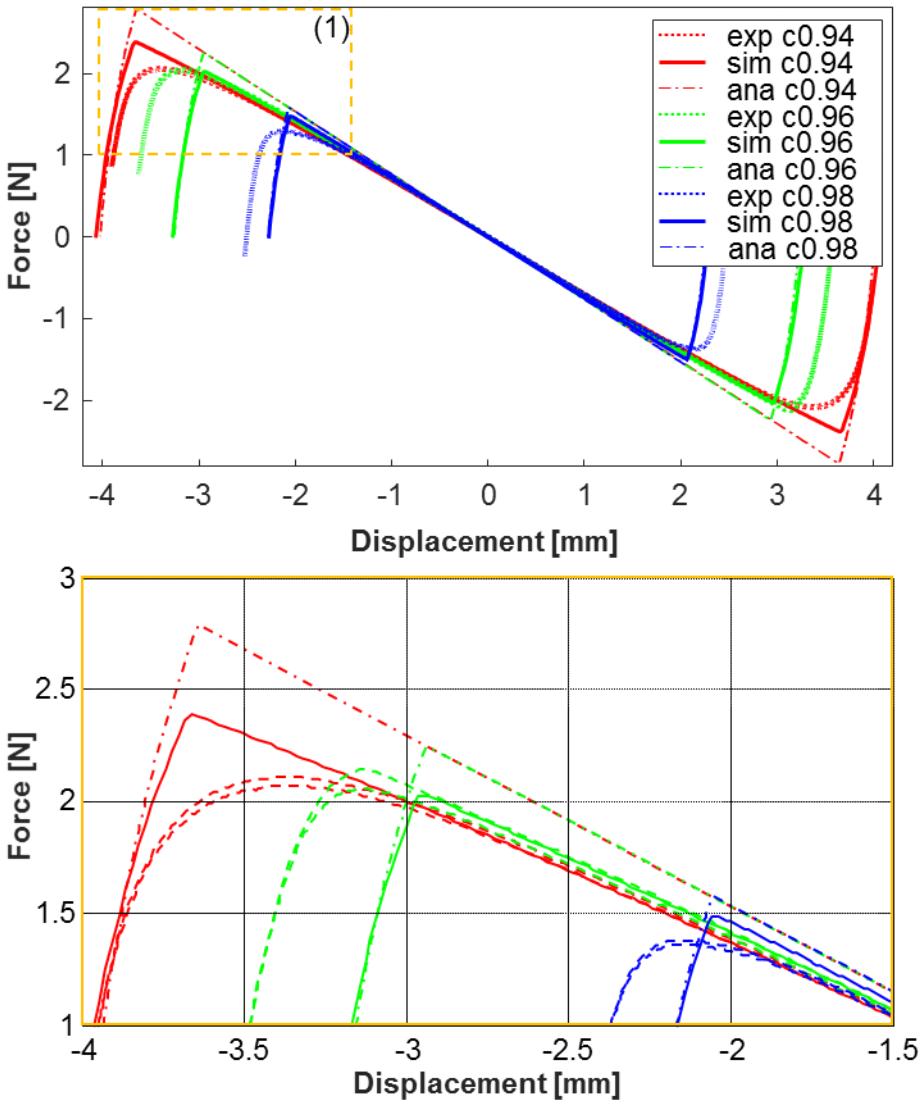

*Figure 3.8: Comparison of the **exp**erimental (measured with low force setup described in section 2.5), **sim**ulated and **ana**lytically calculated (model of Vangbo* [100]*) force path of beam NBSs under different compression rates of 0.94, 0.96, and 0.98.*

3.2.2 Parameter study

For the parameter study, the geometry parameters of the beam (width w, thickness t, and compressed length l) as well as the pre-compression rate c are varied and the corresponding force-displacement characteristic is measured. Note that the initial beam length l_0 is not considered, due to it resulting in the compressed length l and the compression rate c (see equation (3.6)). In each measurement series, just one parameter is changed, while the others are held constant at their reference value. The range of each parameter and the reference value are documented in Table 3.1. For the range of each

parameter meaningful values are chosen, which allows matching the NBS size with the size of typically used DEAs.

In the first measurement series, the compressed length l is varied in steps of 1 mm. Increasing it causes ΔF to increase, too, while Δs is decreasing at the same time (see Figure 3.9 (a)). For reasons of clarity, only five simulation results are exemplarily shown for each measurement series. The results for the compression rate c, which is varied in steps of 0.05, indicate that it influences ΔF and Δs in a way that the negative stiffness is nearly constant (see Figure 3.9 (b)). When varying the thickness t in steps of 2 µm and the width w in steps of 0.5 mm only ΔF is changing (see Figure 3.9 (c) and (d)). It increases in both cases, while the increase is linear for the width w. This is evident, due to increasing the width w is the same as adding an additional NBS in parallel. In addition to the force-displacement plots, for each parameter set the occurring stress on the beam surface (area of the highest stress) during deformation is documented like exemplarily shown in Figure 3.10.

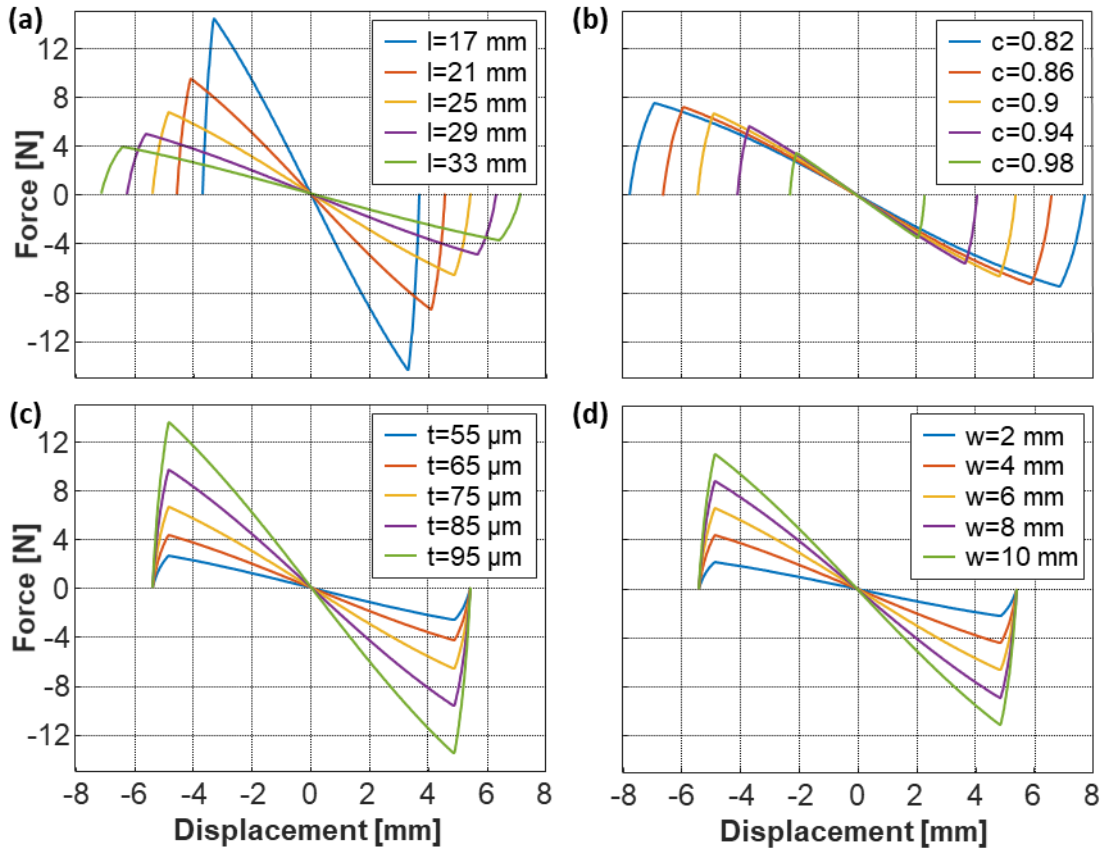

Figure 3.9: Parameter sweep for (a) beam length l, (b) compression rate c, (c) beam thickness t, and (d) beam width w.

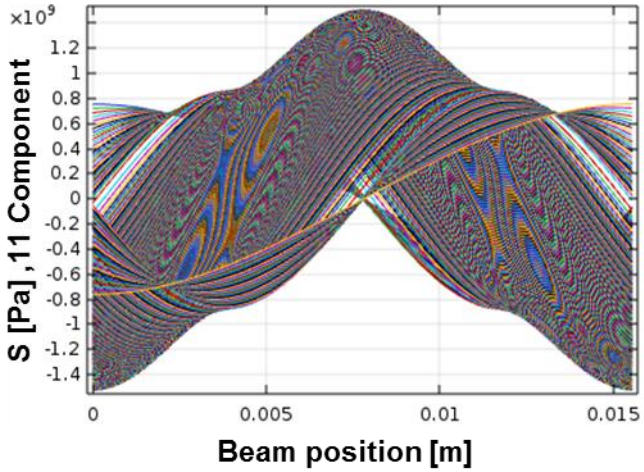

Figure 3.10: Exemplary family of curves for the second Piola-Kirchhoff stress for each displacement step during the simulation. Due to the symmetric nature of the beam only one half of it ($l_0/2 = 0.016\ m$) is considered.

3.2.3 Design method

For the preparation of the design method the whole data collected during the parameter study in Section 3.2.2 is reduced to only three characteristic values for each parameter set (of different c, l, t, and w), namely the maximum occurring stress $\hat{S}$, ΔF,and Δs. $\hat{S}$ corresponds to the maximum magnitude recognized within the family of curves for the second Piola-Kirchhoff stress on the beam surface (see Figure 3.10). Exemplary, the reduced data set for the parameter study of the compressed length l is shown in Figure 3.11 (a). A closer look on the characteristic values of all parameter sets reveals, that Δs is just depending on l and c, $\hat{S}$ is additionally depending on t, while ΔF depends on all four parameters, which is also the reason for the later introduced solving order (see Table 3.1).

The design process itself is actually like solving an under-determined system consisting of four unknowns and three equations. The NBS parameters (c, l, t, and w) represent the unknowns, while the equations are the polynomial fits describing the dependencies of the characteristic values $\hat{S}$, ΔF, and Δs. Besides these values, the installation space is of major importance for a designer. Therefore, the compressed length l can be arbitrarily selected (within the range of the parameter study), too. Additionally, this transfers the equations system to a determined one and it can be solved analytically or graphically. For a better understanding, the solving process is shown in the flowchart in Table 3.1. Within each solving step, one unknown NBS parameter is fixed and resulting temporary characteristic

parameters are calculated. The temporary characteristic parameters of each step are indexed with the NBS parameter fixed in this step. These temporary values are needed to compute the equations of the next solving step.

Table 3.1: Flowchart showing the four calculation steps for all buckled beam NBS parameters (c, l, t, and w). Right column shows the range and reference value of the different NBS parameters used for the parameter study.

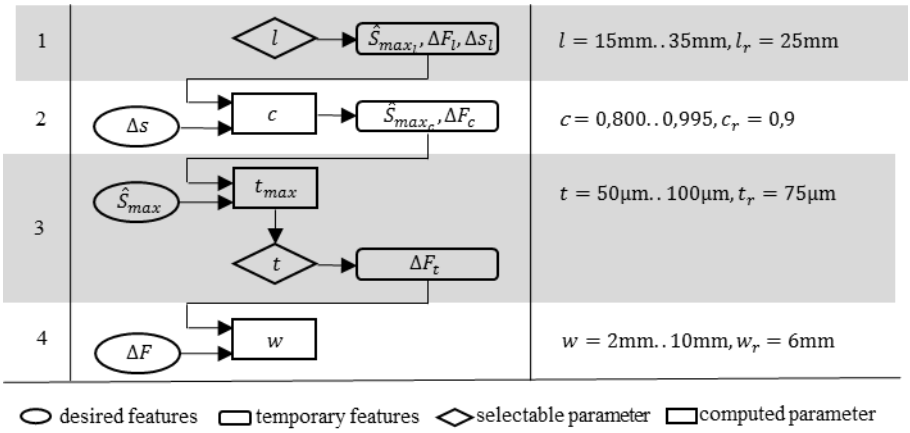

The design process is explained by an example, which uses the more ostensive graphical solution process for the equation system. The whole solving process is illustrated with the plots in Figure 3.11. In this figure the equation of Δs is represented by the polynomial fits of (a) bottom and (b), of $\hat{S}$ by the fits in (a) top, (c) top, and (d), and of ΔF by the fits in (a) center, (c) bottom, (e) and (f). The characteristic values are normalized to be 1 at the reference value (e.g. 0.9 for c) of the corresponding NBS parameter in plot (b) to (f). These normalized values, marked with the index 'N', are used to calculate the temporary values based on the equation displayed at the axis and are dimensionless. In the example, a NBS with the following characteristic values is designed:

- $\hat{S}_{max} = 1.8\ GPa$ (maximum allowed stress),
- $\Delta F = 10\ N$,
- and $\Delta s = 6\ mm$.

In addition, the compressed beam length is chosen to be $l = 28\ mm$. Starting with this value, the temporary characteristic values ($\hat{S}_l = 2.6347\ GPa$, $\Delta F_l = 17.1742\ N$, and $\Delta s_l = 8.5413\ mm$) are gained in the first step, utilizing the plots of the parameter study shown in Figure 3.11 (a). To gain a high accuracy, all values are read out the corresponding MATLAB figures. In the second step, the polynomial fit linking Δs and c is

considered (see Figure 3.11 (b)). However, the chosen compressed beam length l is different to the reference value l_r. To consider this, Δs is normalized by the temporary value Δs_l. Because no further beam parameter has any influence on Δs, $c = 0.9475$ is obtained by exploiting the polynomial fit in Figure 3.11 (b) at the point $\Delta s_N = \Delta s / \Delta s_l = 0.7$. Hence, the beam compression rate is fixed to 0.9475, which is also unequal to the reference value of c, the two remaining temporary characteristic values $\hat{S}_c = \hat{S}_N \hat{S}_l = 1.9983\ GPa$ and $\Delta F_c = \Delta F_N \Delta F_l = 13.6779\ N$ need to be adjusted using Figure 3.11 (c). In step three, the maximum allowed thickness without exceeding the maximum stress $\hat{S}_{max}$ is determined. Therefore, Figure 3.11 (d) is evaluated at the position $\hat{S}_N = \hat{S}_{max} / \hat{S}_c = 0.9012$, which finally solves the equation for $\hat{S}$ and a maximum thickness of $t_{max} = 67.6\ \mu m$ is obtained. Afterwards, the actual thickness t can be selected, depending on the available steel shims. The thickness determines the maximum appearing material stress, which turns out to be $\hat{S} = \hat{S}_N \hat{S}_c = 1.5962\ GPa$ by evaluating Figure 3.11 (d) for a selected thickness of 60 µm. According to Figure 3.11 (e) the remaining temporary value $\Delta F_t = \Delta F_N \Delta F_c = 6.9847\ N$ is obtained, which is used in the last step to determine the width of the beam. Evaluating Figure 3.11 (f) at $\Delta F_N = \Delta F / \Delta F_t = 1.4325$ leads to a width of $w = 8.59\ mm$. If this value is too wide for the installation space, n buckled beams with a width of w/n can be stacked. The final NBS parameters are:

- $l = 28\ mm$,
- $c = 0{,}9475$,
- $t = 60\ \mu m$,
- and $w = 8.59\ mm$.

The maximum appearing stress at the surface of such a NBS is $\hat{S} = 1.596\ GPa$. A comparison with the simulated NBS shows very good agreement (see Figure 3.12). However, the method is not able to predict the regions with positive stiffness of the NBS, which is anyway of minor interest. If the whole NBS force-displacement characteristic is wanted, one simulation with the gained parameters is enough.

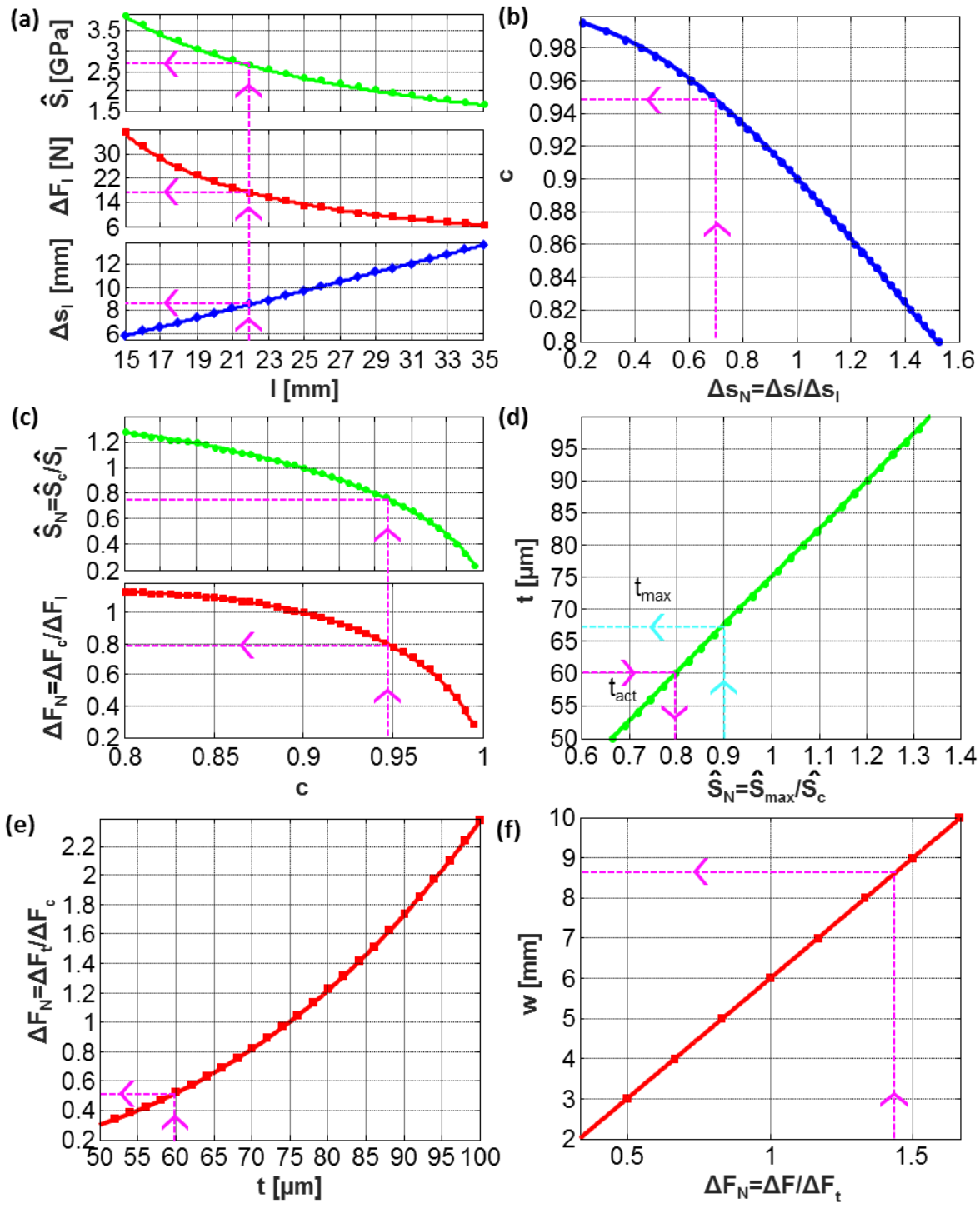

Figure 3.11: Graphical illustration of a stepwise buckled beam geometry determination based on polynomial fits for the characteristic values extracted of the parameter study resulting in the values for a) beam length, b) and c) compression, d) and e) thickness, and f) width.

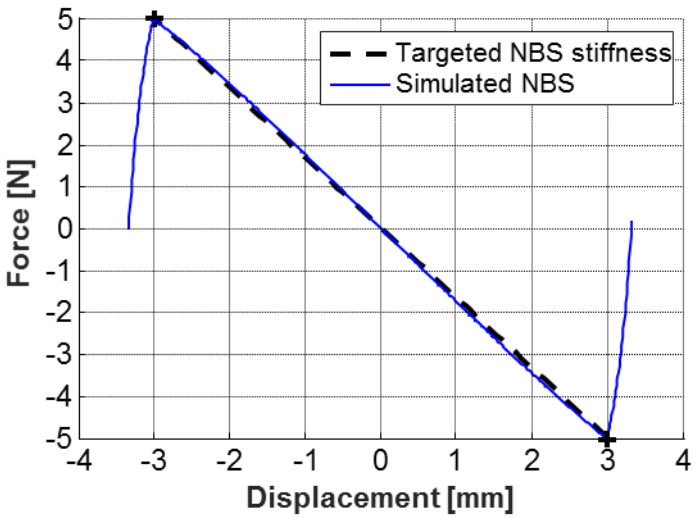

Figure 3.12: Comparison of simulated and targeted force-displacement characteristic. Crosses indicate targeted minimum and maximum force.

3.3 Geometry dependent performance prediction and scaling laws

In the previous chapters, the influence of the biasing elements is studied and it is shown how to design the elements so that they match the characteristic of DEAs. However, the DEA characteristic itself can also be influenced, which is described in this chapter, before combining all in a holistic approach in Section 3.4. This chapter is based on the work of Hau et al. published in the conference papers [103,104] and the journal paper [105]. The demonstrated approaches are shown for COP-DEAs only. However, the presented ideas can also be adapted to SIP-DEAs.

In each of the applications mentioned in Section 1.1, different specifications in terms of stroke and/ or force are typically required. When using conventional actuation technologies, e.g., solenoids or piezo ceramics, a large variety of solutions (see [106,107]) are readily available on the market to cope with many particular applications. In case of DEAs, only few devices are commercially available, therefore custom-built solutions have to be developed for each specific problem. Specifically, in order to develop high-performance DEA systems, the designer has to understand properly how to adapt COP-DEAs to certain force and stroke requirements. Clearly, the actuator performance depends on the material used as dielectric (see equation (2.2) and chapter 2.3) and the chosen

geometry. Since the number of commercially available materials is limited, the geometry is the second parameter (besides the biasing), which can be used to tune the DEA's performance to the needs of specific applications. To this end, this chapter introduces a study on how force and stroke of a COP-DEA scales with geometry. By developing and exploiting geometry scaling laws, an effective way to predict COP-DEA's performance is proposed. It is worth mentioning that approaches for scaling DEA performance have been investigated in earlier literature for diamond shape [60], tubular [108], planar actuators [52,109] or cone actuators [110]. A relevant example is the work of Gupta *et al.* [109], in which the authors propose a DEA output scaling method based on coupling springs with various stiffness to the DEA. A low stiffness of the coupling element results in high stroke and low force, and vice versa. However, this method does not allow individual scaling of force and stroke, and it is limited within the performance range of a specific DEA devices. Another relevant contribution is the work of Orita and Cutkosky [110], in which FE simulations are used to determine the influence of the geometry onto the overall stiffness of a cone DEA. In contrast to the mentioned approaches, the method proposed in this work, exploits the DEA geometry to scale force and stroke output individually in a much larger range without the use of complex and time-consuming FE simulations.

The method presented in this chapter focuses on COP-DEAs. Six different COP-DEAs designs with different inner (ID) and outer diameter (OD) are manufactured (see Figure 3.13 and Table 3.2), and their force-displacement characteristics is measured under different electrical loads. These DEAs are used to study the influence of the geometry on force and stroke output, as well as the validation of a model-based prediction method. In particular, the performance prediction is based on extracting average stress-strain data from experimental force-displacement data (training data set), for a given geometry and material combination (elastomer and electrode). These material data can then be used for calculating force-displacement curves of DEAs with various sizes, based on equations that transform strain and stress to displacement and force, respectively. The method based on force equilibriums described in Section 3.1 can then be used to determine force and stroke output when working against a desired load. Finally, the experimental data and the model-based predictions are compared. The experimental data is additionally used to extract scaling laws for COP-DEAs.

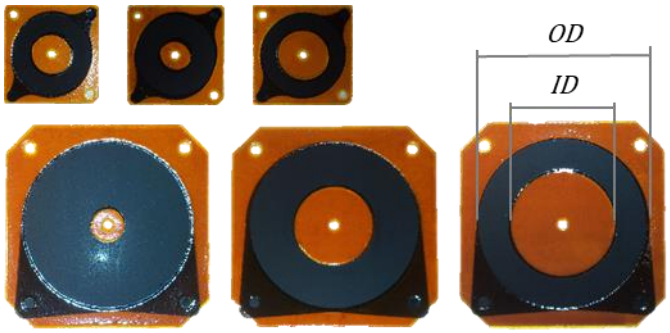

Figure 3.13: Six DEA geometries manufactured for testing and evaluation. Three D25 DEAs (upper row) and three D50 DEAs (lower row) with different IDs (small, medium large), respectively, are shown. The number after the 'D' indicates the overall dimensions, for instance D25 names a DEA with 25 mm edge length.

Table 3.2: Overview of the geometries of the different test specimens. Six different geometries are tested.

	ID [mm]	OD [mm]
D25 DEA small	8.6	21.0
D25 DEA medium	11.4	21.0
D25 DEA large	13.5	21.0
D50 DEA small	8.6	41.9
D50 DEA medium	20.1	41.9
D50 DEA large	26.8	41.9

3.3.1 Performance prediction and evaluation

The presented method for the performance prediction of COP-DEAs with arbitrary geometries is based on the assumption that the stress-strain characteristics of a given material set (electrode and elastomer) is a geometry independent material property. Our first goal, then, is to find some equations that allow relating force and displacement measurements to a stress-strain description.

Strain computation

For the strain calculation, we start by approximating the deflected COP-DEA with a truncated cone [62,111], knowing the actual shape of the membrane is more parabola like than a straight line [112,113]. A comparison of the truncated cone (solid line) and the actual membrane shape (dashed line) is shown in Figure 3.14 (a).

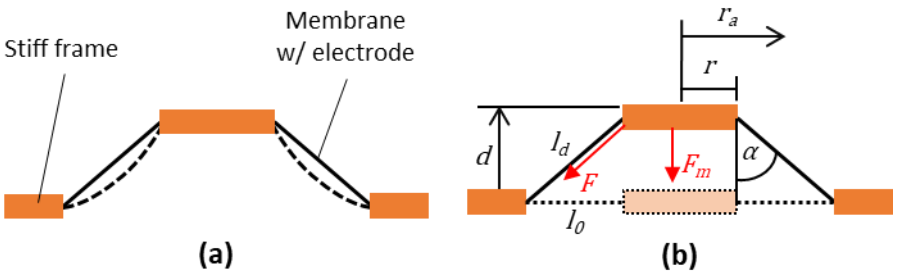

Figure 3.14: (a) Cross-section through the deflected DEAs shown in Figure 3.13. The sketch shows the truncated-cone approximation (straight lines) in comparison to an exaggerated actual membrane shape (dashed lines). (b) Sketch with nomenclature for calculations.

With this approximation, the average stretch $\bar{\lambda}$ can be defined as the quotient of l_d and l_0, representing the electrode-ring width in the deformed and the undeformed state, respectively (see Figure 3.14 (b)), as follows

$$\bar{\lambda} = \frac{l_d}{l_0}. \tag{3.7}$$

By applying the *Pythagorean* Theorem, l_d can be expressed as a function of l_0 and the out-of-plane displacement d resulting in

$$\bar{\lambda} = \frac{\sqrt{d^2 + {l_0}^2}}{l_0}. \tag{3.8}$$

This equation expresses an average stretch $\bar{\lambda}$, which is only depended on the COP-DEA's geometry and its displacement, while neglecting the applied pre-stretch during manufacturing. Thus, it defines an actuation stretch, rather than an overall stretch [111]. Finally, the material average strain $\bar{\varepsilon}$ can be computed as

$$\bar{\varepsilon} = \bar{\lambda} - 1 = \frac{\sqrt{d^2 + {l_0}^2}}{l_0} - 1. \tag{3.9}$$

Stress computation

Stress is, by definition, the ratio between a force and an area upon which the force is acting (assuming that the direction of the force is orthogonal to the area). For membrane DEAs, the product of the membrane thickness and a circumference within the electrode-ring defines this area. In addition, while deflecting the DEA the membrane gets stretched, resulting in a decrease in thickness [104]. To calculate the thickness during deflection t_d

we assume the elastomer to be incompressible, and thus its volume Vol remains constant during stretching [114]. This leads to the following equation

$$Vol = const. = A_{el,0} t_0 = A_{el,d} t_d, \tag{3.10}$$

with the area of the electrode-ring $A_{el,0}$ (undeflected), and of the cone shell $A_{el,d}$ as well as the starting thickness t_0, and the deflected thickness t_d. By recalling the equation for the surface area of a truncated cone [114], equation (3.10) can be simplified as follows

$$t_d = \frac{l_0 t_0}{l_d} = \frac{l_0 t_0}{\sqrt{d^2 + {l_0}^2}}. \tag{3.11}$$

Then, the cross sectional area A on which the force F is acting on can be given as follows

$$A = 2\pi r_a t_d = 2\pi r_a \frac{l_0 t_0}{\sqrt{d^2 + {l_0}^2}}, \qquad r_a \in [r, r + l_0] \tag{3.12}$$

where r_a is the radius where the area A is calculated. Values for r_a can range from the inner disc radius r to the radius of the outer frame $(r + l_0)$ resulting in a different value of stress for the same force F.

The out-of-plane force F_m measured with the experiments described in Section 2.5 needs to be converted to the force F acting in the direction of the stretched membrane using kinematic relationships (see Figure 3.14 (b)), as follows

$$F = \frac{F_m}{\cos \alpha} = \frac{F_m \sqrt{d^2 + {l_0}^2}}{d}. \tag{3.13}$$

Finally, the stress σ within the elastomer membrane can be calculated by combining equations (3.12) and (3.13) to

$$\sigma = \frac{F_m \left(d^2 + {l_0}^2\right)}{2\pi r_a l_0 t_0 d}, \qquad r_a \in [r, r + l_0]. \tag{3.14}$$

The stress calculated with equation (3.14) only depends on the COP-DEA's geometry, its displacement, and the force needed to displace it. However, this stress is not uniquely defined, since it actually represents the particular stress within the membrane at the particular radius r_a. Note, that this is not the case for the average strain in equation (3.9), which is uniquely given for the specific geometry. According to equation (3.14), the stress within the membrane decreases from the inner disc to the outer frame. FE simulations reported in [115] show the same trend, in addition to some local effects, which are not accounted by lumped model developed above. The stress distribution also causes the

thickness of the membrane to increase from the inner to the outer disc and therefore the electric field to decrease, which is visually shown by experiments in [116].

To extract a material characterization in terms of stress-strain response, we need to choose a fixed value for r_a to calculate the average stress at a specific membrane circumference. One possible solution, initially proposed in [114], is to use the smallest radius ($r_a = r$), corresponding to the point at which the highest stress occurs. This idea accounts for the highest stress appearing in the material, and therefore it describes most critical conditions, which is important, for instance in fatigue and failure analysis. However, for an averaged stress calculation, such a maximum stress does not represent a suitable quantity. In this paper, we pursue a different approach based on considering the stress at the average radius ($r_a = \frac{2r+l_0}{2}$). With this assumption, the averaged stress is defined as

$$\bar{\sigma} = \frac{F_m(d^2 + {l_0}^2)}{\pi(2r + l_0)l_0 t_0 d}. \tag{3.15}$$

Describing the stress by means of an average radius also has an interesting physical interpretation. In fact, the radial stress at the average radius of the COP-DEA turns out to be equivalent to the longitudinal stress of an equivalent pure-shear rectangular membrane, having a length equal to l_0 and width equal to the average circumference c_{ave} calculated in correspondence to the average radius (see Figure 3.15). Note that both geometry have the same resulting active area.

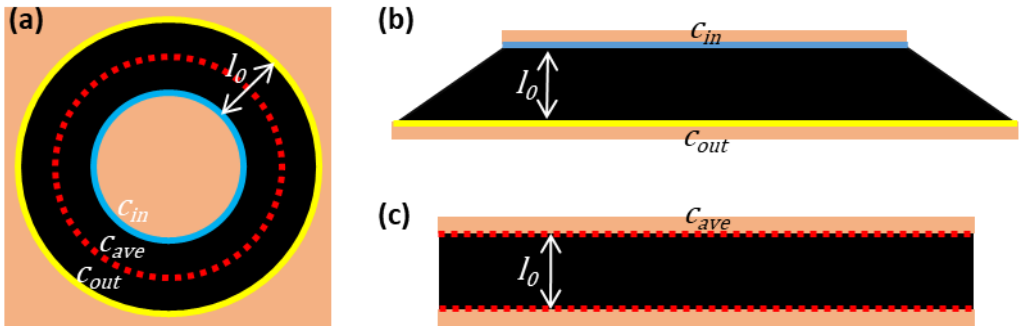

Figure 3.15: Transformation of (a) the COP-DEA design to (c) an equivalent pure shear strip DEA design with a width equal to the average circumference c_{ave}. (b) The intermediate step where the COP-DEA is just unwound into a strip DEA configuration.

Validation of modeling method

To validate equations (3.9) and (3.15) the CV experiments described in Section 2.5 are performed for the six different DEAs of Table 3.2. We point out that the force-displacement

characteristics may be different for each individual sample, given the same geometry, due to manufacturing tolerance and experimental inhomogeneity. To reduce the effects of these phenomena, at least six DEAs are tested for each geometry. A least square fit is used to eliminate the residual viscoelastic hysteresis and to get an averaged force-displacement characteristic for each geometry (see Figure 3.16 (a)). The calculated stress-strain curves for all geometries mentioned in Table 3.2 are plotted in Figure 3.16 (b) measured at constant voltage values of 0 V and 2500 V and at a frequency of 1 Hz, respectively. A significant overlap is observed between data for all geometries, proving the validity of the assumptions discussed above. However, the resulting stress for the D50 DEA small (Figure 3.16 (b), dashed lines) is lower than the ones obtained for the other cases. The reason for this deviation are the simplifications made. Especially the truncated cone assumption error increases, due to the relatively large l_0. Nevertheless, this result proves that the equations above can be used to calculate a generalized and geometry-independent stress-strain behavior, for a certain material set.

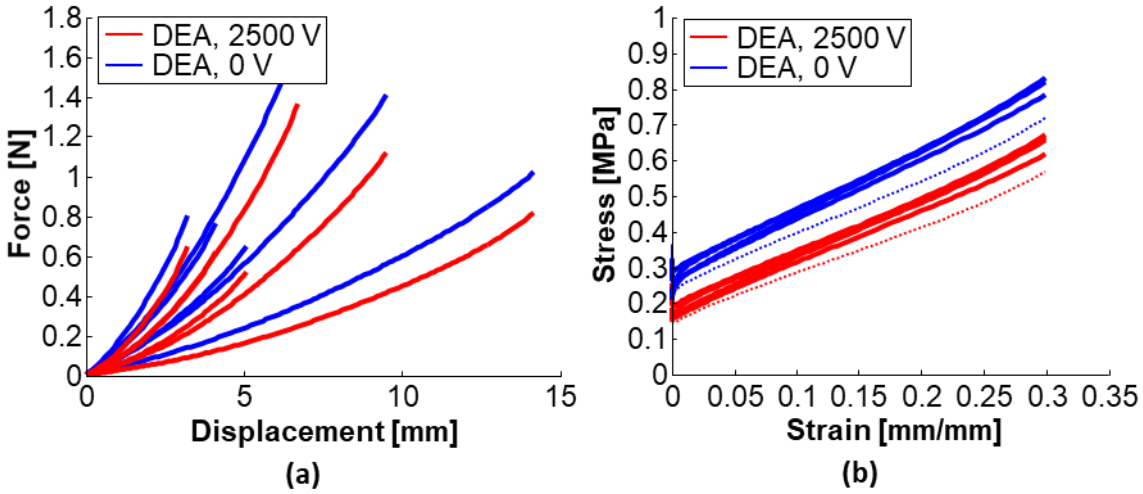

Figure 3.16: (a) Averaged (number of test specimens per geometry n=6) force-displacement data for six different geometries at 0 V and 2500 V and (b) out of it calculated stress-strain plots. The dashed lines in (b) represent the results of the D50 DEA small, which deviates due to its high deviation from the truncated cone assumption.

The results above suggest the possibility of predicting force-displacement data for various COP-DEA sizes. To do so, a given material set (elastomer and electrode) needs to be characterized to gain a set of training data for the stress-strain profile, for instance the one obtained for D25 DEA medium (Figure 3.17, (a)). Equations (3.9) and (3.15) can then

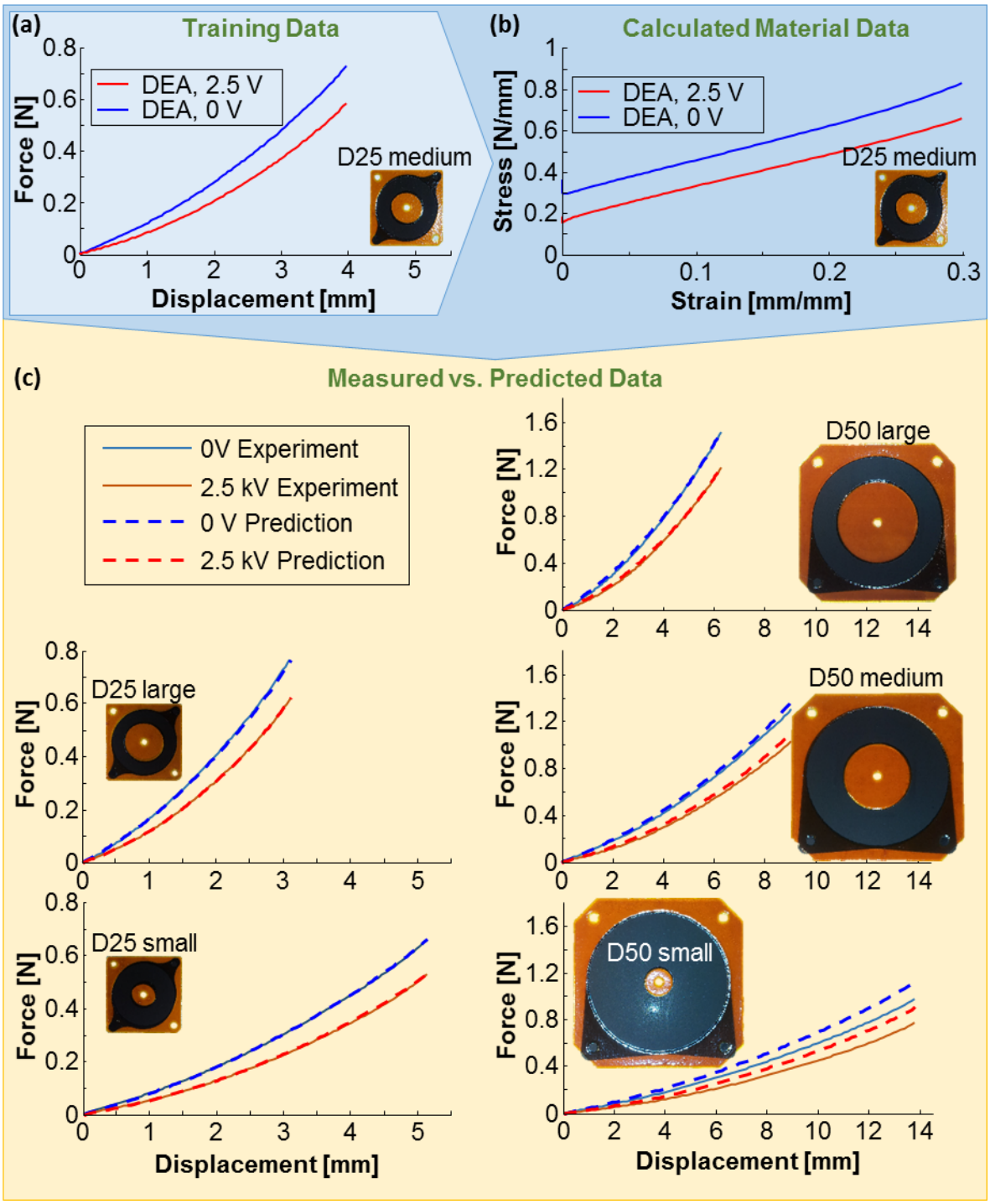

Figure 3.17: (a) Training data set of a D25 DEA medium used to calculate (b) geometry independent material data using equation (3.9) and (3.15), as well as, (c) measured vs. predicted data (using material model) for 5 different DEA sizes. Photograph of DEAs are scaled down to half of their real size.

be used to compute a stress-strain characteristic for the given material set (Figure 3.17, (b)). Finally, the same equations can be used to calculate force-displacement data for any other COP-DEA geometry. Figure 3.17 (c) shows that the result of such a prediction (based

on D25 DEA medium training data) satisfactorily agrees with the measurement data for the other five DEA sizes studied. The predicted force-displacement curves can then be used to test whether the COP-DEA of the chosen geometry can match the requirements (e.g. blocking force or/ and stroke) of a certain application.

To quantify the error of the proposed prediction method for the force-displacement characteristic of a DEA, two different scenarios are studied and evaluated with the model introduced in the previous Section 3.1. In the first case, the blocking force at a strain of 0.25 is measured and compared with the predicted values. In the force-displacement diagram, the blocking force is equivalent to a spring with infinite stiffness, that is, a vertical line. The results are shown in Table 3.3. As one could already expect from Figure 3.16 (b), the largest error (7.8%) is calculated for the D50 DEA small. All other DEAs show an error of 3.1% or less.

Table 3.3: Comparison of measured and predicted blocking force at a strain of 0.25.

	Measured [N]	**Predicted [N]**	**Error [%]**
D25 DEA small	0.117	0.115	1.5
D25 DEA medium	0.126	0.126	0.0
D25 DEA large	0.138	0.135	2.3
D50 DEA small	0.183	0.197	7.8
D50 DEA medium	0.249	0.242	3.0
D50 DEA large	0.276	0.268	3.1

Table 3.4: Comparison of measured and predicted stroke for a hanging mass of 40 g.

	Measured [mm]	**Predicted [mm]**	**Error [%]**
D25 DEA small	0.711	0.678	4.6
D25 DEA medium	0.519	0.519	0.0
D25 DEA large	0.412	0.402	2.5
D50 DEA small	1.800	1.579	12.3
D50 DEA medium	1.048	0.961	8.3
D50 DEA large	0.657	0.643	2.2

In the second scenario, the stroke of the DEAs is estimated when the membrane is biased with a constant load of 40 g, corresponding to a virtual spring with zero stiffness (horizontal line) in the force-displacement diagram. In this case, the largest error (12.3%) is

observed for the D50 DEA small, too. All other DEAs show an error smaller than 8.3% (see Table 3.4).

3.3.2 Experimental results and scaling laws

This chapter studies how the geometry of a DEA influences its force and stroke output. The setup described in Section 2.5 allows running blocking force measurements at different constant strains, too. Therefore, experiments are carried out by displacing the center disc of the DEA to a fixed value, and then cycling the voltage between 0 V and 2500 V, while measuring the force. To ensure strains of 0.1, 0.2, and 0.3, the corresponding displacement d is calculated for each geometry using equation (3.9). As an example, the results of such a measurement are shown in Figure 3.18 for a single D50 DEA large. The difference between maximum and minimum force of each voltage cycle reflects the blocking force. The data shows that the blocking force as well as the viscoelastic creep of the material increases with the applied strain.

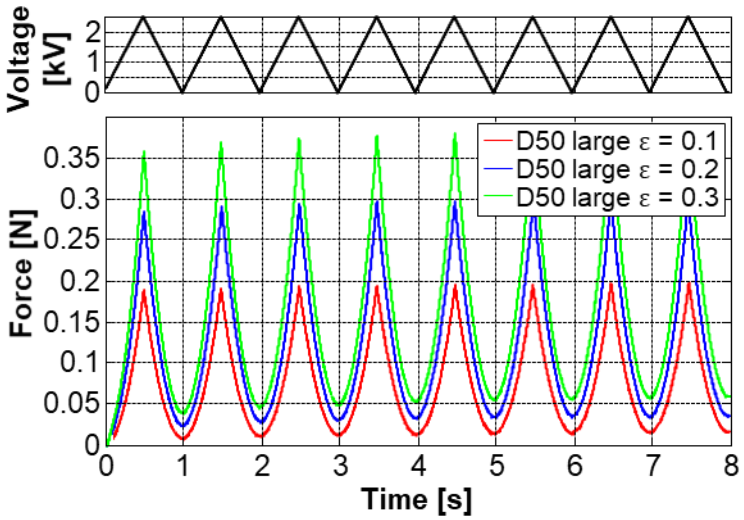

Figure 3.18: Results of blocking force measurements for a single DEA (D50 large size) at different strain levels for triangular input voltage.

To find a correlation between geometry and blocking force, the force data for all geometries and strains is plotted over the ratio between ID and OD in Figure 3.19. The figure shows an increasing linear trend for the blocking force vs. ID OD^{-1}. The force value is also larger for higher strain levels. Note also that, for the data corresponding to highest

ratio ID/OD, the D50 DEA shows the double of the blocking force observed in the D25 DEA case. All these results indicate a strong relationship between DEA size and blocking force.

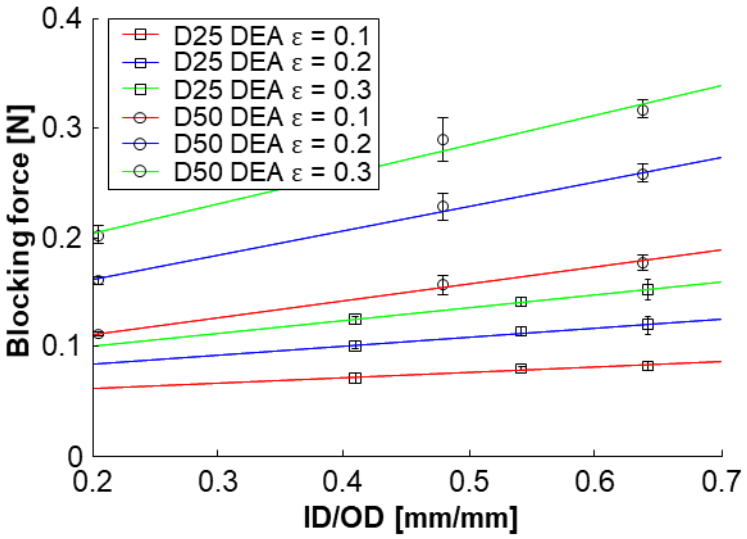

Figure 3.19: Results of blocking force measurements for all DEAs of Table 3.2 at three different strain levels. Plotted quantities represent mean values (n=8) with error bars and linear regression line. The three data points for each data set represent the different inner disc diameters: small, medium large (left to right).

According to the analysis carried out in previous Section 3.3.1, the scaling factor between force and stress is proportional to the area on which the force is acting. This area is defined by the average circumference c_{ave} and the actual membrane thickness. Since the thickness of the membrane solely depends on the strain and its initial thickness (see (3.9) and (3.11)), all DEAs stretched to a certain strain exhibit the same thickness. Therefore, the resulting area on which the force is acting on only differs because of the average circumference c_{ave} that, in turn, is the main factor that influences the blocking force. Figure 3.20 shows a boxplot containing the data of all six geometries, grouped by the strain level and the overall DEA size. The blocking force is normalized with respect to the average circumference c_{ave} and is plotted on the y-axis. As indicated by the notches in the boxplot, there is no significant difference between the samples of D25 and D50 DEAs (for a given strain level). This result validates the assumption that the average circumference c_{ave} determines the blocking force of a COP-DEA. This result agrees with the scaling behavior of planar actuators proposed in [52], when assuming the average circumference to be the width of an equivalent pure shear sample (compare Figure 3.15).

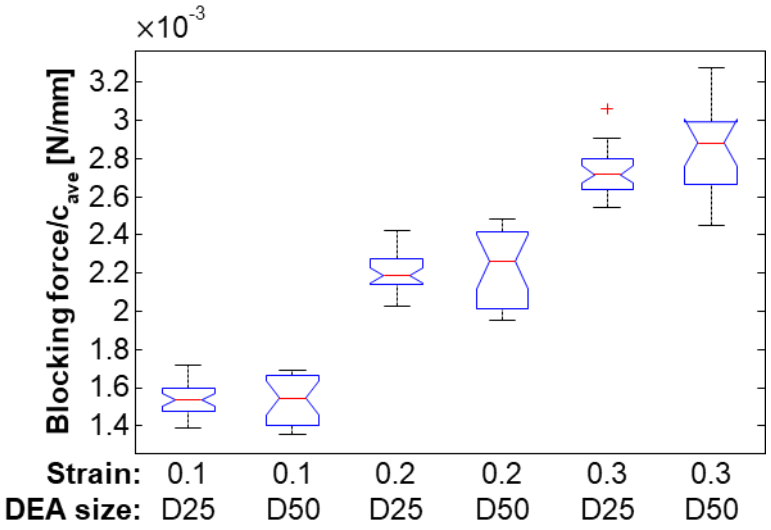

Figure 3.20: Boxplot showing the blocking force normalized on the average circumference c_{ave} grouped by the two different DEA sizes at three different strain levels. Sample size for each box n=18.

Similar correlations are observed when studying the stroke output of the DEAs. The stroke output of a DEA, in a pure shear configuration, mainly depends on the length of the DEA, that is, the electrode-ring width l_0. In a first step, a constant load is applied for each DEA geometry, which displaces the specific DEA to a certain strain level at zero volts. Afterwards, the method described in Section 3.1 is used to estimate the stroke when a voltage of 2500 V is applied. When plotting this stroke over l_0, one observes again a linear relationship, which is slightly strain dependent (Figure 3.21). Therefore, l_0 has the major impact on the stroke of a COP-DEA.

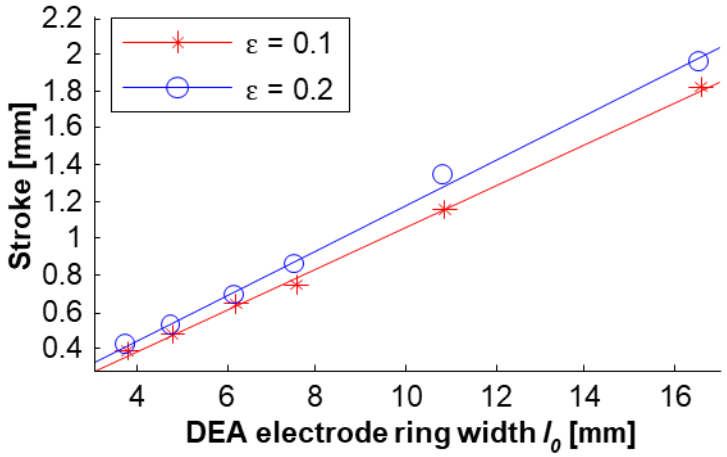

Figure 3.21: Estimated stroke at two different strain levels for all six different DEAs over electrode-ring width l_0. Marker indicate mean values (n=6). Error bars are neglected because they are smaller than the marker.

These results can be translated into laws describing how stroke and force scale with geometry. If the outer diameter stays constant, the force increases with increasing inner diameter, while the stroke decreases (Figure 3.22 (a)). Stroke and force increase with increasing outer diameter, if the inner diameter stays constant (Figure 3.22 (b)). The stroke stays constant and the force increases, if the outer and the inner diameter increases, while l_0 stays constant (Figure 3.22 (c)).

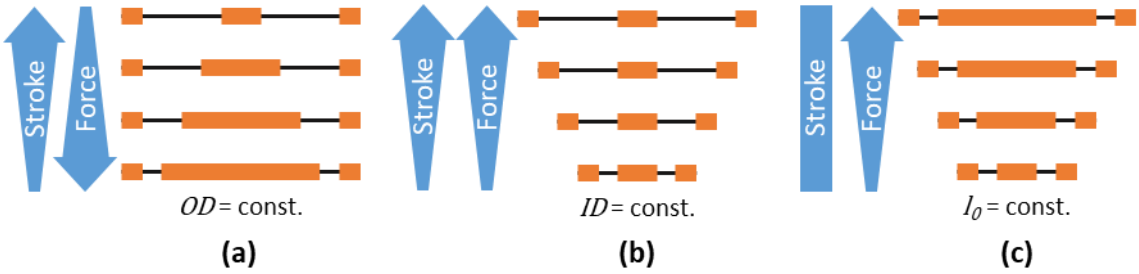

Figure 3.22: Scaling laws for stroke and force output of COP-DEAs: (a) for constant outer diameter, (b) constant inner diameter and (c) constant electrode-ring width.

3.4 Application-driven actuator system design

The previous sections 3.1 and 3.3.2 presented the influence of the biasing mechanism and the DEA geometry, respectively, on the actuator system performance. However, there are two additional ways to influence the force output of a DEA. The first one can just be used to increase the force difference of a DEA system by increasing the Young's modulus of the elastomer used. Figure 3.23 (a) shows the linear approximated forces of two exact same DEAs but the Young's modulus of material 2 is twice as high. The Maxwell pressure is independent of the Young's modulus, and thus the gap between the HV and LV curves stays constant. By adjusting the NBS to both materials the same stroke can be achieved but the force difference is about to be doubled. This method is just mentioned for the sake of completeness, because it is still just a theoretical option, due to the absence of commercially available silicone films with different Young's moduli, and it just increases the force difference and not the force output of the DEAs. The second and more useful way is to stack DEAs [62,117]. This allows increasing the work area as well as the force difference linearly with the number of layers. This is again experimentally proven with three stacks of three, six, and nine D75s DEA modules (described in Section 4.2.1) and the results are shown in Figure 3.23 (b). One can easily see the linear increase.

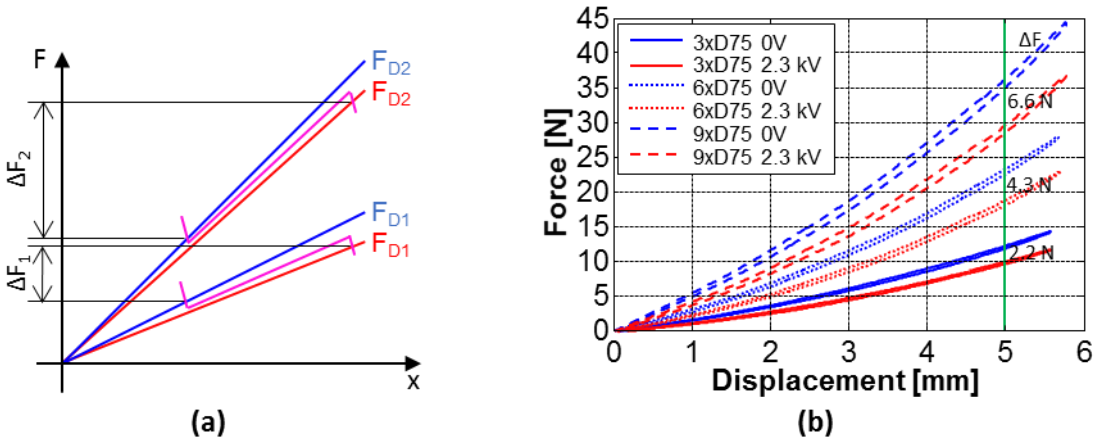

Figure 3.23: (a) Scaling of the force difference by choosing materials with different Young's moduli and adapting the NBS. Material 2 is chosen to be stiffer than Material 1 and the Maxwell pressure is assumed constant. (b) Increasing the work area as well as the force difference by stacking multiple DEAs. The blocking force ΔF is measured at 5 mm displacement.

The above presented (see Section 3.3.2) scaling laws allow for the introduction of a design routine to adapt DEA systems for specific applications. This approach allows one to design actuator systems for arbitrary loads, in contrast to a similar approach of Berselli et al. [62], which is just for the design of constant force actuators. The presented design routine focuses on but is not limited to actuator systems consisting of a DEA (SIP or COP) and a biasing with negative spring-rate, i.e. a NBS coupled with a linear spring. It allows defining the DEA and NBS geometry as well as the characteristic of the linear spring. In addition, the mechanical design parameters, such as offsets and spacers between the elements as well as the pre-compression of the linear spring can be calculated using the modeling approach introduced in 3.1. In general, the design process consists of the following steps (see also Figure 3.24):

1. Characterize load in terms of force and stroke.
2. Choose DEA type: Typically, SIP for high-stroke and COP for high-force applications.
3. Define DEA geometry: Maximize outer diameter (COP)/ width (SIP) in accordance with the constrictions of the applications. Choose inner diameter (COP)/ length (SIP) based on material parameters, such as maximum allowed strain and breakdown voltage, to match stroke requirements.

This step determines the maximum stroke and force output of a single DEA element.

4. Calculate needed number of DEAs to match the force requirements.
5. Define the force-displacement characteristic of the biasing mechanism to match the DEA stack with the load and the desired stroke.

   This determines the geometry of the NBS and the stiffness of the linear spring as well as its pre-compression.
6. Calculate all offsets and spacers of the single elements.

The whole process could be iterative and the steps three to six might be repeated to find the best solution.

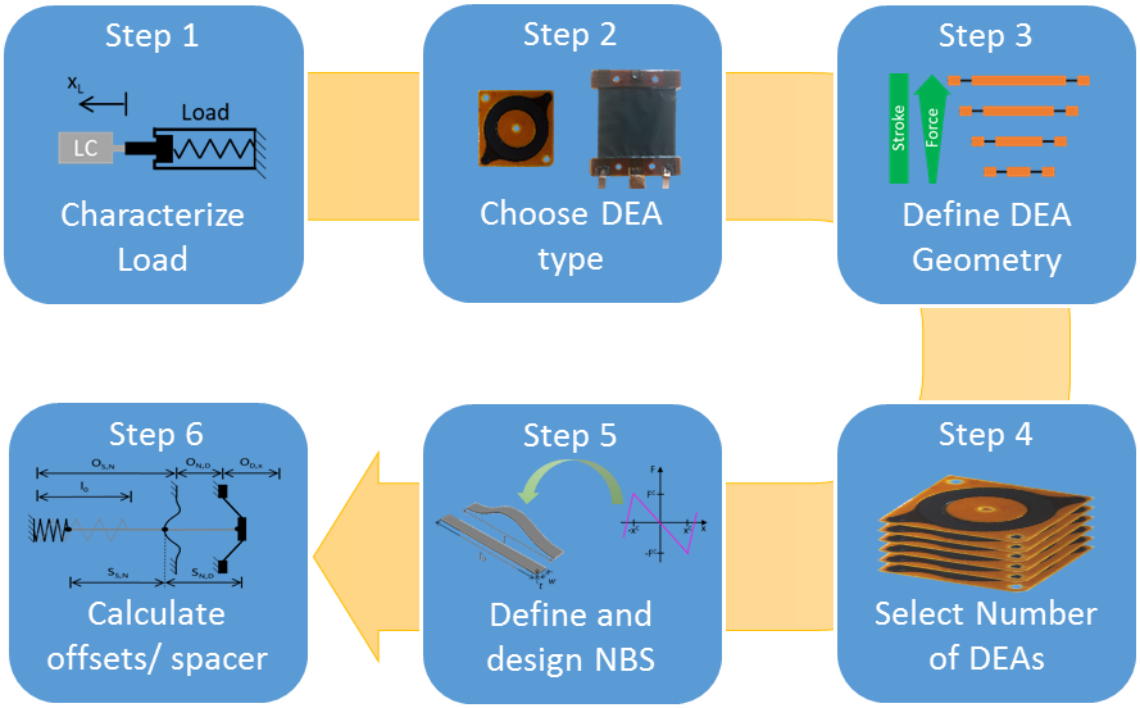

Figure 3.24: Design process of a DEA system to match a specific load.

Now the whole process will be explained using the example shown in Figure 3.25 (a). The same actuator system, which is introduced in the example in Section 3.1 (see Figure 3.3), is used and coupled with a load. The exemplary load consists of a push rod, which is loaded with a pre-compressed linear spring. The characterization of the load (step 1) is sketched in Figure 3.25 (b) and the gained force-displacement characteristic including the desired stroke Δs is shown in Figure 3.25 (c). This information allows defining the kinematic relationship for the load as follows:

$$x_L = -x. \tag{3.16}$$

This equation, together with the equations (3.1) to (3.3), completes the kinematic relations for the whole system (shown in Figure 3.25 (a)), which later allows to calculate all offsets and spacers. To solve the actuation problem, the force equilibrium needs to be considered, in addition, which is given by the following equation:

$$F_D - F_L = -F_S - F_N. \tag{3.17}$$

The forces are sorted that the DEA and load force are on the left and the biasing forces are on the right side of the equation. This sorting helps in the following design process to determine the number of DEA layers and the biasing characteristic.

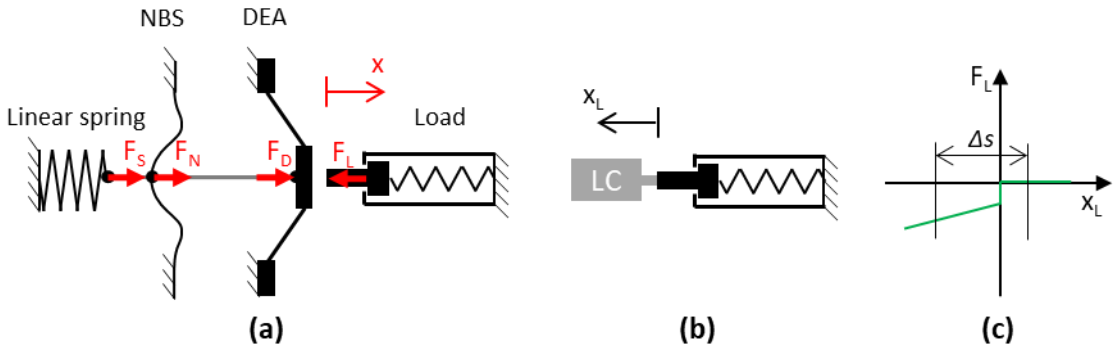

Figure 3.25: (a) Sketch of the DEA system and a load. The sketch also contains the FBD and the global coordinate system. (b) Sketch of the measurement setup for characterizing the load and (c) the corresponding force-displacement characteristic with the desired stroke Δs.

In the example, the COP-DEA design is chosen (Step 2). Besides the force and stroke requirements, the decision for the DEA type can also be influenced by the installation space requirements of the application.

With the information of the desired stroke, the method explained in Section 3.3 can be used to determine the DEA geometry (step 3). As mentioned, the maximum stroke is dictated by the ring width l_0 and the material depended maximum allowed stretch λ_{max}. The breakdown field needs to be considered, too, due to the thinning of the elastomer during stretching. The electrode-ring width l_0 needs to be chosen to fulfill the following inequality, which is derived from equation (3.8):

$$\lambda_{max} \geq \frac{\sqrt{d^2 + {l_0}^2}}{l_0}. \tag{3.18}$$

The displacement d in this case is considered as the sum of the desired stroke Δs and a minimum displacement of the DEA. This minimum displacement is needed separate the LV and HV force curves of the DEA and is described by $x_{LV} - O_{D,x}$ in Figure 3.26 (b), which shows the graphical solution of equation (3.17). Now the geometry of the DEA can be defined. The outer diameter of DEA is limited by the space requirements of the application and should be chosen as large as possible, while the inner diameter needs to be smaller by a factor of $2 \cdot l_0$. The geometry also determines the work area of a single DEA, which can be calculated with a set of training data using the approach described in Section 3.3.1.

In the next step (step 4), the needed number of DEAs, which need to be stacked, is determined. For this purpose, the graphical solution in Figure 3.26 (b) is examined. This figure shows the sum of load and DEA forces (at LV and HV; individual forces shown in Figure 3.26 (a)) acting against the biasing mechanism. This plot is important for the system designer. At least so many DEAs need to be stacked that the curves at LV and HV are completely separated. Additionally, an arbitrary mirrored-N-shaped biasing curve needs to fit within the work area and it needs to intersect the LV curve at a desired x-value x_{LV} and the HV curve at x_{HV} (see Figure 3.26 (b)). This defines the biasing mechanism (step 5). The resulting stroke of such a system equals $x_{HV} - x_{LV}$, which should be equal to Δs.

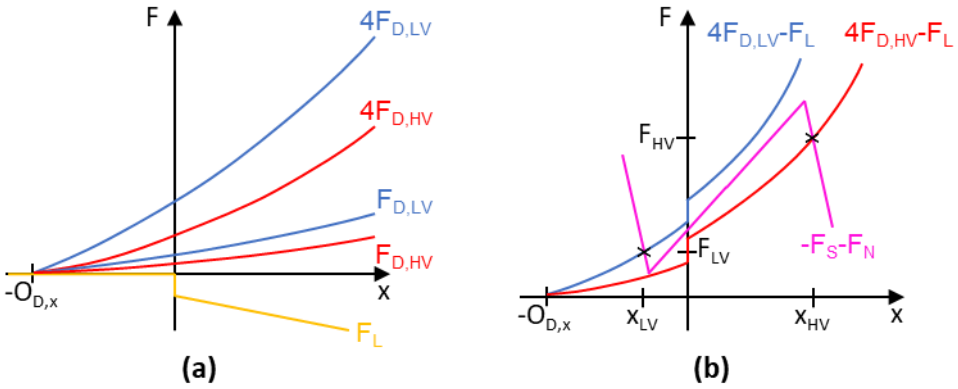

Figure 3.26: (a) Individual forces of the load, a single DEA at HV and LV and a stack of four DEAs. (b) Graphical solution for equation (3.17) of the actuator system shown in Figure 3.25, which is useful for designers of actuator systems.

Then the arbitrary biasing curve is used to gain the important parameters for designing the biasing mechanism. The first parameter is the pre-compression force of the spring ΔF_S, which is the offset of the origin of the arbitrary biasing curve (see Figure 3.27 (a)). Then the stiffness of the biasing mechanism between the minimum and the maximum is used to

determine the stiffness of the NBS k_N in this region and of the spring k_S with the following equation:

$$-\frac{\Delta F_{SN}}{\Delta x_{SN}} = k_S + k_N. \tag{3.19}$$

Note that k_N is negative and its absolute value needs to be larger than k_S, which is positive. This actually allows choosing any value for the spring and the NBS stiffness as long as the absolute value of the sum equals the stiffness of the biasing mechanism shown in Figure 3.26 (b) and Figure 3.27 (a). However, meaningful values for the spring stiffness should be selected, which means that a spring fulfilling the requirements is commercially available. Besides the stiffness, which should be chosen as low as possible, it is important that the spring could be compressed enough to generate the needed force ΔF_S and is still able to be further compressed by $\Delta x_{SN}/2$. With the NBS stiffness k_N and the distance between the minimum and the maximum force of the biasing mechanism Δx_{SN}, the NBS is fully defined. Based on the design process introduced in 3.2 all relevant parameters of the NBS, such as length, width, thickness, and compression can be calculated. Finally, the offsets and spacers of the whole system can be calculated using the equations (3.1) to (3.3) (step 6).

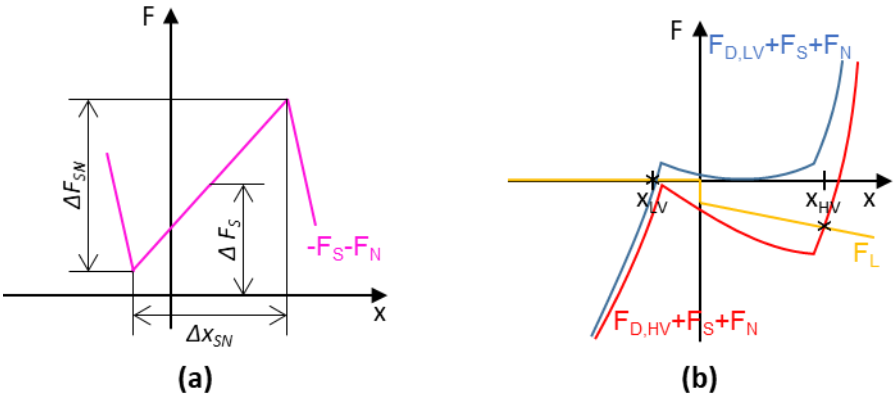

Figure 3.27: (a) Arbitrary biasing force and (b) the graphical solution for equation (3.20) of the actuator system shown in Figure 3.25, which is interesting for the customer of actuator systems.

Besides the force equilibrium shown in Figure 3.26 (b), which is used for the design process, there is an additional interesting one. This equilibrium can be written as:

$$F_L = F_D + F_S + F_N \tag{3.20}$$

This one combines all actuator forces and equates them with the load. The result is shown in Figure 3.27 (b). It shows the work area of the whole actuator system, and thus it is more

interesting from a customer point of view. The actuator system is able to drive all loads, which fit into the work area of the actuator system.

3.5 Conclusion

Chapter 3 studies the main factors that influence the force and stroke output of a DEA system, namely the biasing elements and its geometry. Due to the biasing elements are already intensely studied by other scientists, their influence is just summarized and the focus is on the design of buckled beam based NBSs. The design process is based on a parameter study, which needs to be performed only once. Afterwards, the buckled beam design parameters for a NBS with a desired force-displacement profile can be analytically calculated. The deviations in the force profile in comparison to time-consuming FE simulations are negligibly low, which has not been achieved by any other analytical method published, yet.

For the DEAs the focus is on the geometry. Therefore, a systematic approach to predict the force-displacement characteristic of COP-DEAs with arbitrary geometries is proposed. The method is based on extracting a material characteristic (in terms of a stress-strain behavior) from a set of training data, which is then used to calculate the force-displacement characteristic for different COP-DEA geometries. The method is validated in two different prediction scenarios: blocking force and stroke of various geometries. The prediction errors for stroke and blocking force are not larger than 8.3% and 3.1%, respectively. Additionally, measured and predicted force-displacement plots are compared and show good agreement. Since this method relies on simplified assumptions for the state of deformation of the membrane, that is, the membrane deforms as a truncated cone, the error increases as the deformation becomes less ideal, namely in case of larger electrode-ring widths. Nevertheless, this method is much faster than FE simulations and the errors are still in an acceptable range.

In addition, this study has shown that the stroke output of COP-DEAs mainly depends on the electrode-ring width and that it increases linearly with it, while the force scales linearly with the average electrode-ring circumference. These two parameters can be used to scale stroke and force output of COP-DEAs individually. This method can also be transferred to other DEA geometries, for instance SIP-DEAs.

Finally, a systematic and application-driven design process for DEA systems is developed. It is based on a graphical method to model the performance of DEAs in combination with mechanical elements, which is related to the basic methods used by other scientists, such as [34,40,93,94]. However, for the first time a holistic approach, which includes also the design of the individual elements, is demonstrated in this work. The graphical method, in combination with the findings about the scaling laws of DEAs and the NBS design process, can be used as a powerful design tool for DEA actuator systems. As a result, all relevant information, such as DEA, NBS and spacer sizes as well as offsets, to build an actuator system can be calculated. Designers can use the proposed design process to adapt DEAs to certain applications without using complicated and time-consuming FE simulations as well as low testing and prototyping effort.

Future work can focus on the integration of inertial and acceleration forces into the design process to allow also a dynamic analysis of the system.

Chapter 4 High-force actuator systems

This chapter demonstrates the abilities of the design process, which is introduced in the previous Section 3.4, by designing a DEA system with outstanding performance. For the first time, the force output of membrane DEAs is increased approximately by a factor of 200 to the 100 N level, while maintaining a compact overall size, due to an innovative biasing concept. The chapter includes results of and is based on the conference papers [118,119] as well as the journal article [120].

Pushing the force limit of DEAs is important to make them useful for several applications like valves or brakes, to name just two. Therefore, it is interesting to research high-force DEAs. This chapter starts with an overview of different state-of-the-art DEA concepts with high-force output (Section 4.1) to classify the later presented results of a novel high-force DEA system. Afterwards, the concept and the design of such a compact DEA system for the 100 N level are presented in Section 4.2. This paragraph also includes the characterization data of the different components (DEAs and biasing mechanism) as well as data for the final prototypes.

4.1 State-of-the-art high-force actuation

Many different DEA configuration have been proposed in the recent literature and the ones with the highest force output are collected and are introduced within this section. All subsequently introduced examples for actuator configurations have different designs, geometries, and use different materials, which influence their performance. For example, a look on equation (2.2) for the Maxwell pressure already shows the importance of the material dependent relative permittivity, which linearly scales the force output. The actuator systems subsequently introduced use silicone, acrylic (VHB4910) or polyurethane with a relative permittivity of 2.8 [45], 4.7 [43] and 7 [45], respectively. The reader should keep this in mind, when comparing the performance of the different actuators. Therefore,

the following paragraph should give an overview of actuator configurations and their absolute performance to help the reader classifying the presented research.

The first actuator configurations discussed are stack actuators, which are already introduced in Section 2.2.1. Maas *et al.* [45] manufacture a silicone and a polyurethane based stack DEA generating forces up to 4 N and 10 N, respectively, and a stroke of 350 µm (3.5% of original length). The 2.5 times higher force of the polyurethane actuator is directly related to the 2.5 times higher relative permittivity. Kovacs *et al.* [47] presented a similar actuator (with approximately 400 layers) based on an acrylic elastomer capable of lifting 2.1 kg approx. 2.5 mm (10% of original length). Due to the use of the thickness compression for actuation only, the stroke of stack DEAs is quite limited. A different actuator design for generating high forces are roll actuators described in Section 2.2.3. Pei *et al.* [70] introduced an enhanced version of this type, where the DEA film is wrapped around a spring. They achieve 21 N and a stroke of 10 mm (23% of active length) with an acrylic elastomer (VHB4910). The third DEA type are membrane actuators (see Section 2.2.2). Kofod *et al.* [43] reported for a rectangular uniaxial strained sample a blocking force up to 6.6 N using an acrylic elastomer. A special configuration of the membrane DEAs are the COP-DEAs, which generate an out-of-plane movement. Wang *et al.* [115] proposed such an actuator based on an acrylic elastomer with a stroke of 17 mm and a maximum blocking force of 5 N when three layers are stacked, which is already relatively high in comparison to the typical force output of COP-DEAs, which is in the hundreds of millinewton-range.

Simulation results using the model of Rizzello *et al.* [65] and studies of the geometry influence on the performance (stroke and force output) of membrane actuators (see Section 3.3) show the potential to push the silicone-based membrane DEA technology from the hundreds of mN-range up to the 100 N level and above. The development of a DEA system prototype, proving this forecast, is described in the following Section 4.2.

4.2 Design and characterization of a high-force actuator system

In this section a novel DEA system integration concept is described, which allows a very compact overall size accompanied by high-force generation. The feasibility of the concept is shown with the assembly of two prototypes. However, before the assembly the single

components of the actuator system are characterized to perfectly match them together. Finally, two versions of the high-force DEA system are manufactured and their performance is recorded. The first system is capable of lifting 10 Kg, while the second one is designed to act against a spring load generating a force of 87 N.

4.2.1 Actuator system concept and manufacturing

The actuator system mainly consists of three parts: Membrane DEA stack, biasing mechanism and casing. The goal of this work is to combine these elements in a very compact way to an actuator system with high force output. Therefore, the systematic approach described in Section 3.4 is used. It starts with the characterization of the load, which can be done analytically for a mass and a spring. Both force characteristics of the loads are represented by a straight line, which is horizontal for the mass and has a slope of the spring stiffness for the spring load (see Figure 3.6 (a) and (b), respectively).

Membrane DEA design and manufacturing

For the contemplated actuator system, a modified version of the COP-DEA design (shown in Figure 3.13), which is better suited for high-force applications, is developed. Selecting the DEA type already finishes step two of the design process. The DEAs are manufactured utilizing the 50 µm silicone *Wacker ELASTOSIL®* film for the elastomer layer and a mixture of silicone and carbon black for the compliant electrodes. The frame is manufactured with epoxy material, which similarly to the electrode applied via screen-printing with the process described in Section 2.4.

The next step in the design process is the selection of the DEA geometry. As shown in Section 3.3 the stroke of such a DEA is dictated by the electrode-ring width, while the force increases with the average electrode-ring circumference. Equation (3.18) can be used to calculate the electrode-ring width l_0 based on the following constrains:

- The material strain induced by the deflection of the DEA's center disc should be smaller than $\lambda_{max} = 30\%$, due to its biaxial nature as well as the pre-stretch of 20% applied during the manufacturing.
- At rest of the actuator system, the DEA's center disc needs to be deflected already to separate the low and high voltage curve. This pre-deflection is

indicated by $x_{LV} - O_{D,x}$ in Figure 3.26 (b) and should cause approximately 5% strain in the material.

- A stroke of approximately 3 mm should be achieved with these prototypes.

Therefore, the electrode-ring width is chosen to be 7.5 mm (based equation (3.18)), which allows a DEA's center disc displacement d of 5.5 mm (3 mm stroke and 2.5 mm pre-deflection). For a compact overall size the maximum DEA size is chosen to be 75x75 mm², which dictates the outer diameter to be 65 mm (additional space for the frame needed) and the inner diameter to be 50 mm. Defining all geometric parameters also determines the maximum force output per DEA layer. Figure 4.11 shows the predicted DEA curves (using the method of Section 3.3.1) and compares them with real measurements of such a DEA.

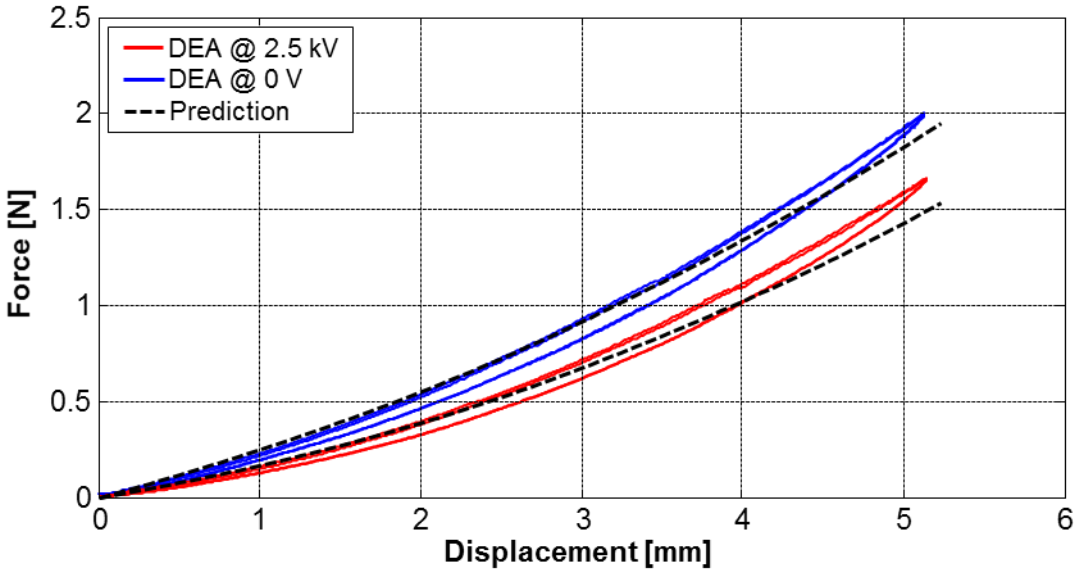

Figure 4.1: Comparison of predicted and measured force-displacement characteristic of a DEA with ID=50 mm and OD=65 mm. The prediction is based on the training data set of a nine times smaller DEA shown in Figure 3.17 (a).

As mentioned in Section 3.4 the force output of a DEA system can be increased by stacking several membranes. The force scales linearly with the number of layers [62] (see also Figure 3.23 (b)). Therefore, a folding process after the screen-printing is introduced to manufacture double-layer DEA modules.

In addition to doubling the force, folding has two more advantages. First, it reduces manufacturing effort, due to the frame material just being printed onto one side of the silicone film (see Figure 4.2 (a) and (b)). Second, after folding, the high voltage electrode is

in the center of the DEA module (see Figure 4.2 (c) and (e)) and thus shielded by the ground electrodes on top and underneath. Additionally, only three printed electrode-layers are needed for the double-layer module.

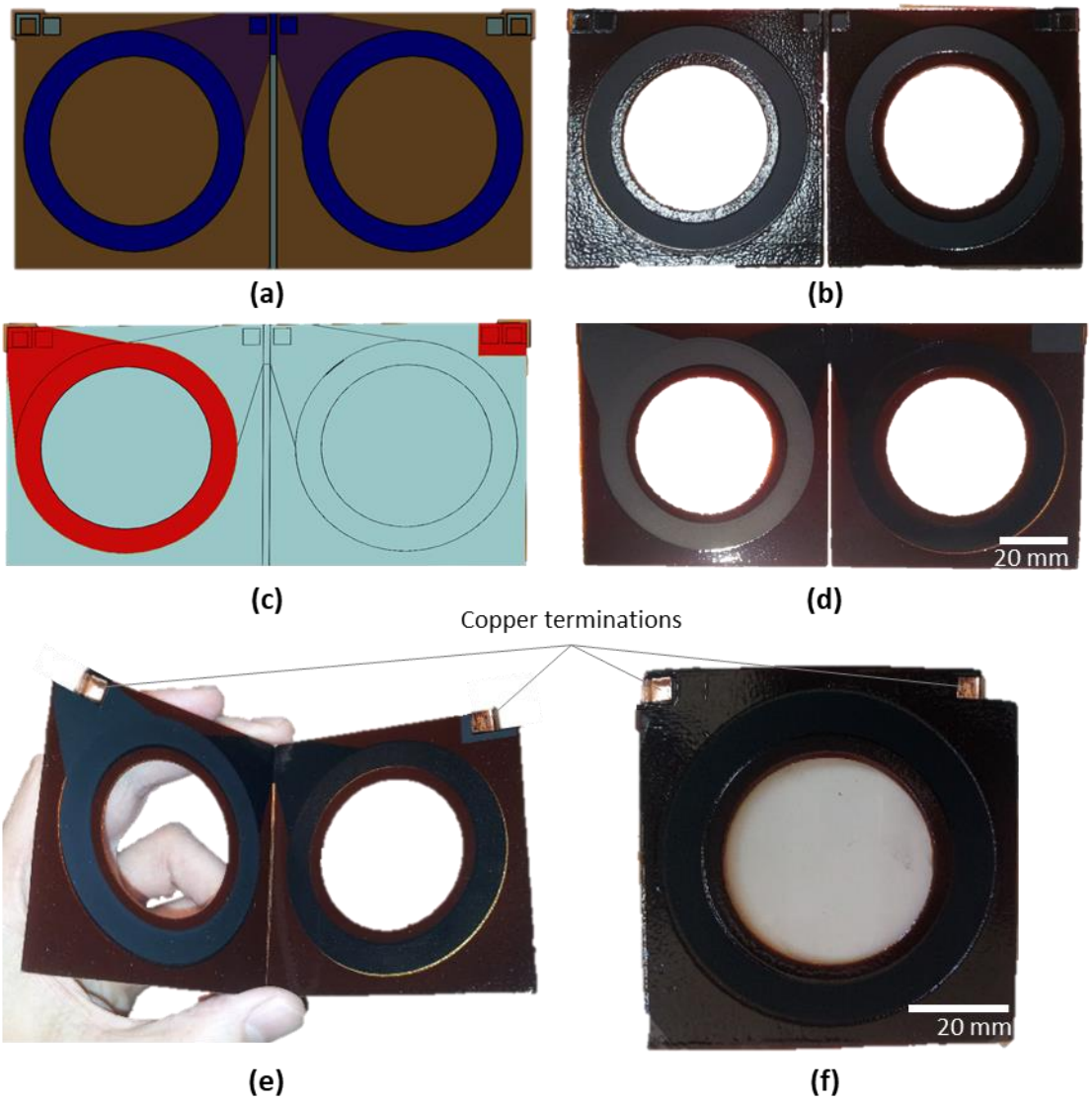

Figure 4.2: (a) CAD picture of the outside with the low voltage electrode (blue, which is partly covered by the frame (brown) and (b) corresponding photograph. (c) CAD picture of the inside with the high voltage electrode (red) and (d) corresponding photograph. (e) Fully printed DEA before folding with blocked out center disc. (f) Folded double-layer COP-DEA module with coper terminations for a low-resistive electrical interconnection.

For a low-resistive and planar electrical connection to the individual electrode-layers, copper tape is applied as electrical terminations during the folding process (see Figure 4.2 (e) and (f)). The copper terminations are also used to interconnect the individual DEA modules by simply stacking them on top of each other and subsequently clamping the

whole unit (see Figure 4.3). This allows for a very low-resistive electrical connection to all DEA modules, which also reduces lifetime problems, which occur, e.g., when punching a pin through stacked layers [80].

Another important feature of the DEAs is the empty area of the center disc (see Figure 4.2). This area opens up an opportunity for compact integration of the biasing mechanism, which is described in the subsequent section.

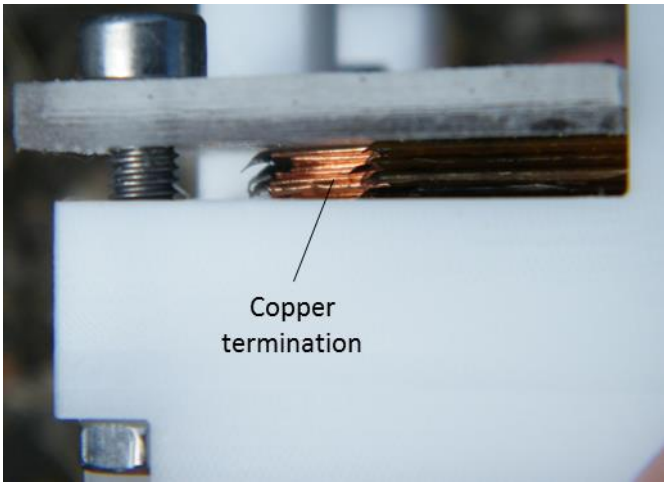

Figure 4.3: Electrical connection of DEA modules within stack via applied copper tape. Stack is already mounted into the casing shown in Figure 4.9.

Biasing mechanism

As mentioned before, the COP-DEAs need to be biased to generate a reasonable stroke and force output (see Section 3.1). The best results are gained by a combination of linear spring (LS) and NBS [95]. Only this combination allows to match the characteristic of the DEA module stack as well as the load characteristic.

A buckled beam mechanism is chosen to design the NBS. The mechanism is actually made of a metal cross (see Figure 4.4 (a)), which represents two buckling beams rotated by 90° to each other. The metal cross, which consists of a laser cut hardened spring-steel 1.1274 (C100S) is inserted into a slightly smaller compression-frame (Figure 4.4 (b)) and clamped afterwards. The compression causes the center of the metal cross to buckle out, resulting in a bi-stable biasing element with a region of negative spring-rate in-between the two stable out-of-plane buckling positions (exemplary force-displacement data is shown in Figure 4.5 (b)). To calculate a compression rate, only the active beam length l_a is considered (see Figure 4.4 (a)). For example, a compression of 96% means that the distance

between the center-clamp and the edge clamping of the NBS is equal to 0.96 times l_a. Note that l_a in this case corresponds to $l_0/2$ in the NBS design routine of Section 3.2.

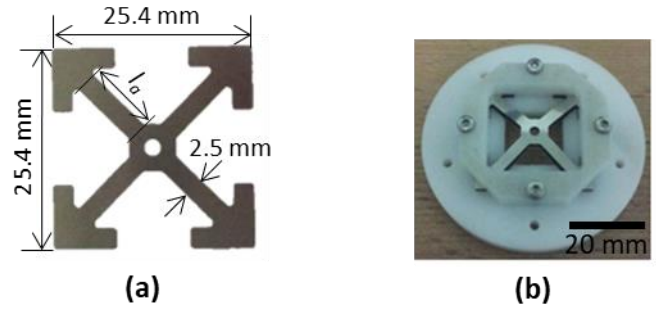

Figure 4.4: (a) Laser cut spring steel cross, which is used as a NBS when constrained in a (b) compression-frame (prototype made of Delrin®) with smaller outer dimensions. The frame can house a stack of metal crosses.

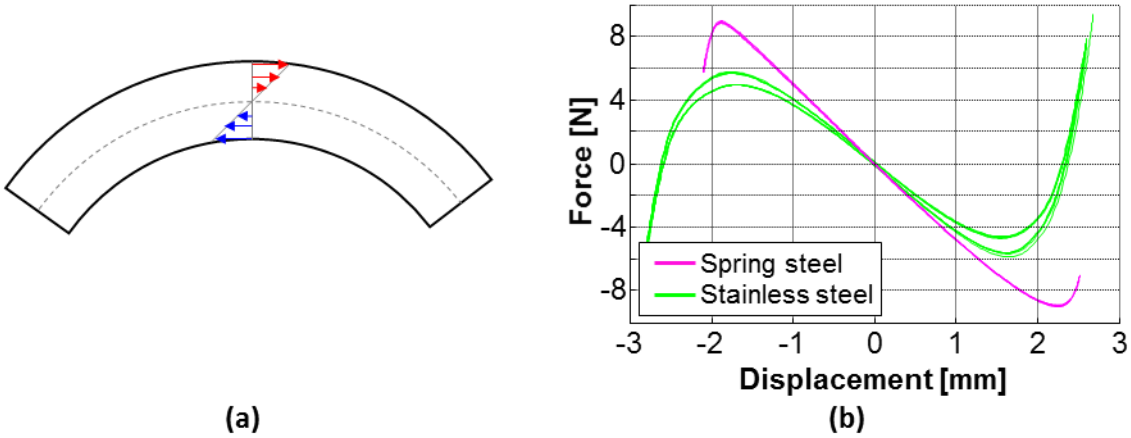

Figure 4.5: (a) Cross-section of a bended beam with resulting tension (red) and compression (blue) stress. (b) Comparison of a NBS made of stainless steel (1.4310 (X10CrNi18-8), yield strength 195 MPa, Young's modulus 200 GPa [121]*) and one made with hardened spring steel (1.1274 (C100S), yield strength 2000 to 2200 MPa, Young's modulus 210 GPa* [122]*). Both are geometrically identical (geometry shown in Figure 4.4, thickness 100 µm) and are mounted into a 96% compression-frame.*

The negative spring rate of such a NBS is influenced by several parameters, for instance beam width, beam thickness, or compression (see Section 3.2). The beam width influences the force difference between the minimum and the maximum linearly, while the thickness has an exponential influence, and thus it is the parameter to be increased for generating high forces. However, there is a limit for the thickness, due to potentially high tension and compression stresses during the bending deformation of the metal beams. This stress

increases linearly with the distance from the neutral axis of the beam (see Figure 4.5 (a)) and should be lower than the yield strength of the material, which is in the range of 2 to 2.2 GPa [122] for the used spring steel. Exceeding the yield strength results in plastic deformation causing a dramatically reduced lifetime as well as an increase of the hysteresis in the force-displacement characteristic of the NBS. Additionally, the energy dissipated in the hysteresis causes a reduced force-difference. The measurement of two geometrically identical NBSs, shown in Figure 4.5 (b), shows these effects.

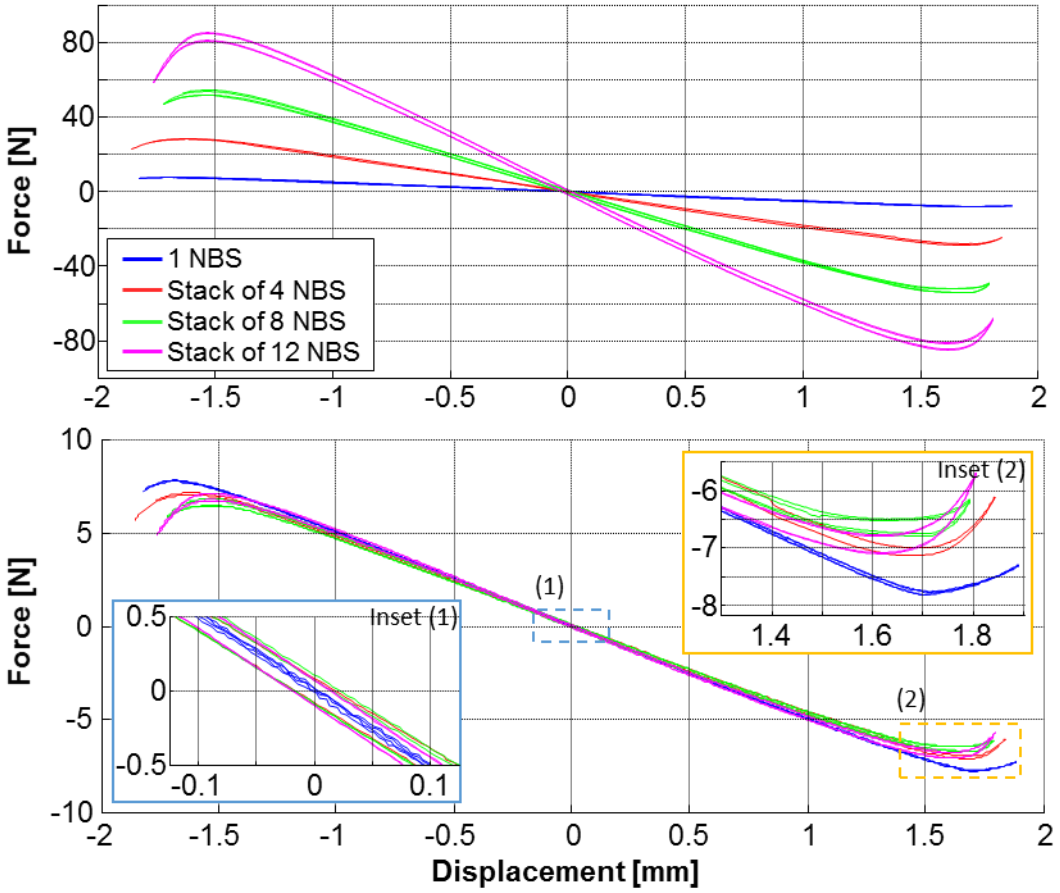

Figure 4.6: Top: Force-displacement characteristic of metal cross stacks with different numbers of metal-crosses (geometry shown in Figure 4.4, thickness 100 µm, and compression-frame 97%). Bottom: Normalized (divided by the number of stacked NBS) force data showing an increase of hysteresis as well as a decrease of the force difference, when metal crosses are stacked.

To avoid exceeding of the yield strength even for the spring steel, several thin metal crosses need to be stacked to achieve high force differences. Figure 4.6 (top) shows the result for several stacks from one to 12 metal crosses. Normalizing this data with the number of stacked metal crosses reveals that the negative stiffness increases linearly with

the number of stacked metal crosses. In addition, the hysteresis increases and the force as well as the displacement difference between the extrema decreases slightly.

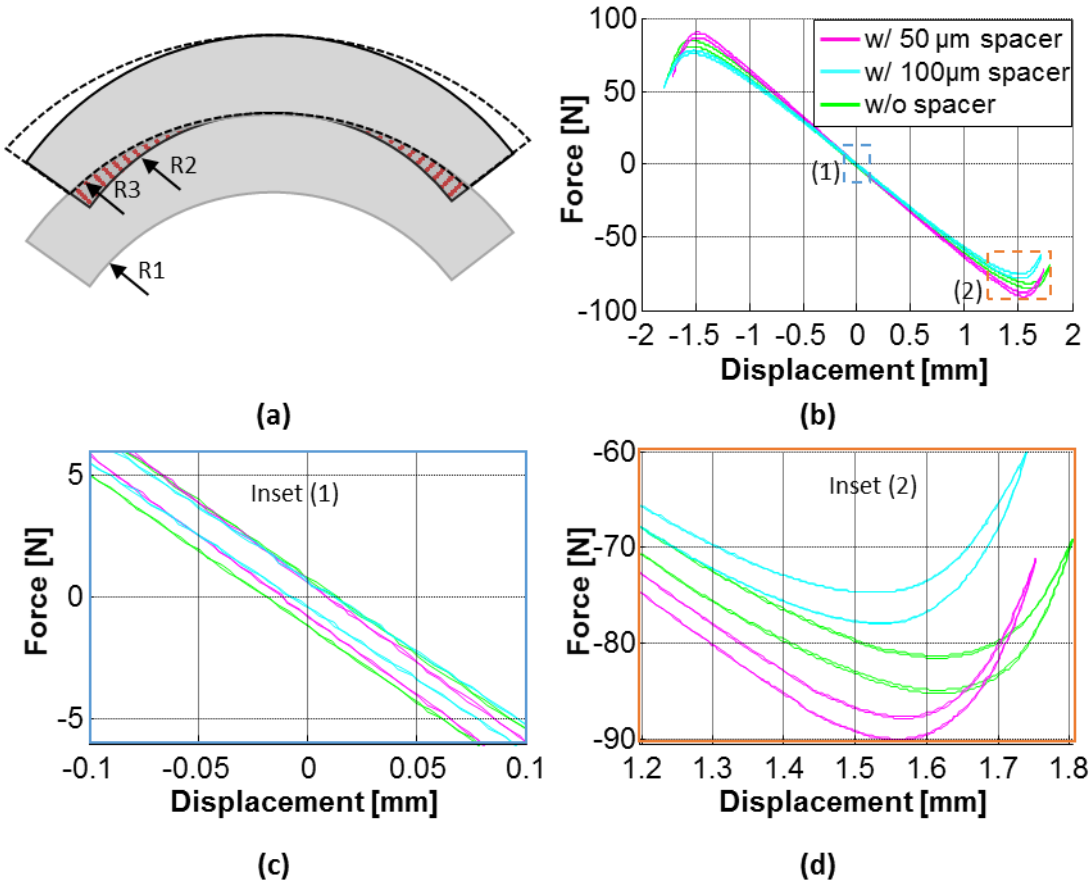

Figure 4.7: (a) Cross-section of two stacked beams. The two beams are intended to have the exact same curvature (R1=R2) to create the intended force. However, they block each other when bending (hatched area), which is resulting in the different curvatures (R1<R3). (b) Comparison of three NBSs made of 12 stacked metal crosses (geometry shown in Figure 4.4, thickness 100 µm, compression-frame 97%) with 50 and 100 µm thick spacers as well as without spacers. (c) Inset (1) shows that the hysteresis close to the origin is slightly smaller with spacers. (d) Inset (2) also indicates a slightly reduced hysteresis, while there is no trend for the minimum achieved force.

One possible reason for the increased hysteresis when stacking multiple NBS elements is increased friction during bending (see Figure 4.7 (a)). Therefore, the influence of spacers in the clamping area of the metal crosses to separate them is studied. Figure 4.7 (b) shows comparative measurements of NBSs consisting of metal crosses stacked and separated with 50 and 100 µm thick spacers as well as without spacers. However, the differences between the three stacks are small. The ones with spacers exhibit a slightly smaller hysteresis (Figure 4.7 (c)). No clear trend for the force difference is visible (Figure 4.7 (d)).

Due to the hysteresis being sufficiently low in all cases and given that the stiffness can be adjusted with the LS, this effect is neglected.

For the LS of the biasing mechanism, a combination of two linear compression springs is chosen. Two springs allow to better fine-tune the overall stiffness with commercially available springs and to achieve a smaller blocking length, while maintaining high pre-compression forces. The two springs have different diameters so that the smaller one can be placed within the larger one, to achieve a high compactness (see Figure 4.8).

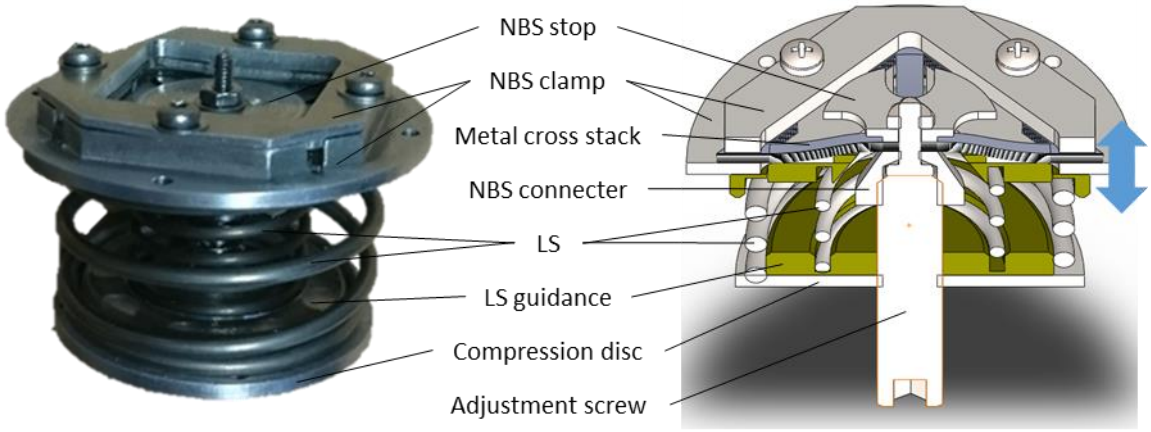

Figure 4.8: Photograph and CAD model cross-section of an assembled biasing mechanism with two compressed LSs.

At the final version of the biasing mechanism, the compression-frame is made of aluminum instead of plastic to avoid material creep (see Figure 4.8). The whole biasing system can be assembled as a standalone subsystem. First, the metal cross stack with spacers is clamped between the NBS clamp top and bottom part, which is held together by four M2 screws. The center of the metal cross stack, the NBS stop, and the NBS mount is bolt together with a M2 screw, which is mounted into the threaded NBS connector. This subassembly forms the NBS. The NBS is then mounted together with the adjustment screw, which is a M6 set screw. In contrast to typical NBSs of this type the center of the NBS stays fix, while the NBS clamping frame is now allowed to move up and down between the two stable positions (indicated by blue arrow in Figure 4.8). This is important for the compact overall design, because the NBS clamp is later connected to the DEAs. Finally, the two LSs are mounted underneath the NBS and are compressed with the LS compression disc. The compression disc can be threaded up and down on the adjustment screw to fine tune the LS compression. Two LS guides, a disc with a groove for each of the LSs, ensures they are

properly centered to avoid an unbalanced/ tilted system. The NBS stop, on top of the biasing mechanism, limits the upwards movement of the NBS by acting as a hard stop for the bottom part of the NBS clamp. This is necessary to prevent the NBS from being damaged by the pre-compression forces of the LSs.

Overall system integration

Finally, the biasing mechanism and the DEA module stack need to be combined into an actuator system. Figure 4.9 shows a CAD model and a photograph of the assembled system, where the biasing mechanism is mounted in the center hole of the DEA module stack for compactness. The overall actuator system has a size of 86x86x25 mm³ (incl. casing). The outer frames of the stacked DEA modules are bolted down with the aluminum actuator cap (see Figure 4.10 (a)), which is covered by a 3D-printed electrical insulation. The insulation is added to insulate the casing just in case of malfunction. The center screws in the front and the back are additionally used to fix the reinforcement bar made of steel, which carries the biasing mechanism. In the front of the actuator, the copper terminations of the individual DEA modules are exposed to make a contact with the power supply. In the photograph (Figure 4.9 (b)), one can see three of the four tappet screws, which connect the biasing mechanism to the center frame of the DEA modules via the DEA tappet (see Figure 4.10).

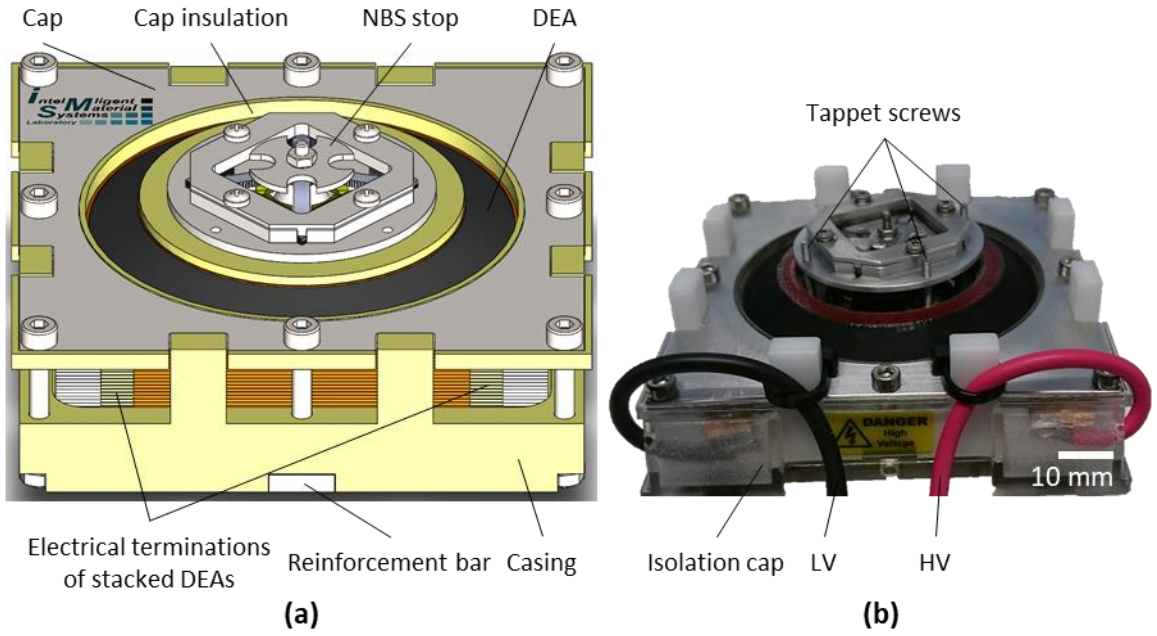

Figure 4.9: (a) CAD drawing and (b) photograph of the assembled actuator system with an overall size of 86x86x25 mm³.

The mechanical interaction for the desired performance is shown in a sketch in Figure 4.10 (b). The biasing mechanism force must be balanced with the force of the partly deflected DEA module stack. This can be achieved by adjusting the position of the biasing mechanism relatively to the DEA module stack (Figure 4.10 (a) and (b), yellow arrow) and by adjusting the LS pre-compression (Figure 4.10 (a) and (b), green arrow), respectively.

The cross-section in Figure 4.10 (a) shows how the mechanical interaction between the biasing mechanism and DEA module stack is realized. The adjustment screw of the biasing mechanism is used to mount it onto the reinforcement bar as well as to adjust the position relatively to the DEA module stack (yellow arrow). The casing made of *Delrin*® covers the reinforcement bar and thus insulates it from the DEA electrodes in case of a malfunction. The DEA tappet (made of *Delrin*®) is connected to the NBS clamp via four screws and deflects the inner frames of the DEA module stack out-of-plane.

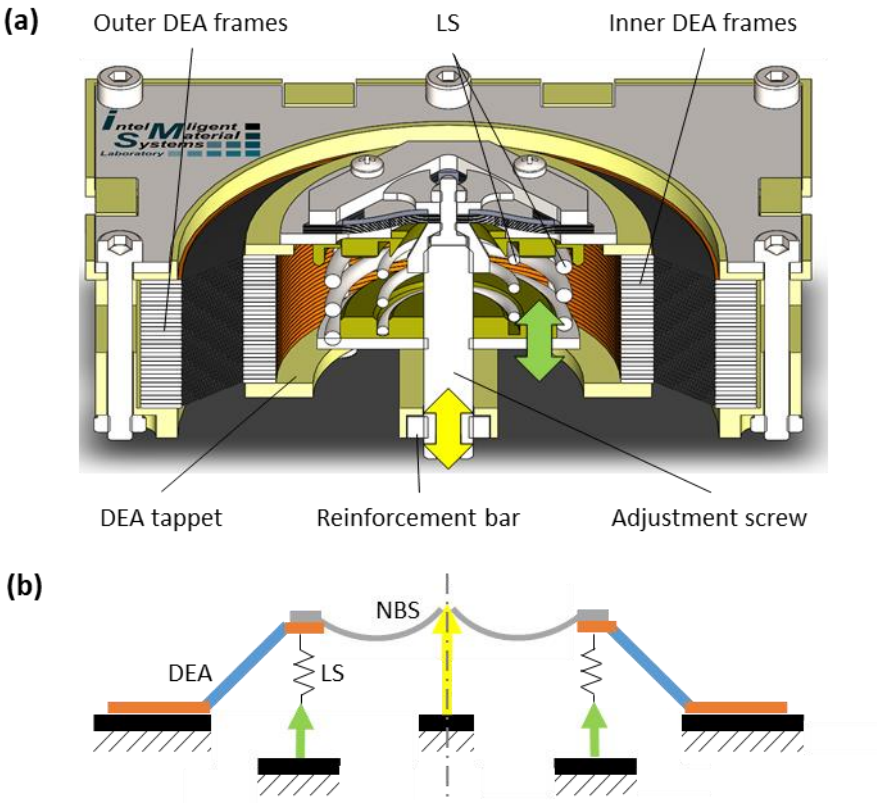

Figure 4.10: (a) CAD model cross-section of the actuator system showing the integration of the biasing mechanism into the blocked out center of the DEA module stack. (b) Sketch showing the mechanical interaction of the DEA stack, NBS, and LS. The yellow arrow in (a) and (b) indicates the possible offset adjustment of the biasing mechanism relative to the DEA stack, while the green arrow shows the possibility to adjust the LS pre-compression.

4.2.2 Characterization of components and actuator system performance

Two different actuator systems are designed and their core components are characterized. One is designed to act against a dead load of 100 N, while the other one is acting against a spring load. Finally, the performance of both systems is evaluated.

Weight lifting actuator

For the first system a stack of ten DEA modules is chosen to have a big enough gap between the low and the high voltage curve (step 4 of design process shown in Figure 3.24). The corresponding force-displacement curves are shown in the designer plot (Figure 4.11 (a)) with the offset of the load (100 N). Afterwards an appropriate biasing mechanism with a stiffness of $k_{SN} = -7.7\ N\ mm^{-1}$ (sum of linear spring and NBS, see equation (3.19)) and a stroke of $\Delta x_{SN} \geq 3\ mm$ needs to be designed to fit between the low and the high voltage DEA curves (step 5 of the design process). A single NBS element, which is suiting the installation space and does not exceed the yield strength of the material, is not capable of giving such a high negative stiffness. Therefore, the strongest one is designed using the method of Section 3.2 and needs to be stacked afterwards. The geometry of the metal crosses with a thickness of 70 µm is shown in Figure 4.4 (a). To form a NBS, it is mounted into a 96% compression-frame. Stacking five of them, separated by 70 µm thick spacers, results in a NBS stiffness of approximately $k_N = -10.2\ Nmm^{-1}$. To reach the desired stiffness and to be able to generate the needed force offset $\Delta F_S \approx 121\ N$ (see Figure 3.27 (a)) the NBS is combined with two linear springs (with a stiffness of 1.36 and 1.1 N mm^{-1}, respectively) to form the biasing mechanism with the characteristic shown in Figure 4.11 (a). This figure can also be used to solve the force equilibrium equation (3.19) of the design process. The shift of the biasing mechanism curve can be used to calculate all individual offsets using the kinematic relations of equations (3.1) to (3.3) of the design procedure (step 6), for instance, the offset $O_{N,D}$ of the NBS relative to the DEA. The stroke $\Delta s = x_{HV} - x_{LV}$ of this actuator system is estimated to be 3.55 mm (see Figure 4.11 (c) and (d)).

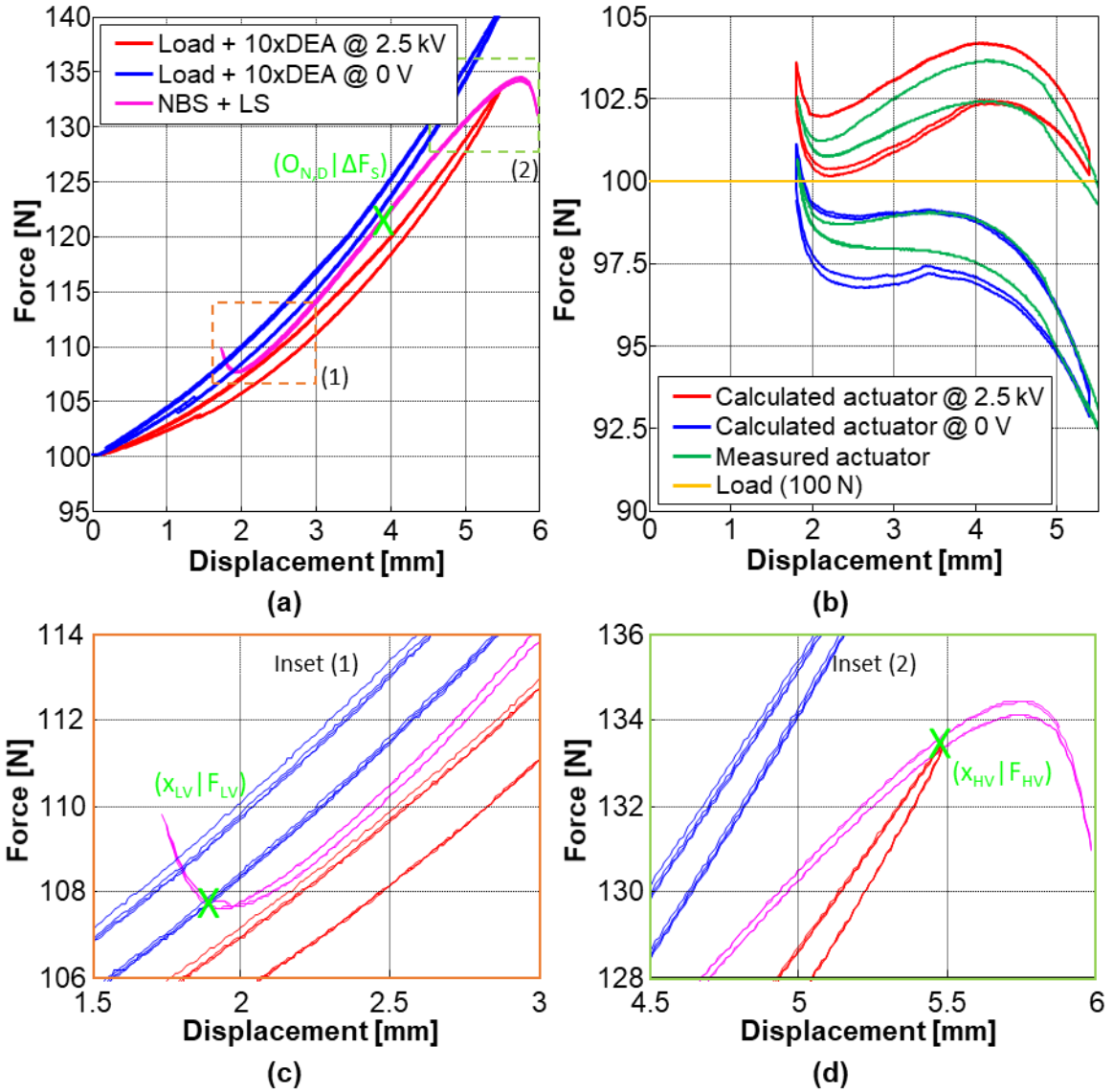

Figure 4.11: (a) Designer diagram showing the equilibria of $F_L + F_D = F_S + F_N$ and (b) customer diagram showing the equilibria of $F_L = F_D + F_S + F_N$. Red and blue curve are calculated with the data plotted in (a) and the green ones are the corresponding actuator forces measured at the assembled actuator. The individual forces of the two diagrams are measured with the high-force setup. (c) Inset 1 showing the intersection of the low voltage curve and the biasing in the designer diagram and (d) inset 2 showing the intersection with the high voltage curve.

Figure 4.11 (b) shows a comparison of the calculated actuator force F_A (blue and red) and the corresponding measured ones (green). The calculated actuator force F_A is computed with the equation $F_A = F_D + F_S + F_N$ (compare to equation (3.20) of the design process) for zero (blue) and 2.5 kV (red). For the calculation, the data plotted in Figure 4.11 (a) is used. The measured actuator force is recorded with the high-force setup

(described in Section 2.5) at the assembled actuator system at 0 and 2.5 kV applied. Both, the calculated and the measured actuator force, show good agreement and hint to a resulting stroke of about 3.4 mm. The smaller hysteresis of the measured actuator force is a result of the smaller displacement range of the DEA during the measurement (4 mm instead of 5.5 mm in the individual force characterization). The lower estimated stroke is a result of imperfections (for instance adjustment of spacers and tilting of individual elements) in the assembly in comparison to the individual measurements.

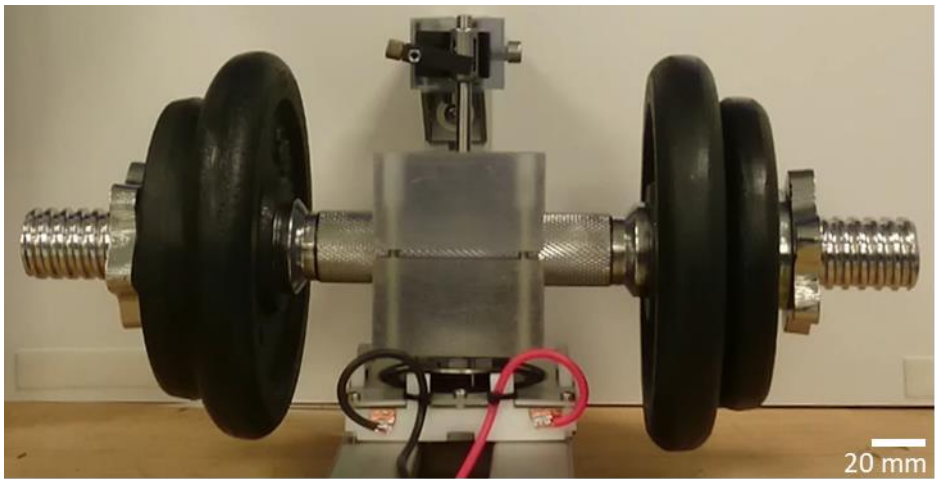

Figure 4.12: Photograph of the actuator system with the 10 kg load on top. The load is guided with a linear bearing (top center of photograph) to prevent it from tilting.

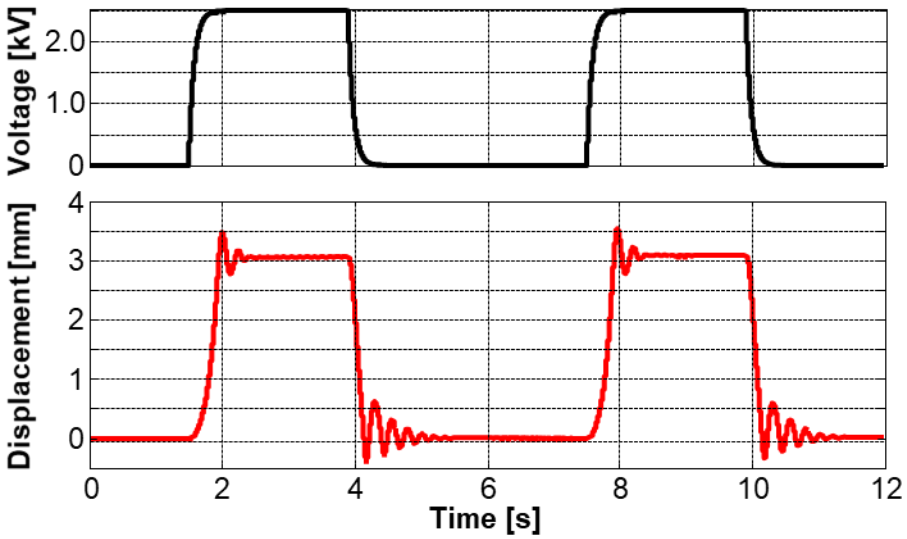

Figure 4.13: Displacement response of the high-force actuator working against a dead load of 10 kg for a square voltage input signal.

After the individual component characterization, the system performance when working against the mass of 10 kg is measured. To prevent the load from tilting it is guided by a linear bearing (see Figure 4.12). The displacement response of the system on a voltage jump from 0 to 2.5 kV is shown in Figure 4.13. After an overshoot to 3.5 mm a steady state displacement of 3.1 mm is achieved, which is close to the prediction made above. The main reasons for the further reduced stroke are imperfections in the alignment and friction.

Spring compression actuator

For the design of this actuator system, the design steps 4 to 6 as described in the previous section for the weight lifting actuator are similarly repeated. First, the number of DEA modules stacked is chosen to be 30. The characterization result of the stack and the intended spring load (stiffness 38.4 N mm^{-1}) are shown in Figure 4.14. The linear force scaling of DEAs via stacking can be seen again, when comparing it with the results of the ten DEAs in Figure 4.11 (a). Afterwards the biasing mechanism needs to be determined using the designer plot shown in Figure 4.15 (a), which is calculated with equation (3.17). The design process follows the same schematics as described in detail for the weight lifting actuator above. However, the biasing mechanism needs to be much stiffer ($k_{SN} = -60.8\ Nmm^{-1}$). To keep the number of NBSs, which need to be stacked, manageable the thickness of the metal crosses is increased to 100 µm resulting in much stiffer NBS elements. This enforces a reduction of the compression rate to 97%, causing a reduced Δx_{SN}, but avoids exceeding the yield strength of the material. However, still 12

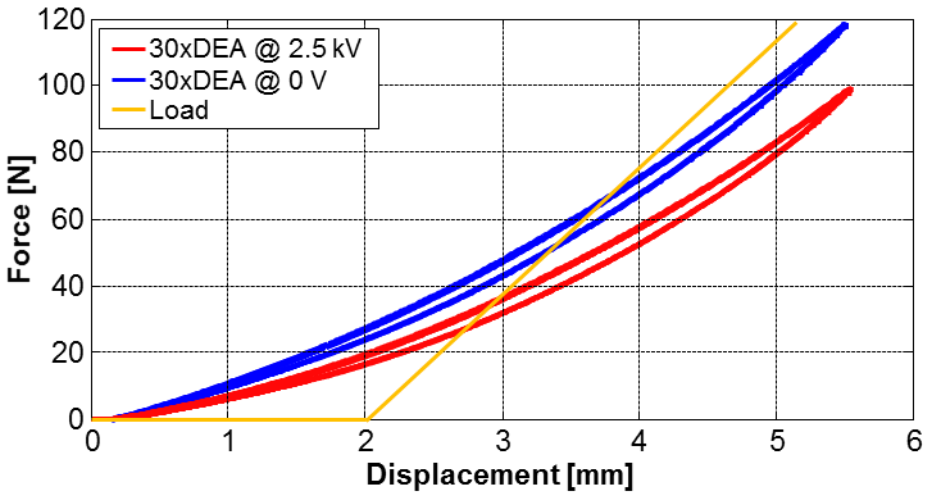

Figure 4.14: Force displacement characteristic of the DEA and the load.

NBSs need to be stacked, which are separated by 50 µm thick spacers. The biasing mechanism is than formed again by combining this NBS with two linear springs having a stiffness of 1.36 and 1.1 N mm^{-1}, respectively (see Figure 4.15 (a)). As can be seen in the two insets (Figure 4.15 (c) and (d)), the biasing mechanism has exactly one intersection with the sum of the DEA modules stacked (at 0 V applied) and the load at the point $(x_{LV}|F_{LV})$ and a second one at $(x_{HV}|F_{HV})$, when 2.5 kV are applied. Between these two points, all three curves are nearly running in parallel. The expected stroke $\Delta s = x_{HV} - x_{LV}$ of such a system is about 2.5 mm.

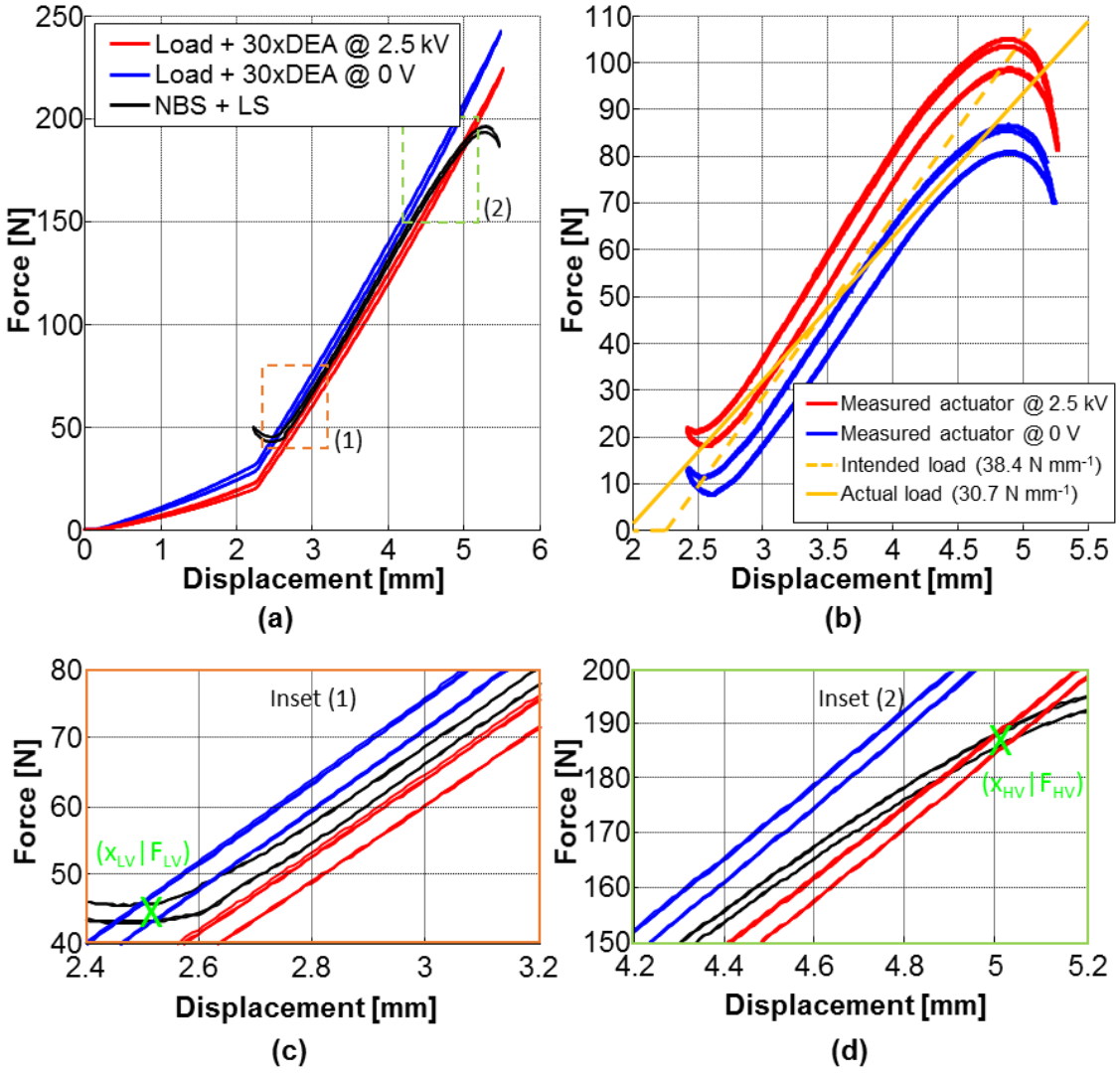

Figure 4.15: (a) Designer diagram showing the equilibriums for $F_L + F_D = F_S + F_N$ with the intended load (stiffness 38.4 N mm^{-1}) and (b) customer diagram showing the equilibrium $F_L = F_D + F_S + F_N$ for both, intended and actual load. The individual forces of the two diagrams are measured with the high-force setup. (c) Inset 1 showing the intersection of the low voltage curve and the biasing in the designer diagram and (d) inset 2 showing the intersection with the high voltage curve.

For the characterization, the actuator system is mounted into the high-force measurement setup (see Figure 4.16). As mentioned above, this actuator system is actually designed to work against a linear spring load with a stiffness of 38.4 N mm^{-1} (intended load), which fits nicely in between the actuator forces (calculated with equation (3.20) from the design process) at 0 and 2.5 kV applied shown in the customer plot in Figure 4.15 (d). However, the stiffness of the measurement setup is not negligible at such high forces. Therefore, the load stiffness needs to be corrected by using equation (2.4) to 30.7 N mm^{-1}, which is plotted as the actual load in Figure 4.15 (b). The lower stiffness results in a lager stroke (approx. 2.7 mm instead of 2.4 mm) and a slightly lower force output prediction (approx. 84 N instead of 90 N). Additionally, the load intersects the hysteresis of the actuator force in a wide range.

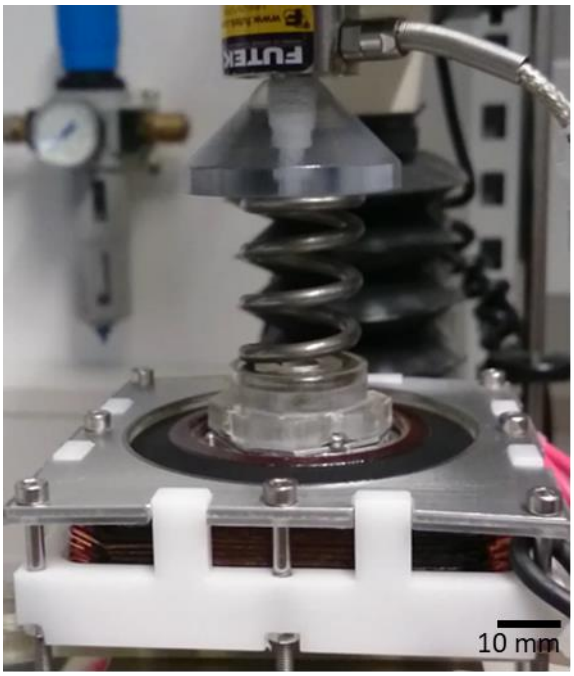

Figure 4.16: Actuator and load spring mounted into the high-force setup for characterization purpose.

After the examination of the single components, the whole system is characterized. When a sinusoidal voltage of 0 to 2.5 kV is applied, the system is able to move 2.8 mm, while generating a force of 87 N (see Figure 4.17). The systematical error of the measurement setup for stroke measurements is already considered. In this configuration, one can clearly see a snapping behavior in the force and stroke plots of Figure 4.17. On the way up the actuator system suddenly pops out when 2.25 kV is reached and snaps back

after the voltage drops below 0.5 kV. The asymmetric bi-stable behavior during sinusoidal excitation is caused by a combination of the NBS characteristic with the viscoelastic effects of the DEA [123]. A closer look at the actuator curves and the intersection of the actual load with the hysteresis shown in Figure 4.15 (c) and comparing this with the displacement results in Figure 4.17 reveals an interesting correlation. The upward jump appears in the region of displacement where the actual load curve leaves the hysteresis of the HV actuator curve, which is the relevant one for the upward movement, while the downward jump is in the region where the actual load curve leaves the LV hysteresis.

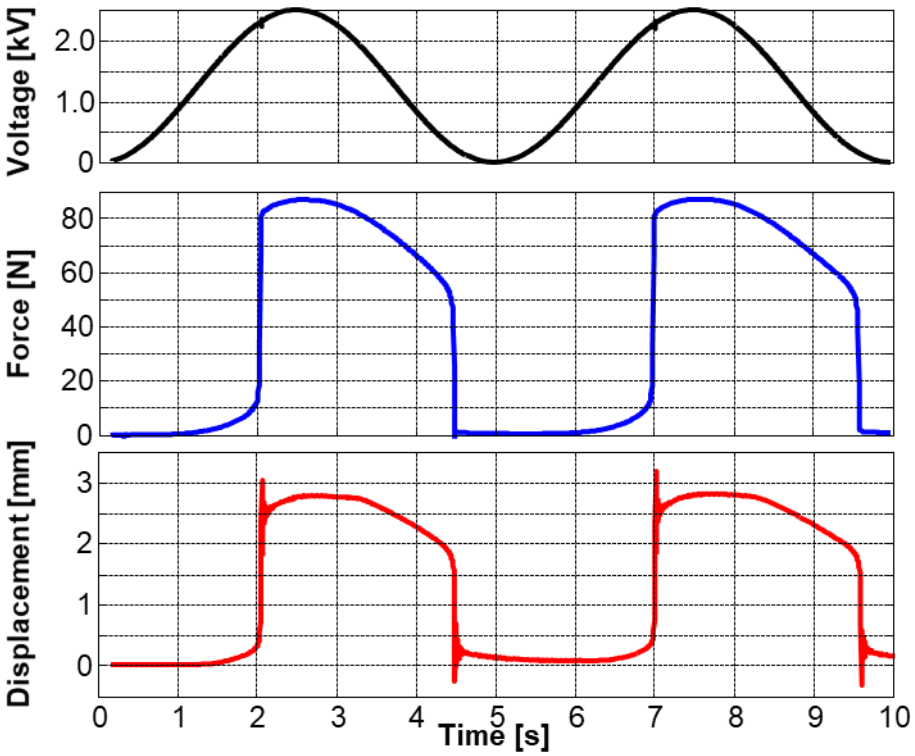

Figure 4.17: Force and displacement response of the high-force actuator working against a LS load for a sinusoidal voltage input signal.

4.3 Discussion of results

A novel manufacturing process for double-layer DEAs using screen-printing and folding is introduced. The process also introduces copper tape as DEA electrical terminations. The copper tape ensures a low contact resistance to the DEA electrodes, due to its planar contact area, as well as low stacking effort together with a very low resistance within a DEA module stack.

The stacking of DEA modules allows to increase the work area linearly with the number of stacked modules. Similarly, this applies to the NBS. Here the force difference increases with the number of stacked metal crosses. To ensure a very low hysteresis of the NBS a material with a very high yield strength needs to be chosen and several metal crosses need to be stacked. Good results are achieved with hardened spring-steel 1.1274 (C100S) sheets with a thickness of 100 µm or less.

The stacking of membrane DEAs and the integration of the biasing mechanism within the passive center of the DEA stack enables very compact designs (86x86x25 mm^3) for actuators with high force output. With the modeling approach of Section 3.4 two demonstrators are designed and manufactured to show the potential of this concept. One is capable of lifting 10 kg up by 3.1 mm, while the second one generates a force of up to 87 N when compressing a linear spring by 2.8 mm. The demonstrated outstanding performance expands the force range of silicone-based membrane DEAs by a factor of about 200 compared to state-of-the-art COP-DEA actuator systems. This allows DEAs to compete with solenoids or pneumatic cylinders in several applications.

From a scientific point of view, the increase of the hysteresis when stacking metal crosses for a strong NBS should be studied in more detail. The first results for adding spacers between the metal crosses in the clamping area do not show a clear trend. However, they hint that this could help slightly suppressing the formation of a hysteresis.

Chapter 5 High Stroke Actuator Systems

This chapter is based on the journal paper [124]. It gives a review on DEAs exhibiting large actuation strain to classify the presented work, followed by the motivation why SIP-DEAs are suited best to compete with them. Finally, a SIP-DEA system, which has low complexity, high actuation strain larger than 50%, and very fast actuation, is presented. The presented actuation strain is about 10 times larger than the one typically obtained by DEA systems biased by material pre-stretch, a mass, or a spring.

5.1 State-of-the-art high stroke actuation

As been shown in the previous chapters the biasing mechanism again plays an important role. This is also valid for generating high actuation strains. In [91], Hodgins *et al.* compared the performance obtained with different biasing mechanisms (mass, LS, and NBS) for COP-DEAs. In this work, the best result in terms of stroke are obtained with a NBS, which results in a stroke 2.5 times higher than the one obtained with a mass. The combination of negative stiffness mechanisms with in-plane DEAs is first introduce by Pelrine *et al.* in [125]. By using an over-center-mechanism, the strain of a SIP-DEA is increased by a factor of five to approx. 15% actuation strain compared to a neutrally loaded one, i.e., a constant force. The higher performance gain obtained for SIP-DEAs, with respect to COP-DEAs, can be explained by looking at typical force-displacement characteristics of the two different actuator configurations (see Figure 5.1). The linear behavior of a NBS suits much better the approximately linear behavior of SIP-DEAs in a wide displacement range (Figure 5.1 (b)), while a COP-DEA is normally characterized by parabolic curves (Figure 5.1 (a)).

Therefore, the focus of Chapter 5 is on the combination of SIP-DEAs with NBSs, starting with an overview of related research. For instance, Wingert et al. in [126] combines a DEA, which is clamped into a flexible hexagonal frame, with an NBS. The resulting stroke is

doubled from 4 to 8 mm (equals approx. 40% actuation strain). Berselli and his colleagues even surpassed these results in their research, which focused on studying actuators with constant force output for robotic applications. They proposed rectangular shaped [127] and diamond shaped [93] in-plane DEAs with approx. 50% and 100% actuation strain, respectively. These results are based on analytical models neglecting any loss phenomena, such as friction and viscoelasticity. However, the consistency of the predictions are confirmed by experiments of Plante [60] (see Figure 2.6) and Vogan [59], who both present an actuation strain larger than 100% for VHB based diamond shape DEAs, which is, to the knowledge of the author, one of the largest reversible actuation strains demonstrated for in-plane DEAs. Larger actuation strains, like the record-high 380% demonstrated in [9] are typically not reversible. Another advantage of SIP-DEAs, in addition to the high actuation strains, is that they allow building relatively flat systems, due to in-plane actuation, permitting to further increase compactness of the resulting actuator system.

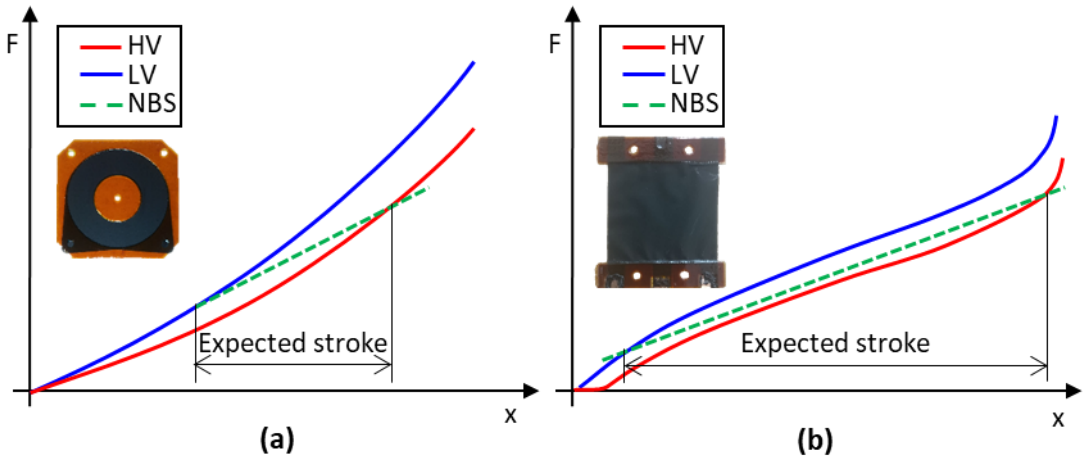

Figure 5.1: NBS (green dashed line) acting against (a) a COP-DEA and (b) a SIP-DEA. The blue curves indicates the LV and the red curves the high voltage HV force-displacement characteristic of the DEA, respectively. Due to the force equilibria between NBS and DEAs, the NBS spring rate switches sign and appears to be positive.

These encouraging results for in-plane DEAs, together with the advantage of SIP-DEAs described by Figure 5.1, motivate the need to investigate further how to optimize the performance of such systems. However, the works mentioned above either use complex DEA configurations like the diamond shape or studies theoretical systems of simpler SIP-DEAs with conceptual NBS mechanisms. Therefore, the scope of this work is the combination of simple to manufacture SIP-DEAs and NBSs to a practical system of low

complexity and high actuation strain. In addition, the use of silicone should enable actuators with very high actuation speed. The SIP-DEAs used in this work are based on a rectangular silicone membrane coated with electrodes on both sides. Two of its opposing edges are constrained by stiff frames, while the other two are free to move. After the manufacturing of the SIP-DEAs, electro-mechanical characterization is performed. With the aid of these results, two DEA systems are designed and characterized. In particular, the first system uses a linear spring for biasing only, while the second one is using an additional NBS in conjunction with the linear spring. Finally, the performance of the two systems is compared.

5.2 Design and characterization of a high stroke actuator system

The actuator considered in this work uses a SIP-DEA as active component. It is coupled with a passive biasing element, such as a spring. If a high voltage is applied to the DEA, its in-plane stiffness decreases and the pulling force of the biasing element elongates the DEA strip. The resulting stroke is denoted as Δs in Figure 5.2. In this work, a linear spring in comparison with a NBS plus a linear spring as biasing element is studied.

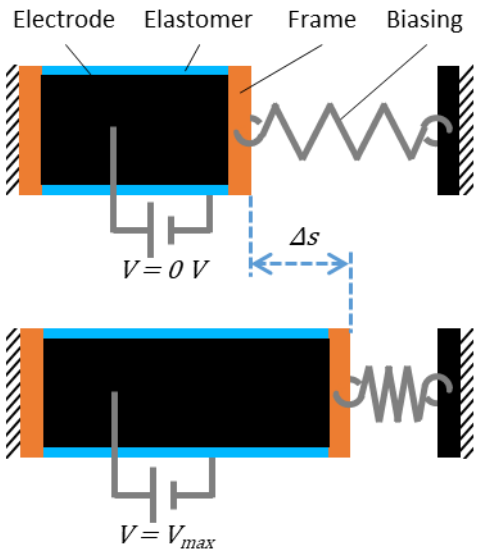

Figure 5.2: Concept sketch of a SIP-DEA coupled with a biasing element (tension spring). An electrical stimulation causes the SIP-DEA to expand about Δs.

5.2.1 Actuator design and manufacturing

This section starts with a description of the deviation in the manufacturing process of SIP-DEAs in comparison to the general one described in Section 2.4. Afterwards the final SIP-DEA design is presented followed by a brief introduction of the biasing mechanisms used for the high stroke actuator system.

Membrane SIP-DEA

The material used as well as the general manufacturing process is described in Section 2.4. In the following, the deviations are stated. Prior to the screen-printing, a uniaxial (not bi-axial) pre-stretch of 20% is applied to the film in the direction of actuation. The pre-stretch is just used to prevent the film from sagging within the metal frame during manufacturing. It is released again after singulation. The epoxide material, which acts as a solid frame, is applied just on one side of the silicone film for the SIP-DEAs. Figure 5.3 (a) shows a top view sketch of the DEAs within the metal frame before singulation. The cross-section in Figure 5.3 (b) shows the layer composition.

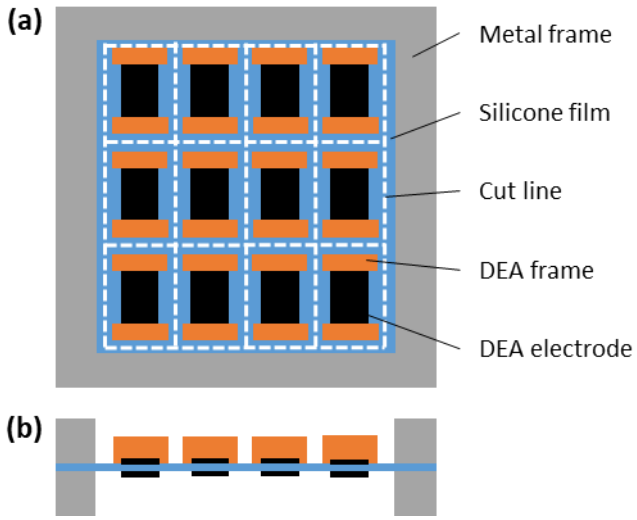

Figure 5.3: (a) Top view sketch of the batch processed SIP-DEAs. (b) Cross-section sketch to illustrate the layer composition.

After the batch processing of multiple DEAs via screen-printing, a scalpel is used to cut them out. Finally, pieces of copper tape are attached as electrical terminations. A strip of 2.5 mm width (see, light blue area), next to the free edges of the SIP-DEA, is not covered with electrode material for insulation and to prevent arcing. To reduce the electrical

resistance, two ground connections are added on the outsides. The center contact is used for the HV connection.

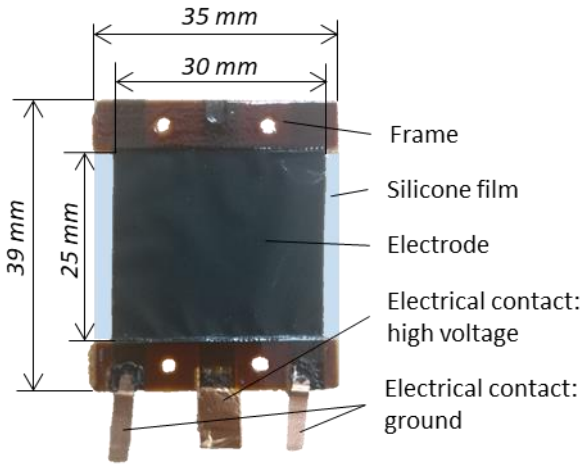

Figure 5.4: Picture including final dimensions (DEA is relaxed, no pre-stretch) of the SIP-DEA manufactured. The uncoated silicone film is highlighted in light blue for a better visibility.

Biasing mechanism

The design of the biasing system is fundamental for determining the performance of the SIP-DEA system. Two different biasing elements are studied in this work. The first one is a simple linear tension spring, while the second one is a combination of a NBS and a linear compression spring. The stiffness of this combination k_B can easily be determined by adapting equation (3.19) to:

$$k_B = k_S + k_N \tag{5.1}$$

with k_S and k_N representing the LS and the NBS stiffness (in the negative region), respectively. Note that k_N must be negative and its absolute value has to be larger than the value of k_S. Overall, the combination of LS and NBS is designed in a way such that the absolute value of k_B matches the stiffness of the SIP-DEA in almost its entire linear range. The NBS itself is similar to the one used for the high-force actuator and consists of a stainless steel cross (1.4310 (X10CrNi18-8), yield strength 195 MPa, Young's modulus 200 GPa [121]), which is mounted into a 3D printed compression-frame (see Figure 5.5). The use of spring steel is not compulsory in the presented actuator system, due to the much lower forces.

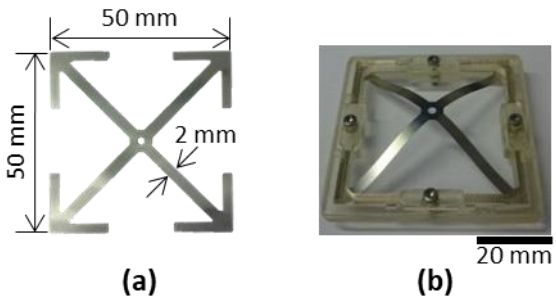

Figure 5.5: (a) Picture of laser-cut stainless steel cross (b) and buckled up steel cross within a compression-frame (scale 1:2).

5.2.2 Characterization of components

To manufacture a DEA system successfully, again all components need to be characterized. In the case of the system with combination of NBS and LS, the force-displacement data of the NBS is used to select a LS with the right spring rate, in order to match k_B with the stiffness of the DEA.

Figure 5.6 shows characterization data of the SIP-DEA at zero and 3000 V, as well as data for the NBS, which is already combined with the LS mentioned in Section 5.2.3. Note how the NBS + LS curve fits in-between the low and high voltage curve of the DEA. The chosen maximum DEA strain of 80% is not a mechanical material limitation, since the used silicone film can sustain more than 200% strain [79]. However, due to the thinning of the film during stretching, the electric field reaches about 108 V µm^{-1} at 80% strain and 3000 V. This value is already above the limit of 80 to 100 V µm^{-1} mentioned in the data sheet.

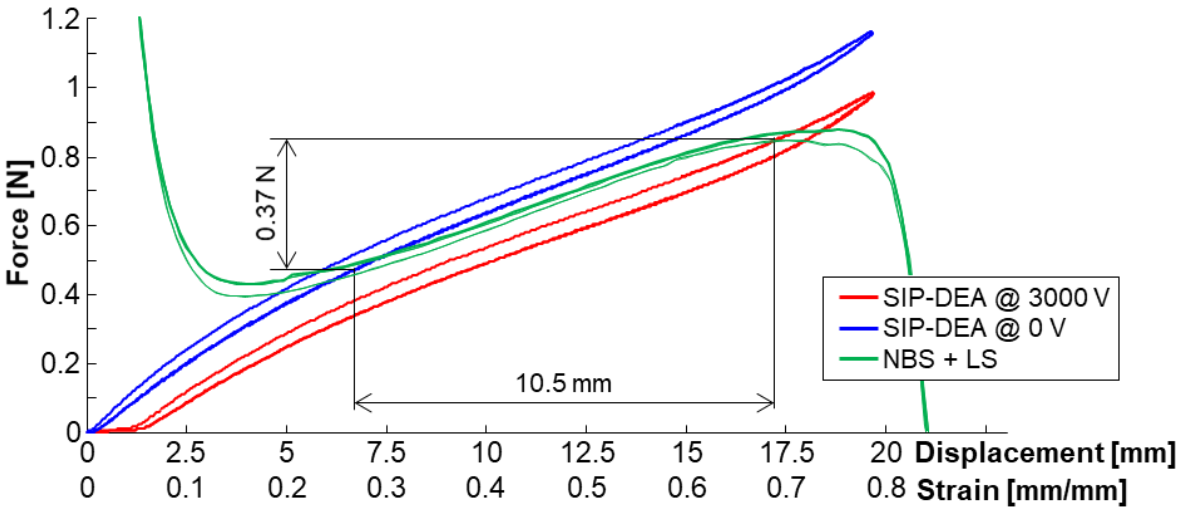

Figure 5.6: Results of the CV test of the DEA at zero and 3000 V and of the NBS-LS-combination.

The hysteresis of the DEA curves is a result of viscoelastic effects, which are typically observed in elastomeric materials [123,128]. To reduce viscoelastic phenomena as much as possible and to avoid at the same time unnecessarily slow experiments, the frequency for the sinusoidal displacement is chosen as 1 Hz. The hysteresis within the NBS measurement is a result of plastic deformation close to the surface, which appears under high bending stress (see discussion in 4.2.1 and Figure 4.5). Therefore, for commercial systems the use of spring steel is necessary.

In addition, Figure 5.6 can be used to estimate the performance of the DEA system graphically. An investigation of the intersection points of the NBS and the DEA at zero and 3000 V applied reveals an expected stroke of 10.5 mm and a force difference of 0.37 N.

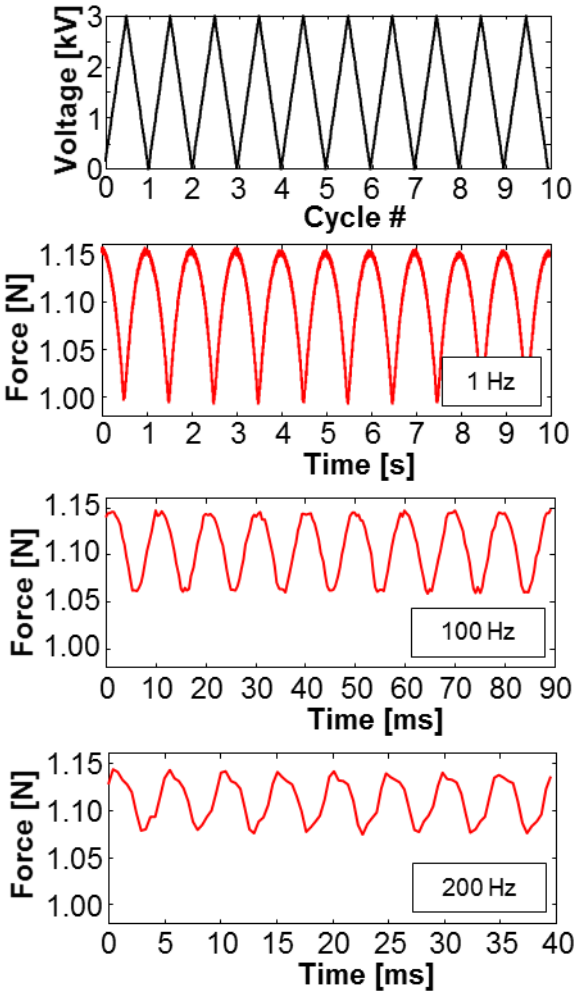

Figure 5.7: Blocking force results of CP test at 80% strain for a triangular input voltage at different frequencies.

The results of the blocking force measurement for a triangular input signal with a peak voltage of 3000 V are shown in Figure 5.7. The blocking force is measured at three different frequencies and at strain of 80%. At 1 Hz the blocking force is 150 mN, which slightly lower than the force gap of 175 mN at 80% strain in Figure 5.6, caused by viscoelasticity in combination with the very short time period, in which the voltage is at its maximum at the triangular shaped input signal. This effect also causes the reduction of blocking force for higher frequencies for instance to 65 mN at 200 Hz. Therefore, triangular input voltages are not well suited to measure the blocking force at high frequencies. Their only advantage, in comparison to a sine signal, is a lower current draw, which is required by the amplifier used. However, Linnebach *et al.* [129] published results for a sine excitation without any drop in blocking force up to a frequencies of 150 Hz for the same actuator geometry. The only additional difference to a more power full HV source is an additional print run when applying the electrode. This results in a slightly thicker electrode layer but reduced resistivity [58]. Nevertheless, the presented data shows, that silicone can be actuated with high frequencies.

5.2.3 Actuator system concept

The first system under investigation consists of a DEA biased with a tension spring, having a stiffness of 0.03 N mm^{-1}. In this configuration, one end, of both DEA and LS, is fixed, while the other ends of both elements are connected and are free to move. The stroke is measured at the coupling end via a laser displacement sensor. The fixed end of the DEA is mounted to a load cell to measure the generated force difference. A sketch of the system is shown in Figure 5.2, while a picture is reported in Figure 5.8.

The second system consists of the DEA and a combination of NBS and LS. In this case, one end of the DEA is fixed to the load cell again, while the other end is free to move, too. The free end is coupled via a rod with the center of the stainless steel cross of the NBS. The LS, which is also fixed at one end, is always maintained under compression during actuation. Hence, it pushes against the center of the stainless steel cross in the direction of actuation (see Figure 5.9). It is important to point out that the NBS-LS combination is always pulling in the direction of motion, in order to keep the DEA under tension. The pull force of the NBS-LS combination can be adjusted by modifying the pre-compression of the LS. The actuator stroke is measured at the center of the NBS.

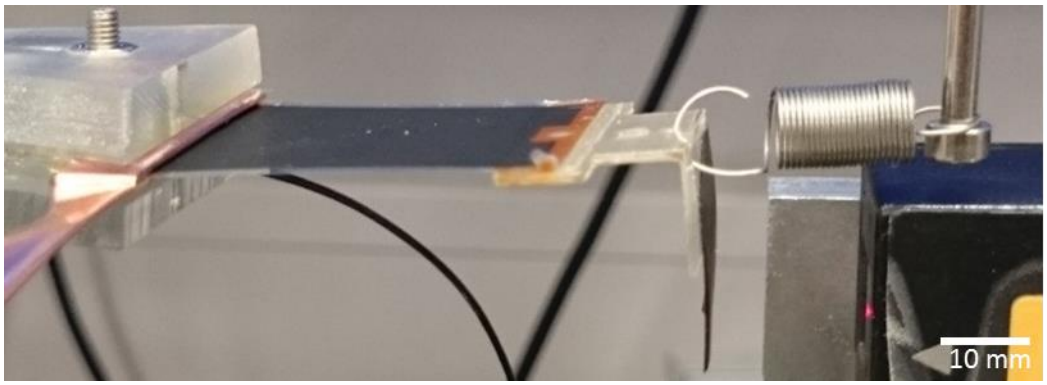

Figure 5.8: Picture of the actuator system consisting of a DEA biased with a tension spring.

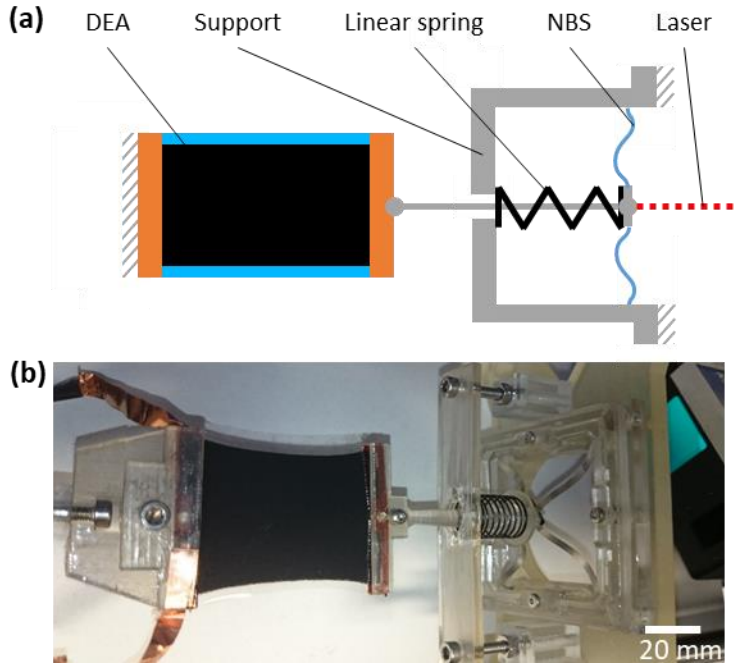

Figure 5.9: (a) Sketch and (b) picture of the actuator system consisting of a DEA and the combinations of NBS and compression LS. The actuator system is mounted into the characterization setup with a laser sensor and a load cell for stroke and force measurements, which is described in Section 2.5.

The stainless steel cross, used for the NBS, has a size of 50x50 mm², a thickness of 75 µm, a beam width of 2 mm, and it is mounted into a frame which compresses the beams to 93% of their initial length (see Figure 5.5). To match the stiffness of the NBS to the one of the DEA, the LS stiffness is chosen to be 0.056 N mm^{-1}.

5.2.4 Actuator system performance

Finally, the DEA systems shown in Figure 5.8 and Figure 5.9 are tested with the low force setup (described in Section 2.5) and compared. Without any voltage applied, both systems

are in equilibrium state. At this point, the DEA is strained by approximately 27% and 60% due to the LS + NBS and the LS biases, respectively. The pre-strain of the LS + NBS system is chosen relatively low in comparison to the LS system, due to the expected higher stroke. At maximum elongation, both systems reach a DEA strain of about 65%-70%, and thus they are subject to a similar maximum electric field. The force and stroke response to a voltage step of 3000 V is then analyzed for both systems. A static displacement of 1.2 and 11.2 mm is reached for the LS and the LS + NBS, respectively (see Figure 5.10 (a)). After the transient oscillation is extinguished, no relevant creep is observed. The systems exhibits an average velocity of 0.07 (LS) and 0.29 m s^{-1} (LS + NBS) between the voltage application and the first stroke maximum.

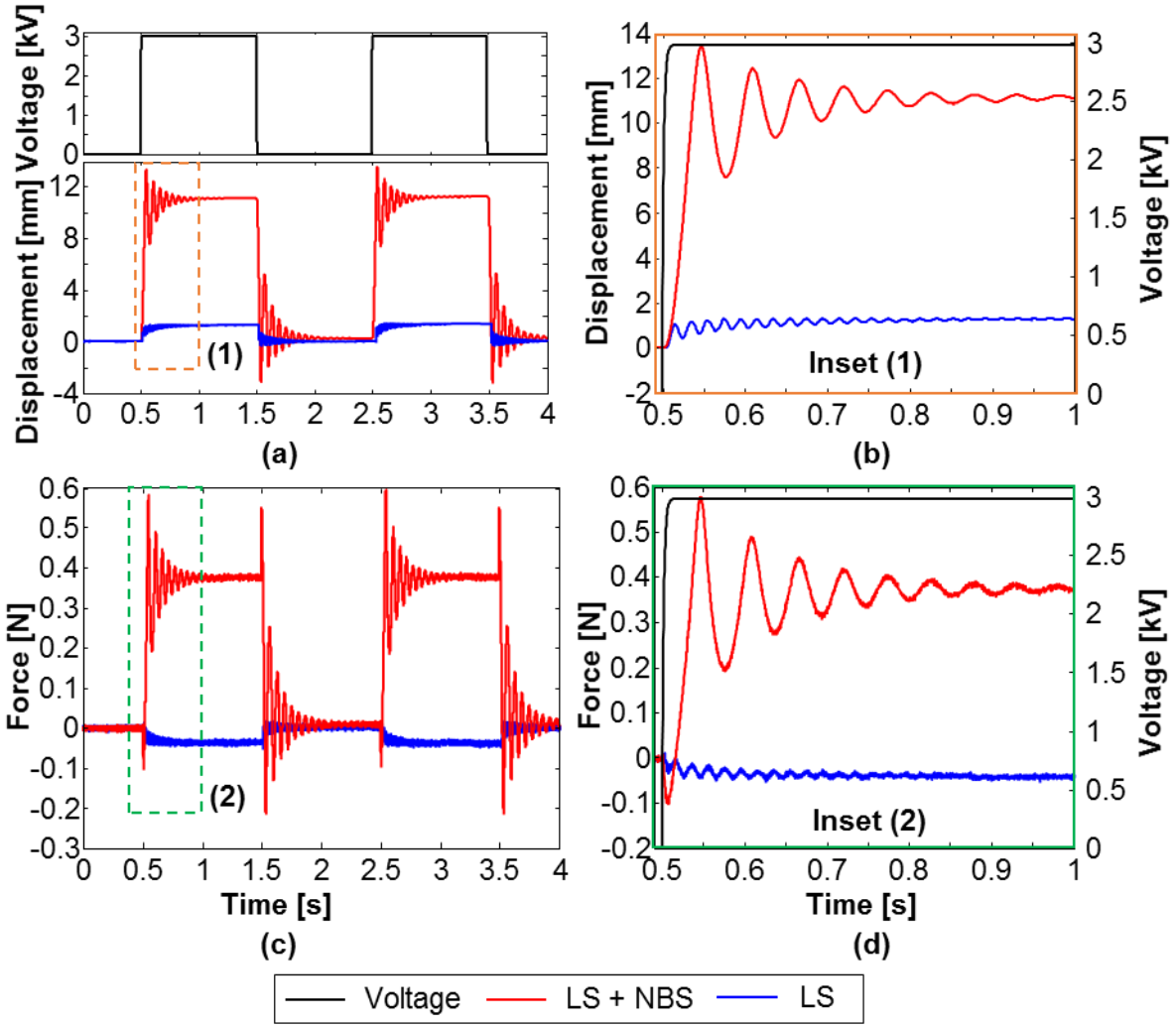

Figure 5.10: Comparison of the performance for both actuator systems build. (a) Actuator stroke response on a voltage step and (b) inset (1) settling of the actuator stroke after activation. In (c) and (d), the same plots are shown for the force response. The force plotted is not the absolute value; it is zeroed at the zero volt equilibrium.

The NBS system exhibits a much higher force difference, as well. The force output of the two systems equals -0.04 and 0.38 N, respectively and is shown in Figure 5.10 (c). Because the expanding DEA allows the tension spring (in the LS bias) to relax partially, the force within the system degreases and the output force of this system is negative. This is not the case for the NBS system. As it can be seen in Figure 5.6, the force increases from the 0 V to the 3000 V equilibrium. The measurement results well agree with the graphical force and stroke estimation, which is performed in Figure 5.6 for quasi-static conditions.

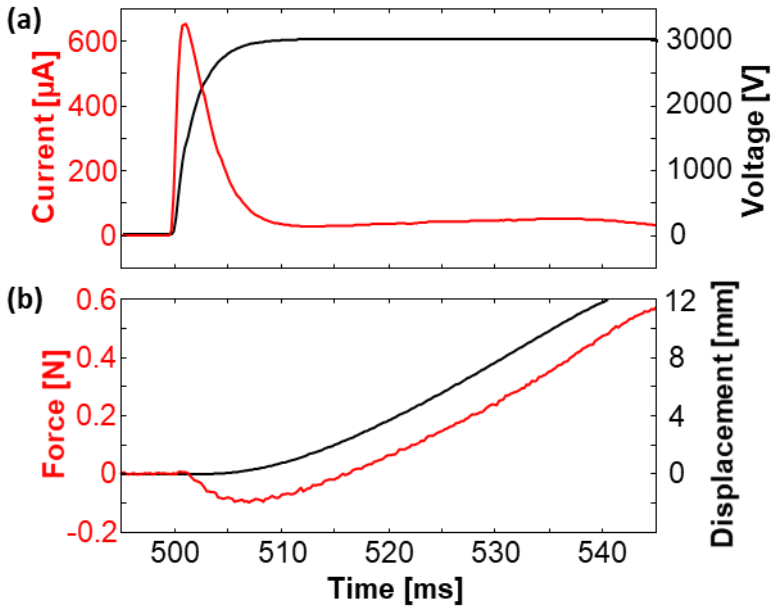

Figure 5.11: (a) Current and voltage vs. time and (b) force and displacement vs. time for the LS + NBS system, respectively.

Figure 5.10 (b) and (d) show the force and stroke response of the two systems immediately after the rising front of the voltage. An interesting fact is that both systems immediately react with a change in force, while the stroke response is delayed. The delay in stroke is caused by inertial and viscoelastic effects. Another interesting effect is the undershoot of the force visible in the first part of Figure 5.10 (d) and Figure 5.11 (b), which is exhibited by the LS + NBS system. This is a consequence of inertia as well and can be understood by inspecting the first milliseconds after the voltage application. The Maxwell pressure, resulting from the applied voltage, is acting instantaneously onto the dielectric already during the capacitance charging. Therefore, it reduces the internal stress of the dielectric material caused by the initial stretch of 27% of the DEA. The reduced stress is measured as a negative force, which is afterwards compensated by the force of the pulling

biasing mechanism. Current measurements showed that the complete charging of the DEA takes about 5 ms, while the force stays negative for 17 ms (see Figure 5.11 (a)). The inverse effect can also be seen when discharging the DEA. The charging time of 5 ms explains again that the DEA is not fully charged when applying a 200 Hz triangular input voltage and thus the maximum blocking force is not reached.

After the dynamic characterization, the quasi-static behavior of the system is studied. As described in [96], a DEA biased with a bi-stable element can be designed to be either stable or unstable. The slope of both, biasing elements and DEA, represents the influencing design factor. As long as the slope of the biasing element (within the operating range) is lower than the slope of the DEA, the overall system is dominated by the DEA, and therefore it exhibits a stable behavior. This means that any small increment in voltage causes a continuous increase in displacement without any jump. If a jump in displacement appears, the system is dominated by the biasing element, and therefore it is (locally) unstable. Nevertheless, an unstable actuator can still be operated in-between two bi-stable positions. Since the slope of both DEA and LS + NBS varies over displacement, the overall system can be tuned to operate in a continuous or bi-stable way, depending on the chosen operating point. The operating point can be influenced by the LS and NBS pre-compression, as well as by the physical offset between the biasing mechanism and the DEA. Changing these parameters causes the NBS + LS curve to shift up/ down and left/ right, with respect to the DEA curve (see Section 3.1 for a detailed explanation), according to the reference frame in Figure 5.6. The different operating modes, stable and critical stable (transition to unstable) operation, for a sinusoidal input voltage (0 to 3 kV, 0.5 Hz) can be seen in Figure 5.12. When increasing the voltage, the critical system jumps from about 3.5 to 8.9 mm when the voltage goes above 2.4 kV and from about 10 back to 2.9 mm, when the voltage is decreased again. At some point within these jumps the biasing mechanism dominates the DEA. The oscillations after the displacement jump indicate that the DEA stabilizes the motion once this condition is reached. The hysteresis in the relation between displacement and voltage is a result of the interaction between bi-stability of the biasing mechanism and the hysteresis of both, DEA and NBS. A detailed and systematic investigation on the stability as well as measurements for a completely unstable operation of similar systems is shown in [130].

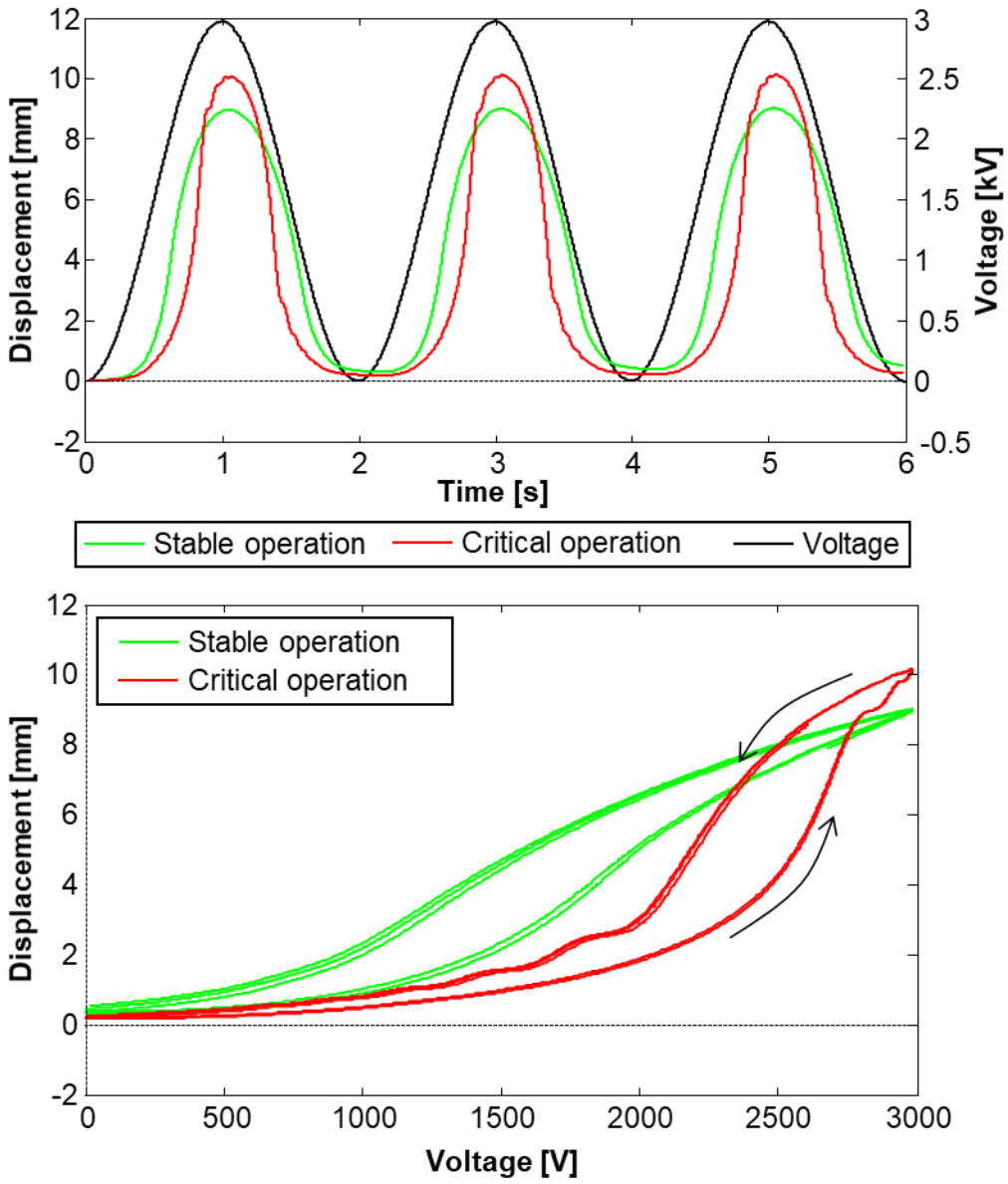

Figure 5.12: Top: Applied voltage (sinewave between 0 and 3 kV, 0.5 Hz) and the displacement response for a stable and critical stable (transition to unstable operation) system. Bottom: Hysteretic relation between displacement and applied voltage for the two systems.

5.3 Discussion of results

In this work, the performance of SIP-DEAs combined with different biasing mechanisms (LS and NBS) are compared. It is shown that a NBS, which has been mainly used in combination with COP-DEAs in previous works, provides an even larger increase in performance when combined with SIP-DEAs. A static actuation strain of 45% (equivalent to a stroke of 11.2 mm) is achieved. The corresponding force difference is of 0.38 N, and an

average elongation velocity of 0.29 m s^{-1} is measured. The force and stroke output of the NBS systems is more than nine times higher in comparison to the LS system. The force output is also higher than the blocking force of 0.15 N at maximum strain. An idealized biasing system, which is indicated by the yellow dashed line in Figure 5.13, would have resulted in even higher values, specifically 18.1 mm stroke (72% strain) and a force of 0.95 N. The idealized biasing is based on a conceptual NBS + LS combination, fulfilling the following criteria: longest straight line fitting in-between the two DEA curves, having one intersection with the 0 V and maximum one intersection with the 3000 V DEA curve. A hard stop prevents the DEA system from moving above the strain limit.

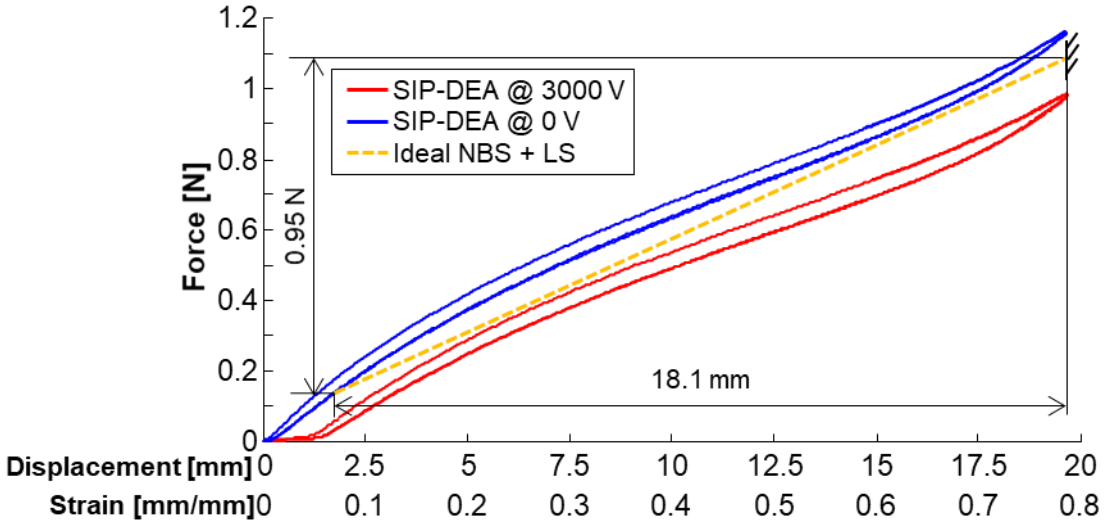

Figure 5.13: Force-displacement characteristic of the SIP-DEA and an idealized biasing mechanism.

Both the manufactured LS + NBS system and the idealized bias exhibit less actuation strain then the one reported by Plante [60] and Vogan [59] for in-plane DEAs. However, there is still room for improvement, for instance, reducing the applied voltage to allow higher strains and thus removing the hard stop. To maintain the force gap at a reduced voltage stacking of several DEAs might be necessary. Nevertheless, a simpler DEA design is demonstrated and the material used as dielectric is different among this work and the solutions in [59,60]. The silicone used in this work has a relative permittivity of 2.8, while the one of VHB used in [59,60] equals 4.7. This causes a higher Maxwell pressure (see equation (2.2)) and consequently higher actuation strain. However, silicone exhibits a much lower mechanical loss factor, which allows much faster actuation [25]. In comparison to

the results of diamond shape DEA based on VHB [131] the presented LS + NBS system with a silicone based DEA is approximately 60 times faster.

The presented work uses the well-known constrained steel crosses as a NBS. They exhibit a big disadvantage in terms of size, because they are orientated perpendicular to the SIP-DEA. Therefore, alternative ways to realize bi-stable biasing solutions have to be investigated. A possible solution could consist in using a pre-compressed beams like shown in [132]. A design study in Figure 5.14 shows this concept. The development of flat biasing solutions will allow the manufacturing of very flat DEA systems, which could fit much better the compactness requirements of several applications, such as valves. For commercialization, the reliability of the SIP-DEAs and the NBS needs to be investigated, too.

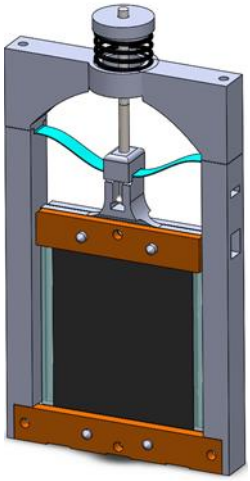

Figure 5.14: Design concept for a flat SIP-DEA system with a combination of a single beam NBS and LS for biasing.

Chapter 6 Conclusion and Outlook

The focus of this thesis is on the development of advanced high-performance DE membrane actuator systems. On the one hand, a concept was presented for the highest force output reported to date in out-of-plane membrane actuators, on the other hand, an innovative concept for biased in-plane actuators was developed that enables linear strokes of more than 50% of the actuator length. Both results are based on an approach, which combines mechanics of materials and advanced biasing concepts into a first systematic design methodology for the development of DE actuator systems.

Scaling laws, derived from a systematic study of COP-DEAs with different geometries, support the design process and additionally show the scalability as well as the design flexibility of DEAs. It is shown, for instance, that the force output of COP-DEAs linearly scales with the average electrode ring circumference, while the stroke linearly scales with the electrode ring width.

The potential of the design process is shown with the manufacturing of two demonstrators with record-high force output for two representative load cases. Silicone based membrane DEAs, which typically exhibit forces in the hundreds of millinewton-range, are intelligently combined with an appropriate biasing mechanism into a compact actuator system, which is able to lift 10 kg about 3.1 mm or to compress a spring (stiffness 30.7 N mm^{-1}) 2.8 mm resulting in a maximum force output of 87 N. A novel manufacturing process for stackable double-layer DEA modules with low-resistive electrical connections is developed within the design process in addition to an innovative high-force biasing concept for a compact overall design (86x86x25 mm^3).

Finally, a concept for fast high-stroke actuators is introduced. It is based on perfectly matching the DEA type to the biasing mechanism resulting in a silicone based SIP-DEA with a reversible stroke of 11.2 mm (equivalent to an actuation strain of 45%) and an average elongation speed of 0.29 m s^{-1}. Theoretically, strokes larger than 18 mm (72% strain) are possible by perfecting the practical construction.

Future work should improve the design of the SIP-DEA system in terms of compactness and applying the concepts of the high-force actuator similarly to SIP-DEAs to combine both, high stroke and force. For commercialization, the manufacturing process, in particular the stacking and electrical contacting process needs to be improved and automated. In addition, reliability studies are mandatory.

Dielectric elastomers are known as a promising technology to build small, lightweight, energy efficient, and smart systems, due to their ability of self-sensing. In this thesis, additional attributes of DEAs are investigated, proven or even added: Scalability, high force and high stroke output. This will enable the technology to compete with or even outperform existing technologies like solenoids or pneumatic cylinders in the future.

References

[1] Uchino, K., 1998, “Piezoelectric Ultrasonic Motors: Overview,” Smart Mater. Struct., **7**(3), pp. 273–285, doi: 10.1088/0964-1726/7/3/002.

[2] Fansler, T. D., Reuss, D. L., Sick, V., and Dahms, R. N., 2015, “Invited Review: Combustion Instability in Spray-Guided Stratified-Charge Engines: A Review,” Int. J. Engine Res., **16**(3), pp. 260–305, doi: 10.1177/1468087414565675.

[3] Actuator Solutions GmbH, “Smallest, Strongest, Simplest - The SMA Actuator” [Online]. Available: http://www.actuatorsolutions.de/products/. [Accessed: 28-Dec-2017].

[4] Carpi, F., De Rossi, D., Kornbluh, R. D., Pelrine, R. E., and Sommer-Larsen, P., 2008, *Dielectric Elastomers as Electromechanical Transducers: Fundamentals, Materials, Devices, Models and Applications of an Emerging Electroactive Polymer Technology*, Elsevier, doi: 10.1016/B978-0-08-047488-5.00033-2.

[5] Pelrine, R. E., Eckerle, J., and Chiba, S., 1992, “Review of Artificial Muscle Approaches,” *Proceedings of the 3rd International Symposium on Micro Machine and Human Science:*, Nagoya, Japan, pp. 1–19.

[6] Kornbluh, R. D., Pelrine, R. E., and Eckerle, J., 1995, “Elastomeric Dielectric Artificial Muscle Actuators for Small Robots,” *Proceedings of the 3rd IASTED International Conference on Robotics and Manufacturing*, Cancun, Mexico, pp. 1–6.

[7] Röntgen, W. C., 1880, “Ueber Die Durch Electricität Bewirkten Form- Und Volumenänderungen von Dielectrischen Körpern,” Ann. der Phys. und Chemie, **247**(13), pp. 771–786, doi: 10.1002/andp.18802471304.

[8] Pelrine, R. E., Kornbluh, R. D., and Joseph, J., 1998, “Electrostriction of Polymer Dielectrics with Compliant Electrodes as a Means of Actuation,” Sensors Actuators A Phys., **64**(1), pp. 77–85, doi: 10.1016/S0924-4247(97)01657-9.

[9] Kornbluh, R. D., Pelrine, R. E., and Pei, Q., 2000, “Dielectric Elastomer Produces a Strain of 380%,” *WorldWide ElectroActive Polymer Newsletter*, Y. Bar-Cohen, ed., 2:2, pp. 10–11.

[10] Pelrine, R. E., Sommer-Larsen, P., Kornbluh, R. D., Heydt, R., Kofod, G., Pei, Q., and Gravesen, P., 2001, "Applications of Dielectric Elastomer Actuators," *Proceedings of SPIE Smart Structures and Materials 2001: Electroactive Polymer Actuators and Devices*, Y. Bar-Cohen, ed., San Diego, p. 335, doi: 10.1117/12.432665.

[11] O'Halloran, A., O'Malley, F., and McHugh, P., 2008, "A Review on Dielectric Elastomer Actuators, Technology, Applications, and Challenges," J. Appl. Phys., **104**(7), p. 071101, doi: 10.1063/1.2981642.

[12] Fett, T., Müller, S., Munz, D., and Thun, G., 1998, "Nonsymmetry in the Deformation Behavior of PZT," J. Mater. Sci. Lett., **17**(4), pp. 261–265, doi: 10.1023/A:1006561001290.

[13] Bar-Cohen, Y., 2000, "Electroactive Polymers as Artificial Muscles: Capabilities, Potentials and Challenges," *Robotics 2000*, American Society of Civil Engineers, Reston, VA, pp. 188–196, doi: 10.1061/40476(299)24.

[14] Rizzello, G., Naso, D., York, A., and Seelecke, S., 2016, "Closed Loop Control of Dielectric Elastomer Actuators Based on Self-Sensing Displacement Feedback," Smart Mater. Struct., **25**(3), p. 035034, doi: 10.1088/0964-1726/25/3/035034.

[15] Hill, M., Rizzello, G., and Seelecke, S., 2017, "Development and Experimental Characterization of a Pneumatic Valve Actuated by a Dielectric Elastomer Membrane," Smart Mater. Struct., **26**(8), p. 085023, doi: 10.1088/1361-665X/aa746d.

[16] Giousouf, M., and Kovacs, G., 2013, "Dielectric Elastomer Actuators Used for Pneumatic Valve Technology," Smart Mater. Struct, **22**, pp. 104010–6, doi: 10.1088/0964-1726/22/10/104010.

[17] Carpi, F., Menon, C., and De Rossi, D., 2010, "Electroactive Elastomeric Actuator for All-Polymer Linear Peristaltic Pumps," IEEE/ASME Trans. Mechatronics, **15**, pp. 460–470, doi: 10.1109/TMECH.2009.2028884.

[18] Pelrine, R. E., Kornbluh, R. D., Heydt, R., and Heim, J. R., 2008, "Electroactive Polymer Devices for Moving Fluid."

[19] Shrestha, M., Asundi, A., and Lau, G., 2017, "Electrically Tunable Window Based on Microwrinkled ZnO/Ag Thin Film," *Proc. SPIE 10163, Electroactive Polymer Actuators and Devices (EAPAD)*, Y. Bar-Cohen, ed., p. 101631Y, doi: 10.1117/12.2259918.

[20] Kornbluh, R. D., Pelrine, R. E., Pei, Q., Heydt, R., Stanford, S., Oh, S., and Eckerle, J.,

2002, “Electroelastomers: Applications of Dielectric Elastomer Transducers for Actuation, Generation and Smart Structures,” *SPIE’s 9th Annual International Symposium on Smart Structures and Materials*, A.-M.R. McGowan, ed., International Society for Optics and Photonics, pp. 254–270, doi: 10.1117/12.475072.

[21] Choi, H. R., Lee, S. W., Jung, K. M., Koo, J. C., Lee, S. I., Choi, R. G., Jeon, J. W., and Nam, J. D., 2004, “Tactile Display as a Braille Display for the Visually Disabled,” *IEEE/RSJ International Conference on Intelligent Robots and Systems (IROS) (IEEE Cat. No.04CH37566)*, IEEE, pp. 1985–1990, doi: 10.1109/IROS.2004.1389689.

[22] Heydt, R., Kornbluh, R. D., Eckerle, J., and Pelrine, R. E., 2006, “Sound Radiation Properties of Dielectric Elastomer Electroactive Polymer Loudspeakers,” *Proc. SPIE Int. Soc. Opt. Eng.*, Y. Bar-Cohen, ed., p. 61681M, doi: 10.1117/12.659700.

[23] Huu Nguyen, C., Alici, G., and Mutlu, R., 2014, “A Compliant Translational Mechanism Based on Dielectric Elastomer Actuators,” J. Mech. Des., **136**(6), p. 061009, doi: 10.1115/1.4027167.

[24] Hau, S., Rizzello, G., Hodgins, M., York, A., and Seelecke, S., 2017, “Design and Control of a High-Speed Positioning System Based on Dielectric Elastomer Membrane Actuators,” IEEE/ASME Trans. Mechatronics, **22**(3), pp. 1259–1267, doi: 10.1109/TMECH.2017.2681839.

[25] Maffli, L., Rosset, S., Ghilardi, M., Carpi, F., and Shea, H. R., 2015, “Ultrafast All-Polymer Electrically Tunable Silicone Lenses,” Adv. Funct. Mater., **25**(11), pp. 1656–1665, doi: 10.1002/adfm.201403942.

[26] Shintake, J., Rosset, S., Schubert, B., Floreano, D., and Shea, H. R., 2016, “Versatile Soft Grippers with Intrinsic Electroadhesion Based on Multifunctional Polymer Actuators,” Adv. Mater., **28**(2), pp. 231–238, doi: 10.1002/adma.201504264.

[27] Araromi, O. A., Gavrilovich, I., Shintake, J., Rosset, S., Richard, M., Gass, V., and Shea, H. R., 2015, “Rollable Multisegment Dielectric Elastomer Minimum Energy Structures for a Deployable Microsatellite Gripper,” IEEE/ASME Trans. Mechatronics, **20**(1), pp. 438–446, doi: 10.1109/TMECH.2014.2329367.

[28] York, A., Dunn, J., and Seelecke, S., 2013, “Systematic Approach to Development of Pressure Sensors Using Dielectric Electro-Active Polymer Membranes,” Smart Mater. Struct., **22**, p. 094015, doi: 10.1088/0964-1726/22/9/094015.

[29] Pelrine, R. E., Kornbluh, R. D., Pei, Q., and Eckerle, J., 2004, “Electroactive Polymer

Sensors."

[30] Koh, S. J. A., Keplinger, C., Li, T., Bauer, S., and Suo, Z., 2011, "Dielectric Elastomer Generators: How Much Energy Can Be Converted?," IEEE/ASME Trans. Mechatronics, **16**(1), pp. 33–41, doi: 10.1109/TMECH.2010.2089635.

[31] Zanini, P., Rossiter, J., and Homer, M., 2017, "Self-Stabilizing Dielectric Elastomer Generators," Smart Mater. Struct., **26**(3), p. 035037, doi: 10.1088/1361-665X/aa59e6.

[32] McKay, T. G., Rosset, S., Anderson, I. A., and Shea, H., 2015, "Dielectric Elastomer Generators That Stack Up," Smart Mater. Struct., **24**(1), p. 015014, doi: 10.1088/0964-1726/24/1/015014.

[33] Anderson, I. A., Gisby, T. A., McKay, T. G., O'Brien, B., and Calius, E. P., 2012, "Multi-Functional Dielectric Elastomer Artificial Muscles for Soft and Smart Machines," J. Appl. Phys., **112**(4), p. 041101, doi: 10.1063/1.4740023.

[34] Wang, H., and Zhu, J., 2008, "Implementation and Simulation of a Cone Dielectric Elastomer Actuator," *Proc. SPIE 7266, Optomechatronic Technologies 2008*, Y. Otani, Y. Bellouard, J.T. Wen, D. Hodko, Y. Katagiri, S.K. Kassegne, J. Kofman, S. Kaneko, C.A. Perez, D. Coquin, O. Kaynak, Y. Cho, T. Fukuda, J. Yi, and F. Janabi-Sharifi, eds., p. 726607, doi: 10.1117/12.816412.

[35] Berselli, G., Vertechy, R., Vassura, G., and Parenti-Castelli, V., 2011, "Optimal Synthesis of Conically Shaped Dielectric Elastomer Linear Actuators: Design Methodology and Experimental Validation," IEEE/ASME Trans. Mechatronics, **16**(1), pp. 67–79, doi: 10.1109/TMECH.2010.2090664.

[36] Shahinpoor, M., Bar-Cohen, Y., Simpson, J. O., and Smith, J., 1998, "Ionic Polymer-Metal Composites (IPMCs) as Biomimetic Sensors, Actuators and Artificial Muscles - a Review," Smart Mater. Struct., **7**(6), pp. R15–R30, doi: 10.1088/0964-1726/7/6/001.

[37] Shankar, R., Ghosh, T. K., and Spontak, R. J., 2007, "Dielectric Elastomers as Next-Generation Polymeric Actuators," Soft Matter, **3**(9), p. 1116, doi: 10.1039/b705737g.

[38] O'Brien, B. M., Gisby, T. A., and Anderson, I. A., 2014, "Stretch Sensors for Human Body Motion," Y. Bar-Cohen, ed., International Society for Optics and Photonics, p. 905618, doi: 10.1117/12.2046143.

[39] Prahlad, H., Kornbluh, R. D., Pelrine, R. E., Stanford, S., Eckerle, J., and Oh, S., 2005,

"Polymer Power: Dielectric Elastomers and Their Applications in Distributed Actuation and Power Generation," *International Conference on Smart Materials Structures and Systems*, Bangalore, p. SA-100-SA-107.

[40] Kornbluh, R. D., Pelrine, R. E., Eckerle, J., and Joseph, J., 1998, "Electrostrictive Polymer Artificial Muscle Actuators," *Proceedings. 1998 IEEE International Conference on Robotics and Automation (Cat. No.98CH36146)*, IEEE, pp. 2147–2154, doi: 10.1109/ROBOT.1998.680638.

[41] York, A., Dunn, J., and Seelecke, S., 2010, "Experimental Characterization of the Hysteretic and Rate-Dependent Electromechanical Behavior of Dielectric Electro-Active Polymer Actuators," Smart Mater. Struct., **19**(9), p. 094014, doi: 10.1088/0964-1726/19/9/094014.

[42] Poulin, A., Rosset, S., and Shea, H. R., 2015, "Printing Low-Voltage Dielectric Elastomer Actuators," Appl. Phys. Lett., **107**(24), p. 244104, doi: 10.1063/1.4937735.

[43] Kofod, G., Sommer-Larsen, P., Kornbluh, R. D., and Pelrine, R. E., 2003, "Actuation Response of Polyacrylate Dielectric Elastomers," J. Intell. Mater. Syst. Struct., **14**(12), pp. 787–793, doi: 10.1177/104538903039260.

[44] Lotz, P., Matysek, M., and Schlaak, H. F., 2011, *Fabrication and Application of Miniaturized Dielectric Elastomer Stack Actuators*, doi: 10.1109/TMECH.2010.2090164.

[45] Maas, J., Tepel, D., and Hoffstadt, T., 2015, "Actuator Design and Automated Manufacturing Process for DEAP-Based Multilayer Stack-Actuators," Meccanica, **50**(11), pp. 2839–2854, doi: 10.1007/s11012-015-0273-2.

[46] Reitelshöfer, S., Göttler, M., Schmidt, P., Treffer, P., Landgraf, M., and Franke, J., 2016, "Aerosol-Jet-Printing Silicone Layers and Electrodes for Stacked Dielectric Elastomer Actuators in One Processing Device," *Proc. SPIE 9798, Electroactive Polymer Actuators and Devices (EAPAD) 2016*, Y. Bar-Cohen, and F. Vidal, eds., Las Vegas, doi: 10.1117/12.2219226.

[47] Kovacs, G., Düring, L., Michel, S., and Terrasi, G., 2009, "Stacked Dielectric Elastomer Actuator for Tensile Force Transmission," Sensors Actuators, A Phys., **155**(2), pp. 299–307, doi: 10.1016/j.sna.2009.08.027.

[48] Compliant Transducer Systems GmbH, "CT Systems/Product" [Online]. Available: http://www.ct-systems.ch/index.php/products. [Accessed: 29-Dec-2017].

[49] Lotz, P., 2009, “Dielektrische Elastomerstapelaktoren Für Ein Peristaltisches Fluidfördersystem,” Technische Universität Darmstadt.

[50] Bochmann, H., von Heckel, B., Hoffstadt, T., and Maas, J., 2016, “Interface Design for DE Based Stack-Actuators Considering Various Application Cases,” *Proc. SPIE 9798, Electroactive Polymer Actuators and Devices (EAPAD) 2016*, Y. Bar-Cohen, and F. Vidal, eds., p. 97982I, doi: 10.1117/12.2218012.

[51] Rosset, S., and Shea, H. R., 2016, “Small, Fast, and Tough: Shrinking down Integrated Elastomer Transducers,” Appl. Phys. Rev., **3**(3), doi: 10.1063/1.4963164.

[52] Jordi, C., Michel, S., Kovacs, G., and Ermanni, P., 2010, “Scaling of Planar Dielectric Elastomer Actuators in an Agonist-Antagonist Configuration,” Sensors Actuators A Phys., **161**(1–2), pp. 182–190, doi: 10.1016/j.sna.2010.05.015.

[53] Carpi, F., Anderson, I. A., Bauer, S., Frediani, G., Gallone, G., Gei, M., Graaf, C., Jean-Mistral, C., Kaal, W., Kofod, G., Kollosche, M., Kornbluh, R. D., Lassen, B., Matysek, M., Michel, S., Nowak, S., O’Brien, B., Pei, Q., Pelrine, R. E., Rechenbach, B., Rosset, S., and Shea, H. R., 2015, “Standards for Dielectric Elastomer Transducers,” Smart Mater. Struct., **24**(10), p. 105025, doi: 10.1088/0964-1726/24/10/105025.

[54] Rosset, S., de Saint-Aubin, C., Poulin, A., and Shea, H. R., 2017, “Assessing the Degradation of Compliant Electrodes for Soft Actuators,” Rev. Sci. Instrum., **88**(10), p. 105002, doi: 10.1063/1.4989464.

[55] Optotune, “Products” [Online]. Available: http://www.optotune.com/products. [Accessed: 06-Jan-2018].

[56] Kollosche, M., Zhu, J., Suo, Z., and Kofod, G., 2012, “Complex Interplay of Nonlinear Processes in Dielectric Elastomers,” Phys. Rev. E, **85**(5), p. 051801, doi: 10.1103/PhysRevE.85.051801.

[57] Hodgins, M., York, A., and Seelecke, S., 2017, “Systematic Experimental Characterization of Dielectric Elastomer Membranes Using a Custom-Built Tensile Test Rig,” J. Intell. Mater. Syst. Struct., **28**(15), pp. 2117–2128, doi: 10.1177/1045389X16685447.

[58] Fasolt, B., Hodgins, M., Rizzello, G., and Seelecke, S., 2017, “Effect of Screen Printing Parameters on Sensor and Actuator Performance of Dielectric Elastomer (DE) Membranes,” Sensors Actuators A Phys., **265**, pp. 10–19, doi: 10.1016/j.sna.2017.08.028.

[59] Vogan, J. D., 2004, "Development of Dielectric Elastomer Actuators for MRI Devices," Massachusetts Institute of Technology.

[60] Plante, J.-S., 2006, "Dielectric Elastomer Actuators for Binary Robotics and Mechatronics," Massachusetts Institute of Technology.

[61] Plante, J.-S., Devita, L. M., and Dubowsky, S., 2007, "A Road to Practical Dielectric Elastomer Actuators Based Robotics and Mechatronics: Discrete Actuation," Proc. SPIE 6524, Smart Struct. Mater. 2007 Electroact. Polym. Actuators Devices, **6524**, pp. 652406-652406–15, doi: 10.1117/12.715236.

[62] Berselli, G., Vassura, G., Parenti-Castelli, V., and Vertechy, R., 2010, "On Designing Compliant Actuators Based On Dielectric Elastomers for Robotic Applications," *Robot Manipulators New Achievements*, A. Lazinica, and H. Kawai, eds., InTech, Vukovar, Croatia, pp. 523–550, doi: 10.5772/9311.

[63] Conn, A. T., and Rossiter, J., 2012, "Towards Holonomic Electro-Elastomer Actuators with Six Degrees of Freedom," Smart Mater. Struct., **21**(3), p. 035012, doi: 10.1088/0964-1726/21/3/035012.

[64] Li, T., Keplinger, C., Baumgartner, R., Bauer, S., Yang, W., and Suo, Z., 2013, "Giant Voltage-Induced Deformation in Dielectric Elastomers near the Verge of Snap-through Instability," J. Mech. Phys. Solids, **61**(2), pp. 611–628, doi: 10.1016/j.jmps.2012.09.006.

[65] Rizzello, G., Naso, D., York, A., and Seelecke, S., 2015, "Modeling, Identification, and Control of a Dielectric Electro-Active Polymer Positioning System," IEEE Trans. Control Syst. Technol., **23**(2), pp. 632–643, doi: 10.1109/TCST.2014.2338356.

[66] Kesner, S. B., Plante, J.-S., Boston, P. J., Fabian, T., and Dubowsky, S., 2007, "Mobility and Power Feasibility of a Microbot Team System for Extraterrestrial Cave Exploration," *Proceedings 2007 IEEE International Conference on Robotics and Automation*, IEEE, pp. 4893–4898, doi: 10.1109/ROBOT.2007.364233.

[67] Kovacs, G., Lochmatter, P., and Wissler, M., 2007, "An Arm Wrestling Robot Driven by Dielectric Elastomer Actuators," Smart Mater. Struct., **16**(2), pp. S306–S317, doi: 10.1088/0964-1726/16/2/S16.

[68] Rajamani, A., Grissom, M. D., Rahn, C. D., and Zhang, Q., 2008, "Wound Roll Dielectric Elastomer Actuators: Fabrication, Analysis, and Experiments," IEEE/ASME Trans. Mechatronics, **13**(1), pp. 117–124, doi: 10.1109/TMECH.2008.915825.

[69] Szabo, J. P., 2005, “Fabrication of Polyurethane Dielectric Actuators,” Def. R&D Canada - Atl. Dartmouth.

[70] Pei, Q., Pelrine, R. E., Stanford, S., Kornbluh, R. D., and Rosenthal, M., 2003, “Electroelastomer Rolls and Their Application for Biomimetic Walking Robots,” Synth. Met., **135–136**, pp. 129–131, doi: 10.1016/S0379-6779(02)00535-0.

[71] Teh, Y. S., and Koh, S. J. A., 2016, “Giant Continuously-Tunable Actuation of a Dielectric Elastomer Ring Actuator,” Extrem. Mech. Lett., **9**, pp. 195–203, doi: 10.1016/j.eml.2016.07.002.

[72] Pei, Q., Rosenthal, M., Stanford, S., Prahlad, H., and Pelrine, R. E., 2004, “Multiple-Degrees-of-Freedom Electroelastomer Roll Actuators,” Smart Mater. Struct., **13**(5), pp. N86–N92, doi: 10.1088/0964-1726/13/5/N03.

[73] Köllnberger, A., 2017, “Silicone Elastomers for Dielectric EAP Applications,” *VDI Expertenforum 2017*, VDI, Karlsruhe, pp. 1–23.

[74] Kollosche, M., Stoyanov, H., Ragusch, H., Risse, S., Becker, A., and Kofod, G., 2010, “Electrical Breakdown in Soft Elastomers: Stiffness Dependence in Un-Pre-Stretched Elastomers,” *2010 10th IEEE International Conference on Solid Dielectrics*, IEEE, pp. 1–4, doi: 10.1109/ICSD.2010.5568259.

[75] Madsen, F. B., Daugaard, A. E., Hvilsted, S., and Skov, A. L., 2016, “The Current State of Silicone-Based Dielectric Elastomer Transducers,” Macromol. Rapid Commun., **37**(5), pp. 378–413, doi: 10.1002/marc.201500576.

[76] Michel, S., Zhang, X. Q., Wissler, M., Löwe, C., and Kovacs, G., 2010, “A Comparison between Silicone and Acrylic Elastomers as Dielectric Materials in Electroactive Polymer Actuators,” Polym. Int., **59**(3), pp. 391–399, doi: 10.1002/pi.2751.

[77] Rosset, S., O’Brien, B. M., Gisby, T., Xu, D., Shea, H. R., and Anderson, I. A., 2013, “Self-Sensing Dielectric Elastomer Actuators in Closed-Loop Operation,” Smart Mater. Struct., **22**(10), p. 104018, doi: 10.1088/0964-1726/22/10/104018.

[78] Pelrine, R. E., Kornbluh, R. D., Pei, Q., and Joseph, J., 2000, “High-Speed Electrically Actuated Elastomers with Strain Greater Than 100%,” Science (80-.)., **287**(5454), pp. 836–839, doi: 10.1126/science.287.5454.836.

[79] WackerChemieAG, “NEUE PERSPEKTIVEN UND INNOVATIVE ANWENDUNGEN MIT ELASTOSIL ® FILM HAUCHDÜNNE SILICONFOLIE,” Tech. Datasheet, pp. 1–4 [Online]. Available:

http://www.wacker.com/cms/media/publications/downloads/7091_DE.pdf. [Accessed: 02-Feb-2018].

[80] Matysek, M., Lotz, P., and Schlaak, H. F., 2011, "Lifetime Investigation of Dielectric Elastomer Stack Actuators," IEEE Trans. Dielectr. Electr. Insul., **18**(1), pp. 89–96, doi: 10.1109/TDEI.2011.5704497.

[81] Kornbluh, R., Wong-Foy, A., Pelrine, R., Prahlad, H., and McCoy, B., 2010, "Long-Lifetime All-Polymer Artificial Muscle Transducers," MRS Proc., **1271**, pp. 1271-JJ03-01, doi: 10.1557/PROC-1271-JJ03-01.

[82] Keplinger, C., Kaltenbrunner, M., Arnold, N., and Bauer, S., 2010, "Rontgen's Electrode-Free Elastomer Actuators without Electromechanical Pull-in Instability," Proc. Natl. Acad. Sci., **107**(10), pp. 4505–4510, doi: 10.1073/pnas.0913461107.

[83] Rosset, S., and Shea, H. R., 2013, "Flexible and Stretchable Electrodes for Dielectric Elastomer Actuators," Appl. Phys. A, **110**(2), pp. 281–307, doi: 10.1007/s00339-012-7402-8.

[84] Pimpin, A., Suzuki, Y., and Kasagi, N., 2007, "Microelectrostrictive Actuator With Large Out-of-Plane Deformation for Flow-Control Application," J. Microelectromechanical Syst., **16**(3), pp. 753–764, doi: 10.1109/JMEMS.2007.895222.

[85] Verplancke, R., Bossuyt, F., Cuypers, D., and Vanfleteren, J., 2012, "Thin-Film Stretchable Electronics Technology Based on Meandering Interconnections: Fabrication and Mechanical Performance," J. Micromechanics Microengineering, **22**(1), p. 015002, doi: 10.1088/0960-1317/22/1/015002.

[86] Benslimane, M. Y., Gravesen, P., and Sommer-Larsen, P., 2002, "Mechanical Properties of Dielectric Elastomer Actuators with Smart Metallic Compliant Electrodes," *Proc. SPIE 4695, Smart Structures and Materials 2002: Electroactive Polymer Actuators and Devices (EAPAD)*, Y. Bar-Cohen, ed., pp. 150–157, doi: 10.1117/12.475160.

[87] Poulin, A., Rosset, S., and Shea, H. R., 2016, "Fully Printed 3 Microns Thick Dielectric Elastomer Actuator," *Proc. SPIE 9798, Electroactive Polymer Actuators and Devices (EAPAD) 2016*, Y. Bar-Cohen, and F. Vidal, eds., doi: 10.1117/12.2218256.

[88] Schlatter, S., Rosset, S., and Shea, H. R., 2017, "Inkjet Printing of Carbon Black Electrodes for Dielectric Elastomer Actuators," *Electroactive Polymer Actuators and*

Devices (EAPAD) 2017, Y. Bar-Cohen, ed., Portland, p. 1016311, doi: 10.1117/12.2258615.

[89] Araromi, O. A., Rosset, S., and Shea, H. R., 2015, "High-Resolution, Large-Area Fabrication of Compliant Electrodes via Laser Ablation for Robust, Stretchable Dielectric Elastomer Actuators and Sensors," ACS Appl. Mater. Interfaces, **7**(32), pp. 18046–18053, doi: 10.1021/acsami.5b04975.

[90] Zakaria, S., Morshuis, P. H. F., Benslimane, M. Y., Yu, L., and Skov, A. L., 2015, "The Electrical Breakdown Strength of Pre-Stretched Elastomers, with and without Sample Volume Conservation," Smart Mater. Struct., **24**(5), p. 055009, doi: 10.1088/0964-1726/24/5/055009.

[91] Hodgins, M., York, A., and Seelecke, S., 2013, "Experimental Comparison of Bias Elements for Out-of-Plane DEAP Actuator System," Smart Mater. Struct., **22**, p. 094016, doi: 10.1088/0964-1726/22/9/094016.

[92] Hodgins, M., York, A., and Seelecke, S., 2011, "Modeling and Experimental Validation of a Bi-Stable out-of-Plane DEAP Actuator System," Smart Mater. Struct., **20**, p. 094012, doi: 10.1088/0964-1726/20/9/094012.

[93] Berselli, G., Vertechy, R., Vassura, G., and Parenti-Castelli, V., 2008, "A Compound-Structure Frame for Improving the Performance of a Dielectric Elastomer Actuator," *Advances in Robot Kinematics: Analysis and Design*, Springer Netherlands, Dordrecht, pp. 291–299, doi: 10.1007/978-1-4020-8600-7_31.

[94] Hodgins, M., and Seelecke, S., 2016, "Systematic Experimental Study of Pure Shear Type Dielectric Elastomer Membranes with Different Electrode and Film Thicknesses," Smart Mater. Struct., **25**(9), p. 095001, doi: 10.1088/0964-1726/25/9/095001.

[95] Hodgins, M., 2016, "Design of Diaphragm Dielectric Elastomer Actuators (DEAs) and Experimental Characterization Techniques," Saarland University.

[96] Loew, P., Rizzello, G., and Seelecke, S., 2017, "Permanent Magnets as Biasing Mechanism for Improving the Performance of Circular Dielectric Elastomer Out-of-Plane Actuators," *Proc. SPIE 10163, Electroactive Polymer Actuators and Devices (EAPAD)*, Y. Bar-Cohen, ed., Portland, p. 101630Y, doi: 10.1117/12.2258390.

[97] Bruch, D., 2017, "Designmethode Zur Auslegung Dielektrischer Elastomeraktoren Mit Nichtlinearen Balkenschnappfedern," Universität des Saarlandes.

[98] Bruch, D., Loew, P., Hau, S., Rizzello, G., and Seelecke, S., 2018, "Fast Model-Based Design of Large Stroke Dielectric Elastomer Membrane Actuators Biased with Pre-Stressed Buckled Beams," *Electroactive Polymer Actuators and Devices (EAPAD) XX*, Y. Bar-Cohen, ed., SPIE, p. 15, doi: 10.1117/12.2296558.

[99] Vangbo, M., and Bäcklund, Y., 1998, "A Lateral Symmetrically Bistable Buckled Beam," J. Micromechanics Microengineering, **8**(1), pp. 29–32, doi: 10.1088/0960-1317/8/1/005.

[100] Vangbo, M., 1998, "An Analytical Analysis of a Compressed Bistable Buckled Beam," Sensors Actuators A Phys., **69**(3), pp. 212–216, doi: 10.1016/S0924-4247(98)00097-1.

[101] Cazottes, P., Fernandes, A., Pouget, J., and Hafez, M., 2009, "Bistable Buckled Beam: Modeling of Actuating Force and Experimental Validations," J. Mech. Des., **131**(10), p. 101001, doi: 10.1115/1.3179003.

[102] Follador, M., Cianchetti, M., and Mazzolai, B., 2015, "Design of a Compact Bistable Mechanism Based on Dielectric Elastomer Actuators," Meccanica, **50**(11), pp. 2741–2749, doi: 10.1007/s11012-015-0212-2.

[103] Hau, S., York, A., and Seelecke, S., 2014, "Rapid Prototyping and Characterization of Circular Dielectric Electro-Active Polymers (DEAP) With Different Geometries," *ASME 2014 Conference on Smart Materials, Adaptive Structures and Intelligent Systems*, American Society of Mechanical Engineers, p. V002T02A004, doi: 10.1115/SMASIS2014-7477.

[104] Hau, S., York, A., and Seelecke, S., 2015, "Performance Prediction of Circular Dielectric Electro-Active Polymers Membrane Actuators with Various Geometries," *SPIE Smart Structures and Materials + Nondestructive Evaluation and Health Monitoring*, Y. Bar-Cohen, ed., International Society for Optics and Photonics, p. 94300C, doi: 10.1117/12.2082871.

[105] Hau, S., York, A., Rizzello, G., and Seelecke, S., 2018, "Performance Prediction and Scaling Laws of Circular Dielectric Elastomer Membrane Actuators," J. Mech. Des., (accepted manuscript), doi: 10.1115/1.4039104.

[106] Physik Instrumente (PI) GmbH, 2014, "PICMA ® Stack Multilayer- Piezoaktoren," Tech. Datasheet, pp. 1–5 [Online]. Available: http://www.piceramic.de/produkt-detailseite/p-882-p-888-100810.html. [Accessed: 05-Feb-2017].

[107] Dr. Fritz Faulhaber GmbH & CO. KG, 2016, “Antriebssysteme 2016,” Tech. Datasheet, p. 480 [Online]. Available: http://pdf.directindustry.de/pdf/faulhaber/antriebssysteme-2016/7023-637170.html. [Accessed: 26-Aug-2017].

[108] Tryson, M., Kiil, H.-E., and Benslimane, M. Y., 2009, “Powerful Tubular Core Free Dielectric Electro Activate Polymer (DEAP) Push Actuator,” *Proceedings of SPIE Smart Structures and Materials + Nondestructive Evaluation and Health Monitoring (EAPAD)*, Y. Bar-Cohen, and T. Wallmersperger, eds., p. 72871F, doi: 10.1117/12.815740.

[109] Gupta, U., Godaba, H., Zhao, Z., Chui, C. K., and Zhu, J., 2015, “Tunable Force/Displacement of a Vibration Shaker Driven by a Dielectric Elastomer Actuator,” Extrem. Mech. Lett., **2**(34), pp. 72–77, doi: 10.1016/j.eml.2015.02.004.

[110] Orita, A., and Cutkosky, M., 2016, “Scalable Electroactive Polymer for Variable Stiffness Suspensions,” IEEE/ASME Trans. Mechatronics, **21**(6), pp. 2836–2846, doi: 10.1109/TMECH.2016.2586484.

[111] Rizzello, G., Hodgins, M., Naso, D., York, A., and Seelecke, S., 2015, “Modeling of the Effects of the Electrical Dynamics on the Electromechanical Response of a DEAP Circular Actuator with a Mass–spring Load,” Smart Mater. Struct., **24**(9), p. 094003, doi: 10.1088/0964-1726/24/9/094003.

[112] He, T., Cui, L., Chen, C., and Suo, Z., 2010, “Nonlinear Deformation Analysis of a Dielectric Elastomer Membrane–spring System,” Smart Mater. Struct., **19**, p. 085017, doi: 10.1088/0964-1726/19/8/085017.

[113] Tezduyar, T. E., Wheeler, L. T., and Graux, L., 1987, “Finite Deformation of a Circular Elastic Membrane Containing a Concentric Rigid Inclusion,” Int. J. Non. Linear. Mech., **22**(1), pp. 61–72, doi: 10.1016/0020-7462(87)90049-7.

[114] Hodgins, M., Rizzello, G., Naso, D., York, A., and Seelecke, S., 2014, “An Electro-Mechanically Coupled Model for the Dynamic Behavior of a Dielectric Electro-Active Polymer Actuator,” Smart Mater. Struct., **23**(10), p. 104006, doi: 10.1088/0964-1726/23/10/104006.

[115] Wang, H., Zhu, J., and Ye, K., 2009, “Simulation, Experimental Evaluation and Performance Improvement of a Cone Dielectric Elastomer Actuator,” J. Zhejiang Univ. Sci. A, **10**(9), pp. 1296–1304, doi: 10.1631/jzus.A0820666.

[116] Mathew, A. T., and Koh, S. J. A., 2017, "Operational Limits of a Non-Homogeneous Dielectric Elastomer Transducer," Int. J. Smart Nano Mater., **00**(00), pp. 1–18, doi: 10.1080/19475411.2017.1421276.

[117] Dastoor, S., and Cutkosky, M., 2012, "Design of Dielectric Electroactive Polymers for a Compact and Scalable Variable Stiffness Device," *Proceedings - IEEE International Conference on Robotics and Automation*, pp. 3745–3750, doi: 10.1109/ICRA.2012.6224808.

[118] Hau, S., York, A., and Seelecke, S., 2016, "A Compact High-Force Dielectric Elastomer Membrane Actuator," *Actuator 2016, 15th International Conference on New Actuators & 9th International Exhibition on Smart Actuators and Drive Systems*, H. Borgmann, ed., MESSE BREMEN WFB Wirtschaftsförderung Bremen GmbH, Bremen, pp. 282–285.

[119] Hau, S., York, A., and Seelecke, S., 2016, "High-Force Dielectric Electroactive Polymer (DEAP) Membrane Actuator," *Proc. SPIE 9798, Electroactive Polymer Actuators and Devices (EAPAD) 2016*, Y. Bar-Cohen, and F. Vidal, eds., Las Vegas, doi: 10.1117/12.2220775.

[120] Hau, S., Rizzello, G., and Seelecke, S., 2018, "A Novel Dielectric Elastomer Membrane Actuator Concept for High-Force Applications," Extrem. Mech. Lett., **23**, pp. 24–28, doi: 10.1016/j.eml.2018.07.002.

[121] Otto Ganter GmbH & Co. KG, 2016, "Werkstoffeigenschaften von Nichtrostenden Edelstählen," pp. 1656–1658 [Online]. Available: https://www.ganter-griff.de/uploads/tx_rldownloadlist/edelstahl.pdf. [Accessed: 07-Apr-2018].

[122] H + S Präzisionsfolien, "H + S Präzisionsfolien - Technische Informationen" [Online]. Available: http://www.hs-folien.de/deutsch/tech-info.html. [Accessed: 03-Apr-2018].

[123] Patra, K., and Sahu, R. K., 2015, "A Visco-Hyperelastic Approach to Modelling Rate-Dependent Large Deformation of a Dielectric Acrylic Elastomer," Int. J. Mech. Mater. Des., **11**(1), pp. 79–90, doi: 10.1007/s10999-014-9270-1.

[124] Hau, S., Bruch, D., Rizzello, G., Motzki, P., and Seelecke, S., 2018, "Silicone Based Dielectric Elastomer Strip Actuators Coupled with Nonlinear Biasing Elements for Large Actuation Strains," Smart Mater. Struct., **27**(7), p. 074003, doi: 10.1088/1361-665X/aab7d8.

[125] Pelrine, R. E., Kornbluh, R. D., Joseph, J., Heydt, R., Pei, Q., and Chiba, S., 2000, “High-Field Deformation of Elastomeric Dielectrics for Actuators,” Mater. Sci. Eng. C, **11**(2), pp. 89–100, doi: 10.1016/S0928-4931(00)00128-4.

[126] Wingert, A., Lichter, M. D., and Dubowsky, S., 2006, “On the Design of Large Degree-of-Freedom Digital Mechatronic Devices Based on Bistable Dielectric Elastomer Actuators,” IEEE/ASME Trans. Mechatronics, **11**(4), pp. 448–456, doi: 10.1109/TMECH.2006.878542.

[127] Berselli, G., Vertechy, R., Vassura, G., and Parenti-Castelli, V., 2009, “Design of a Single-Acting Constant-Force Actuator Based on Dielectric Elastomers,” J. Mech. Robot., **1**(3), p. 031007, doi: 10.1115/1.3147182.

[128] Hodgins, M., Rizzello, G., York, A., and Seelecke, S., 2013, “High-Frequency Dynamic Model of a Pre-Loaded Circular Dielectric Electro-Active Polymer Actuator,” *ASME 2013 Conference on Smart Materials, Adaptive Structures and Intelligent Systems*, American Society of Mechanical Engineers, p. V002T02A020, doi: 10.1115/SMASIS2013-3259.

[129] Linnebach, P., Hau, S., Rizzello, G., Motzki, P., and Seelecke, S., 2018, “Stroke Magnification in Dielectric Elastomer Actuators with Dynamic Excitation,” *Actuator 2018, 16th International Conference on New Actuators & 9th International Exhibition on Smart Actuators and Drive Systems*, H. Borgmann, ed., MESSE BREMEN WFB Wirtschaftsförderung Bremen GmbH, Bremen, pp. 2–5.

[130] Rizzello, G., Naso, D., Turchiano, B., and Seelecke, S., 2016, “Robust Position Control of Dielectric Elastomer Actuators Based on LMI Optimization,” IEEE Trans. Control Syst. Technol., **24**(6), pp. 1909–1921, doi: 10.1109/TCST.2016.2519839.

[131] Plante, J.-S., and Dubowsky, S., 2007, “On the Properties of Dielectric Elastomer Actuators and Their Design Implications,” Smart Mater. Struct., **16**, pp. S227–S236, doi: 10.1088/0964-1726/16/2/S05.

[132] Gatti, D., Tropea, C., and Schlaak, H. F., 2014, “Dynamic Performance of Silicone Dielectric Elastomer Actuators with Bi-Stable Buckled Beams,” *SPIE Eapad 2014*, Y. Bar-Cohen, ed., p. 905638, doi: 10.1117/12.2045048.

List of figures

Figure 2.1: (a) Basic configuration of a DE in its initial and (b) in its charged state. 6

Figure 2.2: (a) Sketch of a stack actuator, (b) cross-section through the stack with electrical connections, and (c) cross-section through an activated stack. 9

Figure 2.3: Examples of stack actuators. (a) Stack actuator from University of Applied Sciences Ostwestfalen-Lippe, Germany, manufactured by folding and stacking [50]. (b) Commercial stack actuator made by CT-Systems, Switzerland [51] with process of Empa. (c) Stack actuator made by Empa, Switzerland, lifting a weight [47]. (d) Stack actuator for valve applications with sealing pad on top made by Empa, Switzerland [16]. 10

Figure 2.4: Minimum energy structure consisting of PET foil and a DE layer (a) at 0 V and (b) activated with 3.8 kV manufactured by École Polytechnique Fédérale de Lausanne [27]. 11

Figure 2.5: CIP-DEA biased by elastomer pre-stretch at (a) 0 V and (b) a high voltage applied. Strip in-plane (SIP) DEA biased by an external force at (c) 0 V and (d) a high voltage applied 12

Figure 2.6: Examples for in-plane actuators. (a) CIP-DEA for material evaluation developed by École polytechnique fédérale de Lausanne, Switzerland [54]. (b) Diamond-shaped linear actuator at its initial state and activated, manufactured by Massachusetts Institute of Technology, USA [61]. (c) CIP-DEA changing the light transmission developed by Nanyang Technological University, Singapore [19]. (d) Haptic feedback actuator and driving electronic designed for an iPod Touch by Artificial Muscle Inc., USA [51]. 13

Figure 2.7: Sketch and cross-section of a COP-DEA (a) at rest, (b) biased out-of-plane with an external force FB, and (c) biased out-of-plane with an external force FB and additionally $Vmax$ applied. 14

Figure 2.8: Examples for out-of-plane actuators. (a) COP-DEA for driving a valve manufactured by Saarland University, Germany [15]. (b) Multi DOF positioning system driven by two COP-DEAs (left: top view, right: side view) and manufactured by Bristol Robotics Laboratory, UK [63]. (c) COP-DEA driven jumping robot for extraterrestrial exploration manufactured by Massachusetts Institute of Technology, USA [61]. (d) Balloon-like DEA (left: at rest, right: activate) demonstrated by Zhejiang University, China [64]. 14

Figure 2.9: (a) Tube actuator in its initial state, (b) activated state, and (c) a cross-section of it. (d) Cross-section of a roll actuator. 16

Figure 2.10: Roll actuators with spring core in different sizes made by (a) Empa, Switzerland [67] and (b) Stanford Research Institute International, USA [20]. (c) Rolled actuator with passive core made by Defence R&D Canada–Atlantic [69]. (d) 2-DOF roll actuators with spring core used for a six-legged robot manufactured by Stanford Research Institute

International, USA [72]. (e) Ring actuator at 0 V (top) and 5.6 kV (bottom) exhibiting 142% actuation strain demonstrated by the National University of Singapore [71]..... 16

Figure 2.11: Radar chart demonstrating the equivalent importance of parameters of the elastomer for a successful actuator system design [cf. 70]. The parameters are grouped in market requirements (red) and material properties (blue), which overlap actuator performance (yellow). 17

Figure 2.12: Parameter space for an electrode ink used in a screen-printing process. 21

Figure 2.13: Schematic of the process flow for manufacturing a COP-DEA showing the progress after each manufacturing step. Initial sheet of silicone film (a), silicone film after pre-stretch (b), and screen-printing of electrode-rings (c) and frame material (d) on both side of the film. 22

Figure 2.14: Screens for printing the frame (a) and the electrode (b) of SIP-DEAs 23

Figure 2.15: Semi-automatic screen-printer ESC-AT 60P with a screen for COP-DEAs and completely printed COP-DEAs underneath. 24

Figure 2.16: Close-up photos of the low force setup shown in Figure 2.18. (a) Showing the laser sensor, the DEA mounting, and the motor. (b) Photo of the pushrod with a load cell attached before deflecting a COP-DEA. The HV amplifier is connected to the screws, which are screwed through the electrode for electrical connection. 25

Figure 2.17: Results of a CV measurement of a medium-sized D25 COP-DEA (see inset and Table 3-2). Light green area indicates the work area of this specific DEA. 26

Figure 2.18: Schematic sketch (a) and a photograph (b) of the low force test setup used for characterization. 27

Figure 2.19: (a) Photo of the high-force characterization setup measuring an actuator from Chapter 4 including load spring (Laser missing on photograph). (b) Schematic of the setup showing two operational modes: (1) Motor is moving to deflect a test specimen and (2) actuator is activated to measure generated force and stroke. 28

Figure 3.1: (a) Sketch of the DEA measurement with load cell (LC) and coordinate system and (b) qualitative results for a CV measurement and applied a low voltage (LV) and a high voltage (HV). 31

Figure 3.2: Sketch of the measurement setup (LC and biasing element) and the corresponding force-displacement characteristic of various biasing elements: (a) weight (mass), (b) linear spring with initial length $l0$, (c) buckling beam based negative-rate bias spring, and (d) magnet. 32

Figure 3.3: Schematic sketch of the system with global coordinate system x and individual coordinate systems of the elements, offsets O of the coordinate systems to each other, lengths S of the rigid spacers, and the initial spring length $l0$..... 33

Figure 3.4: FBD showing the individual forces acting onto the connecting rod. 34

Figure 3.5: (a) Material model of spring and NBS in the global coordinate system and (b) inverted forces as well as the sum of them. (c) Force equilibrium plot of the summed up biasing mechanism force and the DEA at different voltages. 35

Figure 3.6: Comparison of different biasing mechanisms acting against a COP-DEA. The kinematic equation just considers the direction reflected by the algebraic sign and offsets/ spacers are neglected. 36

Figure 3.7: (a) CAD model of a beam in a flat and a pre-compressed configuration showing the nomenclature. (b) Symmetrical bending mode at different deflections for a centrally loaded buckled beam in-between the two stable equilibria. (c) Schematic of force-displacement plot with critical forces and displacements marked with Fc and xc, respectively. 37

Figure 3.8: Comparison of the **exp**erimental (measured with low force setup described in section 2.5), **sim**ulated and **ana**lytically calculated (model of Vangbo [100]) force path of beam NBSs under different compression rates of 0.94, 0.96, and 0.98. 39

Figure 3.9: Parameter sweep for (a) beam length l, (b) compression rate c, (c) beam thickness t, and (d) beam width w. 40

Figure 3.10: Exemplary family of curves for the second Piola-Kirchhoff stress for each displacement step during the simulation. Due to the symmetric nature of the beam only one half of it ($l0/2 = 0.016\ m$) is considered. 41

Figure 3.11: Graphical illustration of a stepwise buckled beam geometry determination based on polynomial fits for the characteristic values extracted of the parameter study resulting in the values for a) beam length, b) and c) compression, d) and e) thickness, and f) width. 44

Figure 3.12: Comparison of simulated and targeted force-displacement characteristic. Crosses indicate targeted minimum and maximum force. 45

Figure 3.13: Six DEA geometries manufactured for testing and evaluation. Three D25 DEAs (upper row) and three D50 DEAs (lower row) with different IDs (small, medium large), respectively, are shown. The number after the 'D' indicates the overall dimensions, for instance D25 names a DEA with 25 mm edge length. 47

Figure 3.14: (a) Cross-section through the deflected DEAs shown in Figure 3.13. The sketch shows the truncated-cone approximation (straight lines) in comparison to an exaggerated actual membrane shape (dashed lines). (b) Sketch with nomenclature for calculations. 48

Figure 3.15: Transformation of the COP-DEA design (a) to an equivalent pure shear strip DEA design with a width equal to the average circumference $cave$ (c). (b) The intermediate step where the COP-DEA is just unwound into a strip DEA configuration. 50

Figure 3.16: (a) Averaged (number of test specimens per geometry n=6) force-displacement data for six different geometries at 0 V and 2500 V and (b) out of it calculated stress-strain plots. The dashed lines in (b) represent the results of the D50 DEA small, which deviates due to its high deviation from the truncated cone assumption. 51

Figure 3.17: (a) Training data set of a D25 DEA medium used to calculate (b) geometry independent material data using equation (3.9) and (3.15), as well as, (c) measured vs. predicted data (using material model) for 5 different DEA sizes. Photograph of DEAs are scaled down to half of their real size. 52

Figure 3.18: Results of blocking force measurements for a single DEA (D50 large size) at different strain levels for triangular input voltage. 54

Figure 3.19: Results of blocking force measurements for all DEAs of Table 3-2 at three different strain levels. Plotted quantities represent mean values (n=8) with error bars and linear regression line. The three data points for each data set represent the different inner disc diameters: small, medium large (left to right)..... 55

Figure 3.20: Boxplot showing the blocking force normalized on the average circumference $cave$ grouped by the two different DEA sizes at three different strain levels. Sample size for each box n=18. 56

Figure 3.21: Estimated stroke at two different strain levels for all six different DEAs over electrode-ring width $l0$. Marker indicate mean values (n=6). Error bars are neglected because they are smaller than the marker. 56

Figure 3.22: Scaling laws for stroke and force output of COP-DEAs: (a) for constant outer diameter, (b) constant inner diameter and (c) constant electrode-ring width. 57

Figure 3.23: (a) Scaling of the force difference by choosing materials with different Young's moduli and adapting the NBS. Material 2 is chosen to be stiffer than Material 1 and the Maxwell pressure is assumed constant. (b) Increasing the work area as well as the force difference by stacking multiple DEAs. The blocking force ΔF is measured at 5 mm displacement. 58

Figure 3.24: Design process of a DEA system to match a specific load. 59

Figure 3.25: (a) Sketch of the DEA system and a load. The sketch also contains the FBD and the global coordinate system. (b) Sketch of the measurement setup for characterizing the load and (c) the corresponding force-displacement characteristic with the desired stroke Δs. 60

Figure 3.26: (a) Individual forces of the load, a single DEA at HV and LV and a stack of four DEAs. (b) Graphical solution for equation (3.17) of the actuator system shown in Figure 3.25, which is useful for designers of actuator systems. 61

Figure 3.27: (a) Arbitrary biasing force and (b) the graphical solution for equation (3.20) of the actuator system shown in Figure 3.25, which is interesting for the customer of actuator systems. 62

Figure 4.1: Comparison of predicted and measured force-displacement characteristic of a DEA with ID=50 mm and OD=65 mm. The prediction is based on the training data set of a nine times smaller DEA shown in Figure 3.17 (a). 68

Figure 4.2: (a) CAD picture of the outside with the low voltage electrode (blue, which is partly covered by the frame (brown) and (b) corresponding photograph. (c) CAD picture of the inside with the high voltage electrode (red) and (d) corresponding photograph. (e) Fully printed DEA before folding with blocked out center disc. (f) Folded double-layer COP-DEA module with coper terminations for a low-resistive electrical interconnection. 69

Figure 4.3: Electrical connection of DEA modules within stack via applied copper tape. Stack is already mounted into the casing shown in Figure 4.9. 70

Figure 4.4: (a) Laser cut spring steel cross, which is used as a NBS when constrained in a (b) compression-frame (prototype made of Delrin®) with smaller outer dimensions. The frame can house a stack of metal crosses. 71

Figure 4.5: (a) Cross-section of a bended beam with resulting tension (red) and compression (blue) stress. (b) Comparison of a NBS made of stainless steel (1.4310 (X10CrNi18-8), yield strength 195 MPa, Young's modulus 200 GPa [121]) and one made with hardened spring steel (1.1274 (C100S), yield strength 2 to 2200 MPa, Young's modulus 210 GPa [122]). Both are geometrically identical (geometry shown in Figure 4.4, thickness 100 µm) and are mounted into a 96% compression-frame. 71

Figure 4.6: Top: Force-displacement characteristic metal cross stacks with different numbers of metal-crosses stacked (geometry shown in Figure 4.4, thickness 100 µm, and compression-frame 97%). Bottom: Normalized (divided by the number of stacked NBS) force data of top showing an increase of hysteresis as well as a decrease of the force difference, when metal crosses are stacked. 72

Figure 4.7: (a) Cross-section of two stacked beams. The two beams are intended to have the exact same curvature (R1=R2) to create the intended force. However, they block each other when bending (hatched area), which is resulting in the different curvatures (R1<R3). (b) Comparison of three NBSs made of 12 stacked metal crosses (geometry shown in Figure 4.4, thickness 100 µm, compression-frame 97%) with 50 and 100 µm thick spacers as well as without spacers. (c) Inset (1) shows that the hysteresis close to the origin is slightly smaller with spacers. (d) Inset (2) also indicates a slightly reduced hysteresis, while there is no trend for the minimum achieved force. 73

Figure 4.8: Photograph and CAD model cross-section of an assembled biasing mechanism with two compressed LSs. 74

Figure 4.9: (a) CAD drawing and (b) photograph of the assembled actuator system with an overall size of 86x86x25 mm³. 75

Figure 4.10: (a) CAD model cross-section of the actuator system showing the integration of the biasing mechanism into the blocked out center of the DEA module stack. (b) Sketch showing the mechanical interaction of the DEA stack, NBS, and LS. The yellow arrow in (a) and (b) indicates the possible offset adjustment of the biasing mechanism relative to the DEA stack, while the green arrow shows the possibility to adjust the LS pre-compression. 76

Figure 4.11: (a) Designer diagram showing the equilibria for $FL + FD = FS + FN$ and (b) customer diagram showing the equilibrium $FL = FD + FS + FN$. Red and blue curve are calculated with the data plotted of (a) and the green ones are the corresponding actuator forces measured at the assembled actuator. The individual forces of the two diagrams are measured with the high-force setup. (c) Inset 1 showing the intersection of the low voltage curve and the biasing the designer diagram and (d) inset 2 showing the intersection with the high voltage curve. 78

Figure 4.12: Photograph of the actuator system with the 10 kg load on top. The load is guided with a linear bearing (top center of photograph) to prevent it from tilting. 79

Figure 4.13: Displacement response of the high-force actuator working against a dead load of 10 kg for a square voltage input signal. 79

Figure 4.14: Force displacement characteristic of the DEA and the load. 80

Figure 4.15: (a) Designer diagram showing the equilibriums for $FL + FD = FS + FN$ with the intended load (stiffness 38.4 N mm^{-1}) and (b) customer diagram showing the equilibrium $FL = FD + FS + FN$ for both, intended and actual load. The individual forces of the two diagrams are measured with the high-force setup. (c) Inset 1 showing the intersection of the low voltage curve and the biasing in the designer diagram and (d) inset 2 showing the intersection with the high voltage curve. 81

Figure 4.16: Actuator and load spring mounted into the high-force setup for characterization purpose..... 82

Figure 4.17: Force and displacement response of the high-force actuator working against a LS load for a sinusoidal voltage input signal..... 83

Figure 5.1: NBS (green dashed line) acting against (a) a COP-DEA and (b) a SIP-DEA. The blue curves indicates the LV and the red curves the high voltage HV force-displacement characteristic of the DEA, respectively. Due to the force equilibria between NBS and DEAs, the NBS spring rate switches sign and appears to be positive. 86

Figure 5.2: Concept sketch of a SIP-DEA coupled with a biasing element (tension spring). An electrical stimulation causes the SIP-DEA to expand about Δs. 87

Figure 5.3: (a) Top view sketch of the batch processed SIP-DEAs. (b) Cross-section sketch to illustrate the layer composition. 88

Figure 5.4: Picture including final dimensions (DEA is relaxed, no pre-stretch) of the SIP-DEA manufactured. The uncoated silicone film is highlighted in light blue for a better visibility. 89

Figure 5.5: Picture of laser-cut stainless steel cross (a) and buckled up steel cross within a compression-frame (b) (scale 1:2)..... 90

Figure 5.6: Results of the CV test of the DEA at zero and 3000 V and of the NBS-LS-combination..... 90

Figure 5.7: Blocking force results of CP test at 80% strain for a triangular input voltage at different frequencies. 91

Figure 5.8: Picture of the actuator system consisting of a DEA biased with a tension spring. 93

Figure 5.9: Sketch (a) and picture (b) of the actuator system consisting of a DEA and the combinations of NBS and compression LS. The actuator system is mounted into the characterization setup with a laser sensor and a load cell for stroke and force measurements, which is described in Section 2.5. 93

Figure 5.10: Comparison of the performance for both actuator systems build. (a) Actuator stroke response on a voltage step and (b) inset (1) settling of the actuator stroke after activation. In (c) and (d), the same plots are shown for the force response. The force plotted is not the absolute value; it is zeroed at the zero volt equilibrium..... 94

Figure 5.11: (a) Current and voltage vs. time and (b) force and displacement vs. time for the LS + NBS system, respectively. 95

Figure 5.12: Applied voltage (sinewave between 0 and 3 kV, 0.5 Hz) and the displacement response for a stable and critical stable (transition to unstable operation) system (top.

Hysteretic relation between displacement and applied voltage for the two systems (bottom). 97

Figure 5.13: Force-displacement characteristic of the SIP-DEA and an idealized biasing mechanism. 98

Figure 5.14: Design concept for a flat SIP-DEA system with a combination of a single beam NBS and LS for biasing. 99

List of tables

Table 1.1: Comparison of smart materials properties and conventional EM actuators (voice coil). Data refers to [10] unless otherwise stated. 2

Table 2.1: Comparison of different elastomer materials. Values reported may depend on test conditions such as the strong relation between breakdown field and applied strain or Young's modulus, respectively. 19

Table 3.1: Flowchart showing the four calculation steps for all buckled beam NBS different NBS parameters used for the parameter study. 42

Table 3.2: Overview of the geometries of the different test specimens. Six different geometries are tested. 47

Table 3.3: Comparison of measured and predicted blocking force at a strain of 0.25. 53

Table 3.4: Comparison of measured and predicted stroke for a hanging mass of 40 g. 53

List of abbreviations

CIP	Circular-in-plane
COP	Circular out-of-plane
CP	Constant position
CV	Constant voltage
DAQ	Data acquisition board
DE	Dielectric elastomer
DEA	Dielectric elastomer actuator
DET	Dielectric elastomer transducer
DOF	Degree of freedom
EAC	Electroactive ceramic
EAP	Electroactive polymer
EM	Electromagnetic
FBD	Free body diagram
FE	Finite element
HV	High voltage
ID	Inner diameter
IPMC	Ionic polymer-metal composites
LC	Load cell
LS	Linear spring
LV	Low voltage
NBS	Negative-rate bias spring
NI	National Instruments
NiTi	Nickel titanium alloy
OD	Outer diameter
PDMS	Polydimethylsiloxane

PET	Polyethylenterephthalat
PZT	Lead zirconate titanate
SIP	Strip-in-plane
SMA	Shape memory alloy
VHB	Very high bond (trade mark of 3M for acrylic tape)

Nomenclature

A	Electrode Area
$A_{el,0}$	Area of electrode-ring
$A_{el,d}$	Area of cone shell
C	Capacitance of the DE or constant
E	Electric field
F	Force, indices link the force to certain mechanical elements (S: Spring, N: NBS, L: Load, D: DEA)
F_m	Measured force
$O_{P,Q}$	Offset between the mechanical elements P and Q
P	Maxwell pressure
$S_{P,Q}$	Length of a spacer between the mechanical elements P and Q
V	Voltage
V_{max}	Maximum actuation voltage
Vol	Volume of elastomer membrane
c_{ave}	Average electrode-ring circumference
c_{in}	Circumference of the inner disc
c_{out}	Circumference of the outer frame
d	Inner disc displacement
l_0	Electrode-ring width or initial spring length
l_d	Electrode-ring width during displacement
n	Number of test specimens
r	Radius of the inner disc
r_a	Radius where stress is calculated
t	Thickness of elastomer
t_0	Initial elastomer membrane thickness after pre-stretch

t_d	Elastomer membrane thickness after pre-stretch and deflection of COP-DEA
x	Displacement or coordinate
ΔF	Resulting force difference
Δs	Stroke of actuators
α	Angle between direction of displacement and stretched elastomer membrane
ε	Mechanical strain
ε_0	Void permittivity
ε_r	Relative dielectric constant
λ	Stretch
σ	Mechanical stress

Curriculum Vitae

Steffen Hau

Am Geißenrech 67
66424 Homburg

Germany
E-Mail: steffen.hau@gmx.de

PERSÖNLICHE DATEN

Familienstand:	verheiratet
Staatsangehörigkeit:	deutsch
Geburtsdatum:	24.07.1984
Geburtsort:	Zweibrücken

BERUFSERFAHRUNG

seit 01.04.2013 **Promotion an der Universität des Saarlandes**
Lehrstuhl für intelligente Material Systeme (iMSL)
„High-performance dielectric elastomer actuator“

von 01.07.2012 bis 29.03.2013 **Masterarbeit an der Universität des Saarlandes**
Lehrstuhl für Mikromechanik, Mikrofluidik/Mikroaktorik
„Design, Herstellung und Charakterisierung eines piezoelektrischen Dehnungssensors auf flexiblem Substrat“
Bewertung: Sehr gut (1,3)

von 01.01.2012 bis 31.06.2012 **Masterseminar an der Universität des Saarlandes**
Lehrstuhl für Mikromechanik, Mikrofluidik/Mikroaktorik
“Betrachtungen zur Zuverlässigkeit von Titan-Dünnschichtleiterbahnen auf verschiedenen Substratmaterialien“

von 08.10.2007 bis 31.10.2010 **R&D Engineer bei Infineon Technologies in Regensburg**
Backend Development: Discrete and Sensor Packages
Davon 3 Monate bei Infineon Technologies in Malacca/Malaysia
Package- und Prozessentwicklung für Die Bonding und SMD Bestückung

von 01.03.2007 bis 31.08.2007 **Diplomarbeit bei XAAR Jet AB in Järfälla/Schweden**
Advanced Manufacturing Technology (AMT) Department
„Fundamental investigations of the performance of a new type of inkjet system for printing of functional fluids”
Bewertung: Sehr gut (1,0)

von 19.09.2005 bis 31.01.2006	**Praxissemester am Institut für Mikro- und Informationstechnik (HSG-IMIT) in Villingen-Schwenningen** *Mikrofluidik Gruppe* „Aufbau und Test einer fluidischen Plattform für ein miniaturisiertes Medikamentendosiersystem“

BILDUNGSWEG

2010 - 2013	**Universität des Saarlandes** *Fachrichtung: Mechatronik mit Vertiefung Mikrosystemtechnik* Prüfung Master of Science (M.Sc.) mit dem Gesamtergebnis: Sehr gut (1,5)
2003 - 2007	**Fachhochschule Kaiserslautern Standort Zweibrücken** *Fachrichtung: Mikrosystemtechnik mit Schwerpunkt Fertigung* Diplomprüfung zum Dipl.-Ing (FH) mit dem Gesamtergebnis: Gut (1,8) Diplomvorprüfung mit dem Gesamtergebnis: Gut (2,2)
2000 - 2002	**Fachoberschule am Berufsbildungszentrum in Homburg** *Fachrichtung: Elektrotechnik* Fachhochschulreife mit der Durchschnittsnote: Gut (2,0)
1994 - 2000	**Realschule des Saarpfalz-Kreises in Homburg** *Mittlere Reife*

WEHRDIENST

von 01.10.2002 bis 30.06.2003	**Grundwehrdienst im 2./Raketenartillerielehrbataillon 52 in Hermeskeil** *Ausbildung zum Raketenkanonier*

KENNTNISSE

Englisch sehr gut in Wort und Schrift

Sehr gute Kenntnisse in SolidWorks, MATLAB und MS-Office

Gute Kenntnisse in LabVIEW und Visual Basic

Zertifikat zum Laserschutzbeauftragten

AUSZEICHNUNGEN

2017	1. Platz EuroEAP Konferenz „Society Challenge“ in Cartagena/ Spanien
2017	2. Platz SPIE Konferenz „Hardware Challenge“ in Portland/ USA
2013	Studienpreis der Küborth-Stiftung: schnelles Studium mit sehr gutem Abschluss
2012	2. Platz beim internationalen Studentenwettbewerb "iCan" in Peking
2011-2013	Deutschland Stipendium der Robert Bosch GmbH

EHRENAMTLICHE TÄTIGKEITEN

Seit 2002	Gruppenleiter bei der Deutsche Pfadfinderschaft St. Georg (DPSG)
2011 - 2013	Platzwart des Jugendzeltplatz „Herrgottshübel“ in Homburg-Jägersburg
2004 - 2007	Mitglied des Ortsrates Jägersburg
2004 - 2007	Mitglied des Kreisjugendhilfeausschusses des Saarpfalz-Kreis

HOBBYS

Pfadfinder, Tanzen, Squash

Publications

Peer-reviewed journal publications:

Motzki, P., **Hau, S.,** Schmidt, M., and Seelecke, S., 2018, "Künstliche Muskeln Und Nerven in Industrie 4.0 Konzepten," Ind. 4.0 Manag., 2018(4), pp. 38–41, doi: 10.30844/I40M18-4_38-41.

Hau, S., Motzki, P., and Seelecke, S., 2018, "Aktor-Sensor-Systeme," GIT Labor-Fachzeitschrift, 7, pp. 2–4.

Hau, S., Rizzello, G., and Seelecke, S., 2018, "A Novel Dielectric Elastomer Membrane Actuator Concept for High-Force Applications," Extrem. Mech. Lett., (accepted manuscript) doi: 10.1016/j.eml.2018.07.002.

Hau, S., Bruch, D., Rizzello, G., Motzki, P., and Seelecke, S., 2018, "Silicone Based Dielectric Elastomer Strip Actuators Coupled with Non-Linear Biasing Elements for Large Actuation Strains," Smart Mater. Struct., doi: 10.1088/1361-665X/aab7d8.

Hau, S., York, A., Rizzello, G., and Seelecke, S., 2018, "Performance Prediction and Scaling Laws of Circular Dielectric Elastomer Membrane Actuators," J. Mech. Des., (accepted manuscript), doi: 10.1115/1.4039104.

Hau, S., Rizzello, G., Hodgins, M., York, A., and Seelecke, S., 2017, "Design and Control of a High-Speed Positioning System Based on Dielectric Elastomer Membrane Actuators," IEEE/ASME Trans. Mechatronics, 22(3), pp. 1259–1267, doi: 10.1109/TMECH.2017.2681839.

International conference proceedings:

Lenz, S., Holz, B., **Hau, S.,** Motzki, P., and Seelecke, S., 2018, "Development of a High Voltage Source for Dielectric Elastomer Actuators (DEA)," Actuator 2018, 16th International Conference on New Actuators & 9th International Exhibition on Smart Actuators and Drive Systems, H. Borgmann, ed., MESSE BREMEN WFB Wirtschaftsförderung Bremen GmbH, Bremen.

Linnebach, P., **Hau, S.,** Rizzello, G., Motzki, P., and Seelecke, S., 2018, “Stroke Magnification in Dielectric Elastomer Actuators with Dynamic Excitation,” Actuator 2018, 16th International Conference on New Actuators & 9th International Exhibition on Smart Actuators and Drive Systems, H. Borgmann, ed., MESSE BREMEN WFB Wirtschaftsförderung Bremen GmbH, Bremen, pp. 2–5.

Bruch, D., Loew, P., **Hau, S.,** Rizzello, G., and Seelecke, S., 2018, “Fast Model-Based Design of Large Stroke Dielectric Elastomer Membrane Actuators Biased with Pre-Stressed Buckled Beams,” Electroactive Polymer Actuators and Devices (EAPAD) XX, Y. Bar-Cohen, ed., SPIE, p. 15, doi: 10.1117/12.2296558.

Hau, S., York, A., and Seelecke, S., 2016, “A Compact High-Force Dielectric Elastomer Membrane Actuator,” Actuator 2016, 15th International Conference on New Actuators & 9th International Exhibition on Smart Actuators and Drive Systems, H. Borgmann, ed., MESSE BREMEN WFB Wirtschaftsförderung Bremen GmbH, Bremen, pp. 282–285.

Hau, S., York, A., and Seelecke, S., 2016, “High-Force Dielectric Electroactive Polymer (DEAP) Membrane Actuator,” Proc. SPIE 9798, Electroactive Polymer Actuators and Devices (EAPAD) 2016, Y. Bar-Cohen, and F. Vidal, eds., Las Vegas, doi: 10.1117/12.2220775.

Hau, S., York, A., and Seelecke, S., 2015, “Performance Prediction of Circular Dielectric Electro-Active Polymers Membrane Actuators with Various Geometries,” SPIE Smart Structures and Materials + Nondestructive Evaluation and Health Monitoring, Y. Bar-Cohen, ed., International Society for Optics and Photonics, p. 94300C, doi: 10.1117/12.2082871.

Hau, S., Hodgins, M., Rizzello, G., York, A., and Seelecke, S., 2015, “Entwicklung Einer Durch Dielektrische Elektroaktive Polymeraktoren (DEAP) Angetriebenen Hochgeschwindigkeitsmikropositionierbühne,” Mechatronik 2015, Dortmund, pp. 73–78, doi: 10.13140/RG.2.1.3180.3363.

Hau, S., York, A., and Seelecke, S., 2014, “Rapid Prototyping and Characterization of Circular Dielectric Electro-Active Polymers (DEAP) With Different Geometries,” ASME 2014 Conference on Smart Materials, Adaptive Structures and Intelligent Systems, American Society of Mechanical Engineers, p. V002T02A004, doi: 10.1115/SMASIS2014-7477.

Hau, S., Marschibois, M., Seidel, H., and Feili, D., 2013, “AlN Auf Flexiblem Substrat Für Langzeitstabile, Energieautonome Sensorsysteme,” Mikrosystemtechnik 2013 - Von Bauelementen Zu Systemen, Aachen.

Poster presentations:

Hau, S., and Seelecke, S., 2017, "Silicone Based Dielectric Elastomer Strip Actuators Coupled with Non-Linear Biasing Elements for Large Actuation Strains," EuroEAP 2017 - International Conference on Electromechanically Active Polymer (EAP) Transducers & Artificial Muscle, Cartagena.

Zhang, X., Verhagen, A., Zhu, Q., **Hau, S.,** and Seelecke, S., 2016, "Design and Control Strategies for a Novel Actuator System with Dielectric Electroactive Polymer and Spring," Actuator 2016, 15th International Conference on New Actuators & 9th International Exhibition on Smart Actuators and Drive Systems, H. Borgmann, ed., MESSE BREMEN WFB Wirtschaftsförderung Bremen GmbH, Bremen, pp. 514–517.

Hau, S., York, A., and Seelecke, S., 2015, "Design and Manufacturing of a Compact High-Performance Stacked Membrane DEAP Actuator," EuroEAP 2015 - International Conference on Electromechanically Active Polymer (EAP) Transducers & Artificial Muscles, Tallinn.

Hodgins, M., **Hau, S.,** Rizzello, G., York, A., and Seelecke, S., 2014, "Design, Fabrication, Testing and Control of a High Speed Micro-Positioning Stage Driven by Dielectric Electro-Active Polymer (DEAP) Actuators," EuroEAP 2014 - International Conference on Electromechanically Active Polymer (EAP) Transducers & Artificial Muscles, Linköping.

Hau, S., York, A., and Seelecke, S., 2014, "Circular Dielectric Electro-Active Polymers (DEAP) with Adapted Geometries to Specific Applications," EuroEAP 2014 - International Conference on Electromechanically Active Polymer (EAP) Transducers & Artificial Muscles, Linköping.

Hodgins, M., **Hau, S.,** York, A., and Seelecke, S., 2013, "Improving the Stroke of Dielectric Electro-Active Polymer Actuators Using a Non-Linear Spring," EuroEAP 2013 - International Conference on Electromechanically Active Polymer (EAP) Transducers & Artificial Muscles, Zürich.

Eidesstattliche Versicherung

Hiermit versichere ich an Eides statt, dass ich die vorliegende Arbeit selbständig und ohne Benutzung anderer als der angegebenen Hilfsmittel angefertigt habe. Die aus anderen Quellen oder indirekt übernommenen Daten und Konzepte sind unter Angabe der Quelle gekennzeichnet.

Die Arbeit wurde bisher weder im In- noch im Ausland in gleicher oder ähnlicher Form in einem Verfahren zur Erlangung eines akademischen Grades vorgelegt.

Ich erkläre hiermit an Eides statt, dass die vorliegende Arbeit mit der elektronischen Version übereinstimmt.

Ich erkläre darüber hinaus mit meiner Unterschrift, dass ich

- keine im Merkblatt "Hinweise zur Vermeidung von Plagiaten" der Naturwissenschaftlich-Technischen Fakultät beschriebene Form des Plagiats begangen habe,
- alle Methoden, Daten und Arbeitsabläufe wahrheitsgetreu dokumentiert habe und
- keine Daten manipuliert habe.

Saarbrücken, 11.05.2018

_____

Steffen Hau